

Fakultät für Physik der Technischen Universität München
Physik-Department E12

Coulomb Excitation of Proton Rich Nuclei ^{32}Ar and ^{34}Ar

Olga Lepyoshkina

Vollständiger Abdruck der von der Fakultät für Physik der Technischen Universität
München zur Erlangung des akademischen Grades eines

Doktors der Naturwissenschaften (Dr. rer. nat.)

genehmigten Dissertation.

Vorsitzende:

Univ.-Prof. Dr. N. Brambilla

Prüfer der Dissertation:

1. Univ.-Prof. Dr. R. Krücken
2. Univ.-Prof. Dr. L. Oberauer (schriftliche Beurteilung)
- Univ.-Prof. Dr. F. von Feilitzsch (mündliche Prüfung)

Die Dissertation wurde am 22.02.2013 bei der Technischen Universität München ein-
gereicht und durch die Fakultät für Physik am 16.04.2013 angenommen.

Abstract

In the present thesis an investigation of the low-lying strength in the proton-rich nuclei ^{32}Ar and ^{34}Ar is reported. The earlier observation of low-lying dipole strength in neutron-rich nuclei and its interpretation with respect to basic nuclear properties (symmetry energy, skin thickness) initiated the investigation of this phenomenon in proton-rich nuclei. Macroscopically this so-called Pygmy strength could be interpreted with the resonant dipole oscillation of a proton-skin against an isospin-symmetric core. For nuclei like ^{32}Ar the occurrence of pronounced dipole strength is predicted in the low-energy region between 8-10 MeV excitation energy. For the ^{34}Ar the pygmy strength is expected to drop sharply and vanish entirely for the N=Z nucleus ^{36}Ar . Using the Coulomb excitation method in inverse and complete kinematics at the LAND/R3B setup at GSI Helmholtzzentrum für Schwerionenforschung GmbH in Darmstadt, Germany, an experiment using radioactive ^{32}Ar and ^{34}Ar beams has been performed. The isotopes were obtained via fragmentation of a 825 AMeV primary ^{36}Ar beam on a 6.347g/cm^2 Be target. The produced proton-rich projectiles with a similar mass-to-charge ratio were separated from the primary beam and from other reaction products in flight using the Fragment Separator FRS. The selected and identified proton rich isotopes with a remaining energy of 650 AMeV were subsequently directed to a lead target of the LAND/R3B setup placed in Cave C. In order to determine the excitation energy after projectile excitation on the Pb target, all the products of the decay from the resonance are detected and identified (fragments, protons and gammas). The reconstruction of the excitation energy for one- and two-proton emission channels for ^{32}Ar and ^{34}Ar were derived from the particles momenta using the invariant mass technique in an event-by-event mode, allowing for an investigation of dipole strength appearance. After the experiment, all the detectors have been calibrated and the Coulomb dissociation cross section for one and two proton emission were determined with two different techniques, which are in good agreement. The data provide first evidence for the existence of low-lying dipole strength in ^{32}Ar , while no low-lying strength is observed in ^{34}Ar . However, further analysis is necessary in order to define the details and interpretation of the appearance of the low-lying strength dipole in ^{32}Ar .

Zusammenfassung

Die vorliegende Arbeit berichtet über die Untersuchung der tiefliegenden Dipolstärke in den protonenreichen Nukliden ^{32}Ar und ^{34}Ar . Frühere Untersuchungen der tiefliegenden Dipolstärke in neutronenreichen Kernen und deren Interpretation bezüglich grundlegender Kerneigenschaften (symmetry energy, skin thickness) initiieren die Untersuchung dieses Phänomens bei protonenreichen Nukliden. Makroskopisch gesehen könnte diese sogenannte Pygmy-Stärke als Dipolschwingungen einer Protonenhaut gegenüber eines isospinsymmetrischen Kernes interpretiert werden. Für Nuklide wie ^{32}Ar wird das Auftreten einer ausgeprägten Dipolstärke in der niederenergetischen Region zwischen 8-10 MeV vorhergesagt. Für den Kern ^{34}Ar wird erwartet, dass die Pygmy-Stärke scharf abfällt und im Falle des N=Z Kerns ^{36}Ar komplett verschwindet. Unter Anwendung der Coulombanregungsmethode in inverser und kompletter Kinematik wurde ein Experiment mit radioaktiven ^{32}Ar und ^{34}Ar Strahlen am LAND/R3B Aufbau am GSI Helmholtzzentrum für Schwerionenforschung GmbH in Darmstadt, Deutschland, durchgeführt. Die Isotope wurden durch Fragmentation eines 825 A MeV ^{36}Ar Primärstrahles an einem Be Target mit einer Massenbelegung von 6.347g/cm² erzeugt. Die produzierten protonenreichen Projektile mit einem ähnlichen Masse zu Ladungsverhältnisses wurden im Flug mit dem Fragment Separator FRS vom Primärstrahl und anderen Reaktionsprodukten separiert. Die ausgewählten und identifizierten protonenreichen Isotope mit einer Restenergie von 650 A MeV wurden anschliessend auf ein Bleitarget des LAND/R3B Aufbaus in Cave C gelenkt. Um die Anregungsenergie der Projektile nach Anregung im Pb Target zu bestimmen wurden alle Produkte, die aus dem Zerfall der Resonanz stammen, detektiert und identifiziert (Fragmente, Protonen und Gammas). Die Anregungsenergie für Kanäle mit ein und zwei Proton Emission von ^{32}Ar und ^{34}Ar wurde aus den Teilchenimpulsen, basierend auf der invarianten Masse Technik event by event rekonstruiert und erlaubt das Auftreten von Dipolstärke zu untersuchen. Nach dem Experiment wurden alle Detektoren geeicht und der Wirkungsquerschnitt der Coulombdissoziation für ein und zwei Protonemissionen mittels zweier unterschiedlicher Methoden bestimmt, welche in guter Übereinstimmung sind. Die gelieferten Daten zeigten erste Hinweise für die Existenz einer tiefliegenden Dipolstärke in ^{32}Ar , wohingegen keine tiefliegende Stärke in ^{34}Ar beobachtet werden konnte. Jedoch sind weitere Untersuchungen notwendig um die Details und Interpretation der tiefliegenden Dipolstärke in ^{32}Ar genauer bestimmen zu können.

Contents

1	Introduction	1
2	Giant Resonances	6
2.1	Classification and General Properties	6
3	Basic considerations	11
3.1	Coulomb excitation	11
3.2	Basic theoretical approximations	12
3.3	Weizsäcker-Williams formalism	13
3.4	Semiclassical approach	15
3.5	Experimental approach	16
3.5.1	Momentum reconstruction	17
3.5.2	Invariant mass	18
4	Experimental Facility and R3B/LAND Setup	21
4.1	Beam transportation	21
4.2	The Fragment Separator FRS	22
4.3	Experimental Setup	23
4.4	Data acquisition system	26
4.4.1	Signal preparation	26
4.4.2	Trigger construction	26
4.5	Detectors before the Target	27
4.5.1	S2 and S8 detectors	27
4.5.2	POS detector	28
4.5.3	PSP detectors (PSP1/PSP2)	28
4.5.4	Veto detector	29
4.6	Detectors after the Target	31
4.6.1	Scintillating GFI1/GFI2 detectors	31
4.6.2	New ToF Wall (NTF)	32
4.6.3	Proton Drift Chambers (PDC1/PDC2)	32
4.6.4	Big ToF Wall (TFW)	34
4.7	Detectors around the Target	34
4.7.1	Crystal Ball (XB)	34
4.7.2	Silicon STrip detectors (SST1/SST2)	36

5	Calibration	39
5.1	Calibration within the <i>land02</i> package	39
5.2	Internal calibration of the scintillator paddles	40
5.2.1	Time reconstruction	41
5.2.2	Energy reconstruction	42
5.2.3	Crossed paddles algorithm	42
5.3	Calibration of the individual detectors	43
5.3.1	ToF Walls: NTF and TFW	43
5.3.2	GFI and PSP position calibration	46
5.3.3	Proton Drift Chamber (PDC)	51
5.3.4	Calibration of the gamma detector	54
5.3.5	Hit Reconstruction	55
5.4	Stability of the calibration parameters	57
5.4.1	Possible NTF issues	58
5.5	Incoming beam calibration	60
6	³²Ar and ³⁴Ar data evaluation	63
6.1	Projectile	63
6.1.1	Mass identification	63
6.1.2	Charge identification	64
6.1.3	Selection of incoming projectiles	64
6.2	Outgoing Channels	66
6.2.1	Fragment Detection	66
6.2.2	Magnetic field	67
6.2.3	Tracking through ALADIN	68
6.3	Acceptance corrections	71
6.4	Efficiency of the proton arm	72
6.5	γ -ray contribution	77
6.6	Background contamination	80
7	Results and Discussions	83
7.1	Excitation energy spectra	83
7.2	Coulomb excitation cross sections	84
7.3	Low-energy excitation	90
8	Summary and outlook	93
	References	95
	Acknowledgment	101

List of Figures

1.1	The prediction of remaining pygmy dipole strength (PDR) below the giant resonance (GDR) region in proton-rich ^{32}Ar is presented in the left panel (the dipole strength distribution as a function of the excitation energy is shown). Right panel illustrates proton and neutron densities where the lowest is for the state in the giant dipole at 18.01 MeV and upper is the state in the pygmy resonance the range 8.3 - 9.6 MeV [10].	3
1.2	Schematic view of the decay modes of the ^{32}Ar in collisions with ^{208}Pb . Due to the low separation energies, the higher proton evaporation channels can be observed. . .	4
2.1	The main modes of the giant resonances.	7
3.1	Coulomb excitation process between a projectile (Ar) and a target nucleus (Pb). The argon projectile impinges towards the lead target with an impact parameter b	14
3.2	Virtual photon numbers for ^{32}Ar projectile impinging on a ^{208}Pb target with 650 AMeV as a function of photon energy for three multipolarities. The E1 (solid red line), M1 (dashed blue line) and E2 (dashed black line) virtual photon fields are represented.	16
4.1	Layout of the accelerator facility at GSI, showing the linear accelerator UNILAC, the heavy-ion synchrotron SIS, the Experimental Storage Ring ESR and the FRagment Separator FRS.	22
4.2	Schematic of the FRS setup with the primary target area. The secondary ions produced after the interaction fragmented incoming beam coming from SIS with the target placed at the entrance of FRS are selected and identified by the FRagment Separator before coming to the Experimental Hall in the Cave C [11].	23
4.3	Schematic view of the R3B/LAND experimental setup in Cave C. The setup provides full kinematics measurements. Selected secondary beams are sent to the secondary Pb target, placed in the center of the Crystal Ball. The heavy reaction fragments are deflected to the different angles by the ALADIN dipole magnet and further detected by fibre detectors (GFI), placed after the magnet and a small ToF Wall (NTF). Protons are detected by drift chambers (PDC1, PDC2), Si-strip detectors and Big ToF Wall (TFW), while γ rays are detected by the Crystal Ball array.	25
4.4	Schematic of the electronics with the time- and energy- readout modules.	27
4.5	The POS detector which is mainly used for timing purposes.	30
4.6	The Position sensitive PIN diode is readout by four anodes Q_1, Q_2, Q_3, Q_4 and by a cathode Q from the back side of the detector.	30

4.7	Schematic of the scintillating fiber detector (left) and the mask (right) to guide the fibres on the PSPM cathode [55].	31
4.8	Schematic of the New ToF Wall used for the detection of the heavy reaction products.	32
4.9	The schematic of one layer of the drift chamber and procedure of the electrical signal reordering. The sense wire anodes surrounded by cathode wires (field wires) forming a hexagonal structure. The inter-wire distance of 0.7 cm.	33
4.10	The big Time of Flight Wall for the detection of light particles, e.g. protons.	34
4.11	Crystal Ball γ -ray detector. The picture show a view of opened (bottom) and closed detector (top).	35
4.12	A single Silicon STrip detector with its front-end-electronics board (green part). Total 1024 strips are grouped in 10 visible and 6 (rear side) blocks of 64 read-out lines each, which strips are capacitively connected to 10+6 VA chips with pre-processing on the front-end board. The active area is rectangular with $4 \times 7 \text{ cm}^2$ with 640 vertical and 384 horizontal strips. The detector is used for the reconstruction of the position.	37
5.1	Schematic structure of the <i>land02</i> framework. Calibration levels are shown inside boxes with a short description of each steps.	40
5.2	Schematic view of a single scintillator paddle. The position of the hit in the paddle can be reconstructed using the time and energy signals measured by the two PM tubes at the edges of the paddle. The time and energy signals measured by each PM depend on the distance of the hit (x) to the edges of each paddle.	41
5.3	Typical example of the pedestal distribution of one channel NTF detector.	44
5.4	The time calibrator (Tcal) events. A linear correlation is plotted between the time presented in nanoseconds (Tcalt) and time in channels from the TDC.	46
5.5	The time of the NTF detector before (top) and after (bottom) the synchronization. The time of the hit in the NTF detector is derived from each photomultiplier of each paddle (TCAL, SYNC levels). The blue spectra represents the time from the first PMT1 and black one is from the second PMT2.	47
5.6	The time resolution of the NTF detector is $\sigma = 42.13 \pm 0.34$ picoseconds.	48
5.7	Schematic view of the pixels detector.	49
5.8	The plot of the GFI detector in (ν, ν) coordinates before (top) and after (bottom) gain matching. Each cluster of dots corresponds to a fibre.	50
5.9	Figure shows a reconstructed position correlation between two fiber detectors GFI1 and GFI2. Some bars along the correlation line are coming from wrong position identification.	51
5.10	One layer contains two rows of sense wire anodes and having hexagonal structure cathode wires. To reconstruct the distance the drift lengths r_1 and r_2 derived from the measured drift times are used.	52
5.11	One dimension spectra (top right) presents an example of the reconstructed radius r_1 in cm after the $x(t)$ -curve applied. Top left represents a measured arrival time used to calculate an $x(t)$ -curve. The status of wires for the first drift chamber PDC1 is shown (bottom). One can see two holes in the distribution meaning that two wires are broken.	54

-
- 5.12 Upper left frame of the plot presents an example of the peak fitting for the ^{22}Na (511 keV, 1275 keV), ^{88}Y (898 keV, 1836 keV) and PuC (6130 keV) sources (upper right frame). Red solid lines represent the fit function for the peaks. A background of the function is shown with blue dashed lines. The Gaussian peak component are presented in green dotted lines. The sharp peaks (channel number 4450) at the left side of the spectra can be explained as a reminders of the cut-off pedestals. Bottom right: Energy calibration curve for crystal 131. The linear correlation between the known energies (5 points) of calibration γ -rays and their positions measured in raw QDC channels. The procedure has been done for each individual crystal. Parameters of the linear calibration function, such as gain and offset, are found by linear regression. 56
- 5.13 Dependence of T_{tcal} parameter as a function of data-file number on time. Lower plot (left) shows the example of the drifting channel for paddle 18 of TWF, second PM tube. The rest plots, represents a "normal" motion, common to all channels. 58
- 5.14 Corrected T_{tcal} parameter as a function of data-file number on time. Lower left plot shows an example of pure "anomalous" motion. 59
- 5.15 The energy deposit distribution versus x position for the horizontal paddle 5, using the sweep run. The x position is derived from the time difference as $0.5 \cdot (t_1 - t_2)$. The smiley effect and the spoiled energy distribution is observed during the calibration procedure which is possible to correct. The lower frames show the energy deposit distribution after the corrections are applied. 60
- 5.16 Linear fit of $\beta \Delta t$ versus β for the three different calibration runs. The offset of the linear fit is related to the flight path between S8 detector placed at the FRS and POS counter placed in Cave C. The slope from the fit is related to the time offset due to cabling and electronics. 62
- 6.1 An example of the velocity β for the incoming ^{33}Ar (b), ^{31}Cl (c) and ^{32}Ar (a) isotopes. 64
- 6.2 An example of a two-dimensional identification plot of mass to charge ratio versus Z of the incoming particles. The graphical cut to select ^{32}Ar and ^{34}Ar are shown. . . . 65
- 6.3 Example for incoming ^{32}Ar : Correlation of the energy loss between the Silicon STrip detector placed before the ALADIN magnet and NTF located behind the magnet. Looking to the left part of the NTF distribution one can see a long tail which comes from the secondary break-up reactions occurring between these two detectors. Such events occur with different charges in the NTF but one energy on the SST. Z corresponds to the primary ^{32}Ar beam, $Z - 1$ and $Z - 2$ are reaction products after photodissociation and emission of 1 and 2 protons, respectively. The energy loss information gives a possibility to make a clean cut on the outgoing channels. 67
- 6.4 The magnetic field components of the ALADIN magnet are shown. The main y-direction of the field is clearly prominent if all particle pass the field in the x-z plane. 68

6.5	The plot shows an example of the reconstructed detectors hits of fragment and 2 protons by the tracker algorithm. The green lines represents the track of the heavy fragments while the red lines represent proton tracks. The blue crosses indicate the measured positions of the particles in the various detectors. Starting from the middle of the target, the SSTs detectors placed before the magnetic field, the GFIs and the NTF detectors used to track the heavy fragment are shown. The PDC drift chambers and the big ToF wall (TFW) are used to track protons.	69
6.6	The plot shows an example of mass distribution for non-interacting ^{32}Ar (top) and ^{34}Ar (bottom) isotopes passing Pb target. Expected peak positions for non-reacted ^{32}Ar and ^{34}Ar to be at 32 and 34 respectively proves the proper working tracking algorithm. The mass resolution is around 0.8%.	70
6.7	Fragment mass distributions for $^{32}\text{Ar}(\gamma, 2p)$ (left) and $^{34}\text{Ar}(\gamma, 2p)$ (right) reaction channels after the tracking through the ALADIN magnetic field.	71
6.8	The x-residual position resolutions for the fragment (top left) and protons (bottom left) on the SST1 are shown. Due to the narrow position distribution for the fragment, the resolution as expected is much better ($\sigma = 0.02$ mm) compare with the protons. The projection on the x-axis (bottom right) shows a visible acceptance cut of the protons in y-direction due to the limited opening angle of the beam in y-direction behind the target. The correlation between the transversal p_y^\perp component and the y-position on the first drift chamber (top right) shows a place where two wires are missing.	72
6.9	Experimental setup in the R3BROOT simulation package. Protons (red line) are tracked as well as fragments (white line) from different reactions.	73
6.10	Protons with high excitation energies are deflected to larger angle and stopped in the ALADIN wall. It reduced the proton acceptance.	73
6.11	Acceptance curves for the one proton and two proton channels of incoming ^{32}Ar (left) and ^{34}Ar (right) respectively. Each curve starts from the certain specific energy separation threshold. The red curves describe one proton emitted in the reaction and the blue curves show the two proton cases.	74
6.12	The combination of the proton efficiency detection. The total number (N_{total}) of events requires hits in all detectors (see case 1). Then the number of proton hits in each individual detector layers (unpacked in DHIT level) is counted by requiring that some events are missed in one plane of the detectors (see case 2, 3, 4).	74
6.13	The correlation between two drift chambers PDC1 and PDC2 required to reduce the background.	75
6.14	The simulation of the x-ray background have been performed and compared with the experimental data. The experimental (black line) and simulated (red line) x-ray background from the Crystal Ball are compared for the ^{32}Ar isotope.	78
6.15	The γ -sum spectra represent $2^+ \rightarrow 0^+$ transitions in ^{30}S and ^{32}S ions. The background (red) is derived using the non-reacted beam and scaled to the number of incoming particles.	79

6.16	Mass distribution for $^{32}\text{Ar}(\gamma, 2p)$ (bottom) and $^{34}\text{Ar}(\gamma, 2p)$ (top) reactions channels in Pb (red line) and C (blue line) targets. The main peaks around the ^{30}S and ^{32}S are obtained using the cuts on outgoing fragment masses. The second peaks around the ^{29}S and ^{31}S coming from the nuclear reaction also contribute.	81
6.17	An example of the mass distribution for $^{32}\text{Ar}(\gamma, 2p)$ reactions channels after applying the experimentally derived α_{Pb} . The peak coming from the nuclear contribution vanishes meaning that the integrals of ^{29}S is equal to 0.	82
7.1	The energy of different isotopes for ^{32}Ar case. Due to the fact that ^{31}Cl has no bound excited state the excited ^{32}Ar isotope decays mostly via two (or more) proton emission.	83
7.2	The histograms represent excitation energy distributions for ^{32}Ar isotope measured with lead (top), carbon (middle) and empty targets (bottom). Neither efficiency and acceptance corrections nor γ -ray contributions were applied to the spectra.	85
7.3	The excitation energy distributions for $^{32}\text{Ar}(\gamma, 2p)$ (bottom) and $^{34}\text{Ar}(\gamma, 2p)$ (top) isotopes measured with the lead target. The black dots represent the pure spectra and the red ones - the spectra with included γ -ray contribution. Neither acceptance nor efficiency correction were applied to the spectra.	86
7.4	^{32}Ar excitation energy distribution reconstructed from the data measured with lead target in one-proton (top left) and two-protons (top right) channels and as well as for ^{34}Ar in one-proton (bottom left) and two-protons (bottom right). Efficiency and acceptance corrections are applied. Since for $^{32}\text{Ar}(\gamma, p)$ reaction, the number of measured γ -rays is less than 4% of all data, they are not added. For $^{32}\text{Ar}(\gamma, 2p)$ reaction the γ -sum energy is added. Statistical errors are displayed.	87
7.5	$^{32}\text{Ar}(\gamma, 2p)$ mass spectrum for the Pb target before the subtraction of background. The main peaks around ^{30}S is obtained using the cut on an outgoing fragment mass. The second peak around the ^{29}S is produced from the nuclear reactions. The tail of the peak at larger mass appears from contamination of the cut and presents a wrongly tracked neighboring reaction channel.	89
7.6	The mass distribution for the $^{32}\text{Ar}(\gamma, 2p)^{30}\text{S}$ (right) and $^{34}\text{Ar}(\gamma, 2p)^{32}\text{S}$ (left) reactions. The mass spectra are normalized to the numbers of incoming projectiles. After scaling and subtraction of nuclear contribution and background, the Coulomb cross sections spectra are obtained.	91
7.7	Excitation energy distributions for ^{32}Ar (top) and ^{34}Ar (bottom) isotopes, where both 1p- and 2p-reaction channels were summed up.	92

Chapter 1

Introduction

For many decades the electromagnetic interaction has been established as a versatile tool for nuclear physics studies. Not only is it the best understood among all four fundamental interactions, but also the large enough strength of the electromagnetic interaction allows to cause observable effects of the charge and the current distributions in a nucleus. Both in theory and experiment the electromagnetic interaction made by far the most dominant contribution in understanding the structure of nuclei.

Already in early studies of nuclear reactions the possibility of exciting atomic nuclei by means of the electromagnetic field of impinging charged particles has been investigated [1] and an excitation cross section has been expressed by applying a classical treatment of the trajectory of the bombarding particle [2]. Thus, the excitation cross section was derived as a function of the energy, mass and charge of the projectile. Later the discovered process, which is nowadays named Coulomb excitation, was developed for the investigation of low-lying rotational and vibrational nuclear states. Using higher bombarding energies, the excitation of higher energy states has been investigated as well. However, in these early Coulomb excitation experiments only light ions such as protons or α particles were used as projectiles and consequently the electromagnetic force affecting the target was too weak and only a few nuclear states could be populated. The later developed accelerators for heavy ions allowed the possibilities to perform more effective and complex Coulomb excitation experiments where due to the strong electromagnetic field from heavy projectiles the target nucleus can absorb several quanta and thus many nuclear states can be readily populated [9]. This complex Coulomb excitation process provides an opportunity to devise a variety of experiments where to study the electromagnetic properties of nuclear states. For a long time the principle of measurements was limited to only stable beams and targets. Further advances in nuclear physics research allowed for reaction studies using radioactive beams and that has given opportunities to extend experimental studies of nuclear structure from the valley of stability to the nuclear drip-lines. Since radioactive beams became available, the big interest is focused on performing experiments with exotic nuclei, which open up a wide knowledge about nuclear structure.

The experimental studies with nuclei close to the proton or neutron drip-line will help to understand the properties of exotic nuclei. In particular there is a big lack of nuclear structure information in the low-mass region. Close to the drip-lines, where

the separation energies become low and the capture cross-sections are mainly governed by only a few low-lying resonances, statistical models are not useful anymore and detailed description of level energies, spin-parity assignments, Q -values and reaction cross-sections are needed. The research centers that have been built during last decades, among which are RIKEN (Japan), CERN (Switzerland), NSCL (USA) and GSI (Germany), opened up new opportunities for above mentioned and many more experimental studies.

The measurements presented in this thesis are concerned with a study of dipole strength distribution in proton-rich nuclei, namely $^{32,34}\text{Ar}$. This investigation was proposed by the R3B/LAND Collaboration at the GSI Helmholtzzentrum für Schwerionenforschung GmbH. The main goal of this experiment is to search for signatures of the predicted Pygmy Dipole Resonance (PDR) in a neutron-deficient nuclear isotopes. Appearance of the low-lying pygmy dipole resonance in proton-rich nuclei is related to the formation of the proton skin. The proton pygmy resonance, from the macroscopical point of view, is predicted to be a low-lying transition, lying below the Giant Dipole Resonance (GDR), which is interpreted as oscillation of proton skin against the isospin saturated core, justified by theoretical transition density and current distributions related to the dynamics of excited nucleons. It belongs to the certain excitation energy range in the neighborhood of the proton separation threshold. Since the proton-drip line is much closer to the line of β -stability than the neutron drip-line, bound nuclei with an excess of protons over neutrons can be found only in the light and medium mass proton-rich nuclei. Study of the PDR is interesting not only as a new exotic mode of nuclear excitation but it also may have an important impact on the understanding of certain astrophysical phenomena. The giant dipole resonance is the best known dipole mode, since it is easy to selectively excite by means of photo-nuclear reactions. The phenomenon of GDR in stable nuclei is well understood from both, the macroscopic and microscopic points of view. However, theoretical calculations as well as experimental results indicate that extreme structural differences can be expected between exotic and stable nuclei. Therefore, further studies of these phenomena are required.

The GSI Helmholtzzentrum für Schwerionenforschung GmbH in Darmstadt is a scientific centre for the research on heavy ions. Here the study of the electromagnetic excitation of a secondary, high energy beam of unstable nuclei in a high- Z target have been preformed for neutron-rich nuclei (see [7, 8] and references therein). And an occurrence of a neutron pygmy dipole resonance was confirmed using kinematically complete experiments with R3B/LAND setup. The earlier experimental studies of the observation of the low-lying strength below the giant dipole resonance were already performed using the complete experimental apparatus for the stable nuclei $^{44,48}\text{Ca}$, ^{208}Pb [3], [4], [5] and neutron-rich nuclei like $^{20,22}\text{O}$ [6] and $^{130,132}\text{Sn}$ [7, 8].

For the proton-rich nuclei the situation is different since the proton drip-line is much closer to the β -stability than the neutron drip-line and nuclei with an excess of protons over neutrons are found only for nuclei with $Z < 50$. Due to the presence of a high Coulomb barrier, which holds the protons in, nuclei do not exhibit a pronounced proton skin, except for very light elements. Taking into account that in light nuclei, the multipole response is less collective, all these effects seem to preclude the formation of

proton pygmy states. Nevertheless, Paar, Vretenar and Ring [10] showed in their recent calculations, that a proton pygmy resonance should develop in nuclei of mass numbers $A = 30-50$ located close to the proton drip line. They performed the calculation for the chain of even-even proton-rich Ar isotopes where, for example, for nuclei like ^{32}Ar the occurrence of pronounced dipole strength is predicted in the low-energy region between 8-10 MeV excitation energy. For the ^{34}Ar the pygmy strength is expected to drop sharply and vanish entirely for the $N = Z$ nucleus ^{36}Ar (see fig. 1.1). Different models have been used to study this new collective mode, from hydrodynamic models to shell-model calculations via mean-field plus random phase approximation (RPA). The occurrence of the PDR lying below the giant dipole resonance in proton rich $^{32,34}\text{Ar}$ nuclei was analyzed in the framework based on the Relativistic Quasiparticle Random Phase Approximation (RQRPA). The dipole strength located close to the particle-emission threshold is a general feature in many isospin asymmetric nuclei. The appearance of this mode is currently much under debate and subject to theoretical and experimental investigation. The left panel of figure 1.1 shows the low-lying strength at excitation energies between 8-10 MeV. The right panel shows the transition densities where in contrast to the isovector giant resonance at 18 MeV, the proton and neutron transition densities of the pygmy state vibrate in phase inside the nucleus.

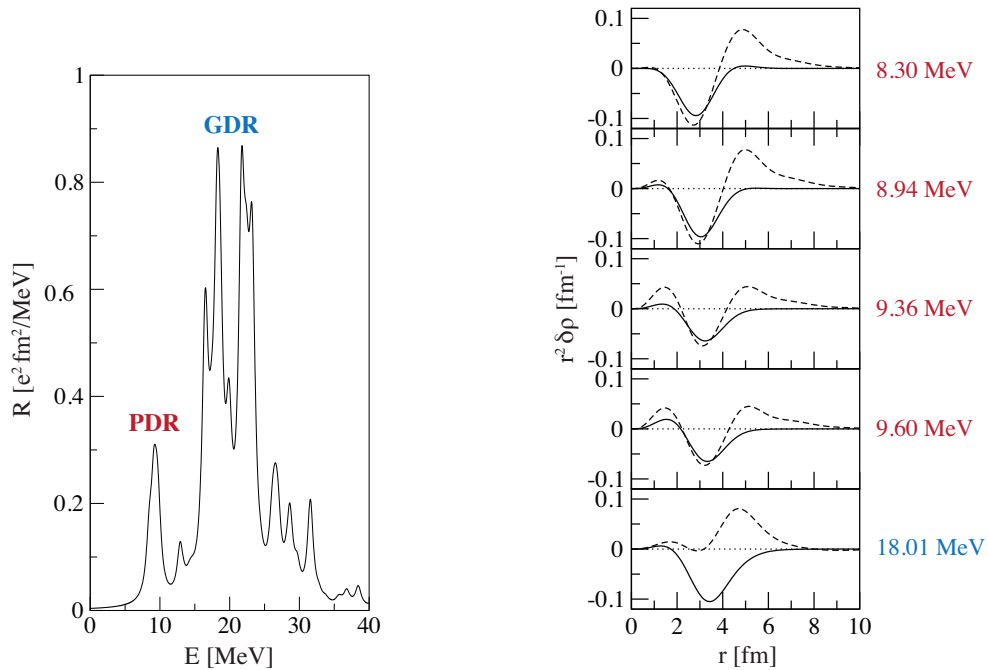


Figure 1.1: The prediction of remaining pygmy dipole strength (PDR) below the giant resonance (GDR) region in proton-rich ^{32}Ar is presented in the left panel (the dipole strength distribution as a function of the excitation energy is shown). Right panel illustrates proton and neutron transition densities where the lowest is for the state in the giant dipole at 18.01 MeV and upper is the state in the pygmy resonance the range 8.3 - 9.6 MeV [10].

^{32}Ar is the lightest known argon isotope with a half life of $t_{1/2} = 98 \pm 2$ ms. The

proton separation thresholds for one proton and two proton separation are $S_p = 2.4$ MeV and $S_{2p} = 2.7$ MeV, respectively. Since the proton separation thresholds ($S_{p,2p}$) are much lower than the neutron separation thresholds ($S_n = 21.5$ MeV) for ^{32}Ar , the decay from the excited levels in the considered energy range will be mostly achieved by proton emission. That is also true for the most part of giant resonance centered at an excitation energy of 18 MeV. The main part of the excited ^{32}Ar nuclei decay via two proton emission to ^{30}S (see fig. 1.2) because there is no bound excited state in ^{31}Cl . However, direct decays to the ground state of ^{31}Cl can also be observed.

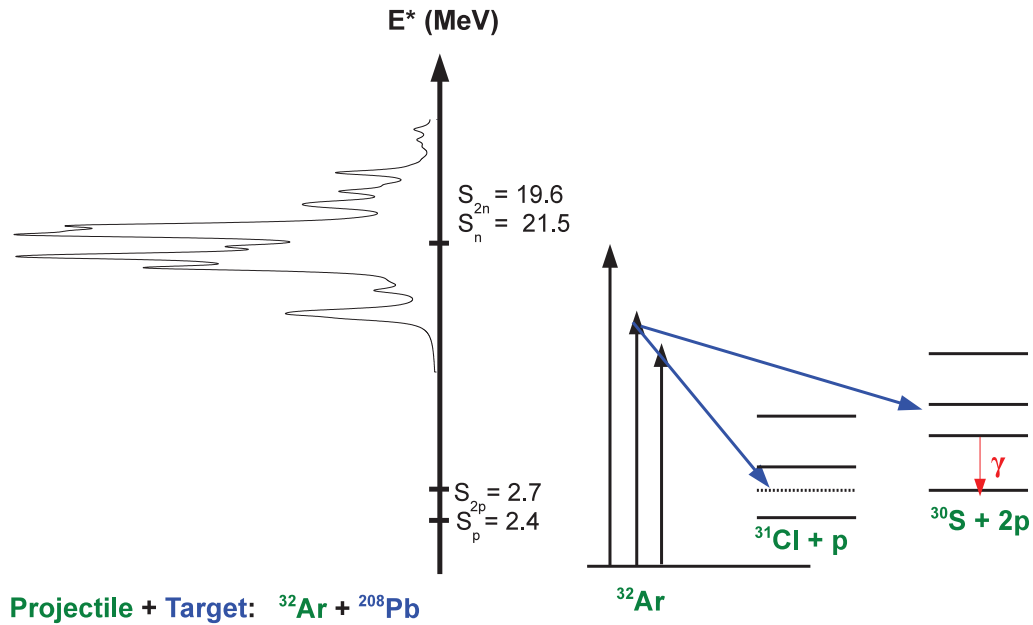


Figure 1.2: Schematic view of the decay modes of the ^{32}Ar in collisions with ^{208}Pb . Due to the low separation energies, the higher proton evaporation channels can be observed.

The major part of this thesis involved the calibration procedure along with analysis of the experiment performed with the R3B/LAND facility at GSI-Darmstadt, in August 2008. One proton and two proton channels of reactions of the proton-rich ^{32}Ar and ^{34}Ar nuclei were studied via Coulomb dissociation in inverse kinematics at 650 A MeV projectile energy, and integrated differential cross-sections were determined. Coulomb dissociation is a unique way to study the photo-excitation of exotic nuclei since experiments with real photons are impossible for short-lived nuclei. However, in order to derive the photo-absorption cross section from the Coulomb excitation cross section, the response of the nuclei has to be compared using direct and indirect measurements.

In this work, the results for the obtained excitation energy and integrated cross sections are presented. Some additional resonances in the excitation energy range from 6 to 10 MeV were observed. The analysis of the presented data has to be complemented with a decay model allowing for an interpretation of the 1p- and 2p-decay data with respect to the appearance of low-lying strength. That, however, requires an additional investigation and goes beyond the scope of this thesis.

The thesis is organized in the following way. The general properties of the giant dipole resonances and a brief overview of the experimental methods used to study the dipole resonances in nuclei are presented in chapter 2. The experimental techniques relevant for the Coulomb dissociation method, such as the virtual photon theory and the expression of the invariant mass formula used to calculate the excitation energy of the resonance, are presented in chapter 3. In chapter 4, the experimental facility at GSI-Darmstadt is described. Also the R3B/LAND experimental setup used to obtain the present data along with electronics and the data acquisition system (based on a trigger decision) are described. Chapter 5 is dedicated to the setup and detection system calibration needed before any physical data can be extracted. The data analysis procedure and the particles tracking through the ALADIN magnet after the reaction target are discussed in chapter 6. The obtained integrated Coulomb excitation cross sections for the reaction channels of interest are presented in chapter 7.

Chapter 2

Giant Resonances

A giant resonance corresponds to a collective nuclear excitation in which an appreciable fraction of the nucleons moves coherently together. The occurrence of such collective motions is a common feature of many-body quantum systems. During the last few decades, the experimental and theoretical studies brought a clear understanding of the giant resonance phenomena in stable nuclei in terms of macroscopic and microscopic models [17]. The first identification and investigation of the giant resonance was made by Bothe and Gentner [14] (1937). They used photons of 17.6 MeV from the reaction ${}^7\text{Li}(p, \gamma)$ in several targets. Later in 1944 the phenomenon was expressed as an oscillation of the protons against the neutrons in the nuclei (the isovector giant dipole resonance) [15]. The observation was confirmed by Baldwin and Klaiber [12] in 1947 by using Bremsstrahlung from the 100 MeV betatron to excite a uranium target. They measured the fission yield for photon energies in the range of 10-100 MeV and observed a prominent peak in the cross section for photons of about 20 MeV. In 1948 Goldhaber and Teller [16] interpreted this resonance with a hydrodynamical model where all the protons in the nucleus move collectively against all the neutrons creating an electric dipole moment. Since then, the GDR has been systematically studied for almost all stable nuclei. Other resonance modes were observed as well, contributing to a systematic view of the giant resonances within the liquid-drop model which were classified according to their multipolarity L , isospin T and spin S quantum numbers (see figure 2.1).

2.1 Classification and General Properties

The giant monopole resonance (GMR), $\Delta L = 0$, is a density oscillation consisting of cyclic phases of compression and expansion. The giant quadrupole resonance (GQR), $\Delta L = 2$ is a surface oscillation. The dipole resonance (GDR), $\Delta L = 1$, is a shape or density oscillation which can be considered as a damped oscillation of the protons against the neutrons. The qualitative structure of the giant dipole resonance and of other multipole resonances follows from the microscopic harmonic oscillation model. The oscillation of the nucleons can be either in-phase or out-of-phase and have electric/magnetic modes according to the ΔT and ΔS :

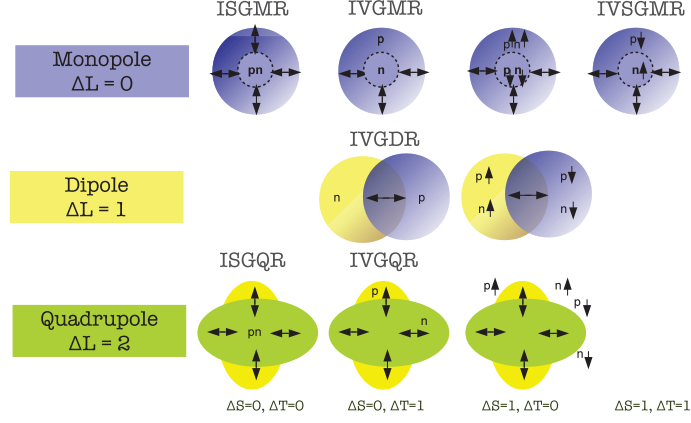


Figure 2.1: The main modes of the giant resonances.

- $\Delta T = 0$
Giant Dipole Resonance has Isoscalar vibration (ISGDR) in which the neutrons oscillate in phase with protons.
- $\Delta T = 1$
Giant Dipole Resonance has Iovector vibration (IVGDR) in which neutrons and protons oscillate out of phase against each other.
- $\Delta S = 0$
These modes are electric (E) where nucleons vibrate following a multipole pattern given by L .
- $\Delta S = 1$
These modes are magnetic (M) where nucleons with spin \uparrow vibrate against nucleons with spin \downarrow , following a multipole pattern given by L .

Since the separation of proton and neutron distributions need to have an additional energy, for the same multipolarity the isovector modes are always higher in excitation energy than the isoscalar modes. In case this oscillation is coupled to an electromagnetic field, the shape of the resonance can be approximated by a Lorentzian distribution:

$$\sigma(E) = \frac{\sigma_m \Gamma_m^2 E^2}{(E^2 - E_m^2)^2 + \Gamma_m^2 E^2}, \quad (2.1)$$

where σ_m , Γ_m and E_m are the peak cross section, the resonance width and the resonance energy of the peak of the distribution, respectively. These parameters of the distribution are smooth functions of the nuclear mass A , meaning that the GDR resonance energy decreases gradually with increasing mass number. This mass dependence can be reproduced using the following semi-empirical formula:

$$E_m = 31.2A^{-1/3} + 20.6A^{-1/6}(\text{MeV}). \quad (2.2)$$

This expression proposed for the E_m in order to calculate the peak energy for any mass number A in the validity range of the models. In one of the models, the proton fluid vibrates against the neutron fluid and the restoring force is proportional to the volume energy coefficient of the Bethe-Weizsäcker mass formula. This model provides the energy of the vibration to be proportional to $A^{-1/3}$. Goldhaber and Teller [16] proposed a model based on the oscillation of interpenetrating spheres of protons and neutrons while preserving the center of mass position, leading to the $A^{-1/6}$ dependence. Experimentally it has been shown that the A dependence of the excitation energy of the dipole is intermediate between $A^{-1/3}$ and $A^{-1/6}$, i.e. the GDR is a mixture of density and shape oscillation.

The total cross section for the excitation of the giant dipole resonance is usually compared to the Energy Weighted Sum Rule (EWSR). The EWSR provides a benchmark for the photoabsorption cross section as a model-independent quantity derived from the elementary principles. For electric dipole excitation the energy weighted sum rule, which is also called the Thomas-Reiche-Kuhn sum rule (TRK) [18], can be approximately described as:

$$\int_0^\infty \sigma_\gamma(E)dE \simeq 60 \frac{NZ}{A} [\text{MeV} \cdot \text{mb}], \quad (2.3)$$

where N and Z are the neutron and proton number of the nucleus, $A = N + Z$ is the mass number. The sum rules reflect bulk properties of a system (i.e. size or number of components) and links them to giant resonance parameters. Experimental strength exhibiting a sizable part of EWSR confirms the collectivity of the resonance. Measurements for heavy nuclei revealed that the total cross section values may also exceed the TRK sum rule approximated value. An additional contribution related to the velocity-dependent terms (which are usually neglected) in the nucleon-nucleon interaction can be accounted for in the sum rule derivation.

Since the giant resonances are situated at energies above the particle emission threshold, their total width Γ_{GDR} consists of three different contributions:

$$\Gamma_{total} = \Gamma_{inh} + \Gamma^\uparrow + \Gamma^\downarrow, \quad (2.4)$$

where Γ_{inh} is a damping width which occurs from the fragmentation of the particle-hole (p-h) strength due to shell structure effects and mainly apparent in light nuclei. Γ^\uparrow is an escape width which appears due to the coupling of the resonant state to the continuum which gives rise to the direct decay of a particle into hole states of the residual nucleus. It is the dominant contribution for light nuclei. Γ^\downarrow is a spreading width and

arises from the coupling of the resonant states to nuclear compound states, eventually leading to the emission of low-energy particles. If the mass number A is increasing, the decay proceeds via mixing with more complicated states and for heavy nuclei the total width will be dominated by the spreading width [17]. Giant resonances can be viewed as a coherent superposition of many particle-hole states. One of the most commonly used many-body theory for modeling of collective excitations is based on the mean-field approach, *Random Phase Approximation* (RPA) [19, 20, 21, 22]. This model describes the excitations of the ground state in terms of particle-hole (p-h) excitations. The mean-field calculations result in a single particle structure of a nucleus. In turn, the collective phenomena are introduced to the system by adding residual two-body (p-h) interaction which is not accounted for in the mean-field potential. The residual interaction is responsible for mixing of many unperturbed p-h states and an additional highly correlated state is created. This constructive superposition of p-h states is significantly shifted up or down in excitation energy depending on the interaction properties and absorbs almost all available transition strength revealing a collective character. The rest of the strength is shared by other, non-collective solutions of the RPA equations which are closely related to original p-h excitations.

Chapter 3

Basic considerations

3.1 Coulomb excitation

Coulomb excitation is a process of inelastic scattering in which a charged particle transmits energy to the nucleus through the electromagnetic field. This process can appear at a much lower energy than that necessary for the particle to overcome the Coulomb barrier; the nuclear force is, in this way, excluded in the process. Commonly, targets of the stable nuclei are bombarded with heavy ions at energies so low that the Coulomb repulsion prevents the two nuclei from touching each other, assuring thus a pure Coulomb interaction process without nuclear contribution. However, this method may not be appropriate anymore to study so-called exotic nuclei. These are nuclei far from stability and thus cannot be formed into targets due to their short lifetimes. In order to investigate such nuclei Coulomb excitation in inverse kinematics is used at energies below or above the Coulomb barrier, depending on their production mechanism. The exotic beam particles are scattered off a stable target and detected in coincidence with γ -rays, tagging an inelastic scattering process. In the present experiment the nuclei of interest (argon) impinged on a target with high atomic number (Pb). If the projectile is excited into an unbound state, the process is called Coulomb dissociation. For relativistic projectile energies (700 - 1000 AMeV) the reaction products are kinematically focused in the forward direction and their velocities are the same as the beam velocity. In 1924, Fermi introduced an idea that led to what is now known as the Weizsäcker-Williams formalism [64]. He described the process of electromagnetic excitation due to a moving charged particle within a non-relativistic approach, that allowed to derive the frequency (or energy) spectrum based on a time-varying electric field. Later on, Weizsäcker and Williams extended this formalism taking relativistic effects into account [63].

3.2 Basic theoretical approximations

Sommerfeld parameter

The strength of the interaction between the projectile and the target nucleus is described by the dimensionless quantity

$$\eta = \frac{a}{\lambda/2\pi} = \frac{Z_1 Z_2 e^2}{\hbar \nu_p}, \quad (3.1)$$

where a is half the distance of closest approach in the collision and equal $Z_1 Z_2 e^2 / m_o \nu_p^2$. ν_p is the velocity of the projectile, λ is the wavelength of the projectile. In case when the Sommerfeld parameter η is much larger than unity ($\eta \gg 1$), one may describe the motion of the projectile and target nuclei in a non-relativistic theory and the trajectories of these nuclei are considered as classical Rutherford trajectories (see description below). Since relativistic velocities of the interacting particles are used in the present experiment, relativistic theory is used where $\eta \ll 1$ for small scattering angle.

Straight-line approach

In the theory of Coulomb excitation the projectile nuclei are assumed to follow classical trajectories. For the relativistic case, the projectile scattering angle θ in the laboratory reference system can be expressed with the help of the Rutherford formula

$$\theta_{lab} = \frac{2Z_1 Z_2 e^2}{\gamma m_1 \nu_1^2 b} \quad (3.2)$$

where b is the impact parameter for the electromagnetic interaction, ν is the velocity and $m_1 = A_p \nu$ is the mass of the projectile, Z_1 and Z_2 are the corresponding charge of the projectile and target, γ is the Lorentz factor and e is the unit charge. The distance between the interacting nuclei is considered to be large compared to their radii. Using the Rutherford equation, the detected angle is approximately zero. Hence, this angle can be neglected and an assumption of a straight line trajectory is considered. The Rutherford approach is applied in order to derive experimental cross section and compare it with theory. In order to include the process of the projectile interaction with the time-dependent electromagnetic field of the lead target, the different approaches are considered. The main idea is to consider the electromagnetic transition in the isotope from a initial state to a final excited state and connect it with the measured differential cross section.

Minimum impact parameter

Commonly, the electromagnetic cross sections are expressed adopting a minimum impact parameter b_{min} which is closely related to the radii of the interacting nuclei and below which electromagnetic excitation is cut off. The most common parametrization to define b_{min} in the present analysis of experimental data as well as in theoretical

approaches is given by Benesh, Cook and Vary [62] in case of heavy ion collisions. In particular, b_{min} is the distance below which scattered ions remain within the range of nuclear forces and above which interaction is purely electromagnetic. This distance is related to the sum of radii of interacting nuclei as

$$b_{min} = r_0 \cdot \left(A_p^{1/3} + A_T^{1/3} - x \cdot \left(\frac{1}{A_p^{1/3}} + \frac{1}{A_T^{1/3}} \right) \right), \quad (3.3)$$

where $r_0 = 1.34$ fm and $x = 0.75$ are obtained from a fit to experimental nucleon-nucleus and nucleus-nucleus interaction data. A_p is the atomic mass number of the projectile and A_T is the atomic mass number of the target. The calculated minimum impact parameter is $b_{min} \approx 11.7$ fm.

Maximum excitation energy

With an energy around 650 AMeV of the colliding nuclei and the impact parameter 11.7 fm, the maximum excitation energy is $E_{max} \approx 23.5$ MeV calculated as

$$E_{max} = \frac{\hbar c \beta \gamma}{b}. \quad (3.4)$$

It is the energy above which the process becomes adiabatic while the Coulomb excitation process must be non-adiabatic. Since a range of the giant dipole resonance in heavy nuclei is around 20 MeV, with the obtained maximum excitation energy this range can be covered. The maximum excitation energy that can be transferred to a system in the electromagnetic process is connected to the virtual photon spectrum. Above a certain value of the excitation energy, the number of the photons quickly drops.

3.3 Weizsäcker-Wiliams formalism

The formalism developed by C.F. Weizsäcker and E.J. Wiliams in 1934 describes the Coulomb excitation process in terms of equivalent photon numbers. Here, Coulomb excitation is described as the absorption of virtual photons which are produced by relativistically moving charged particles. Figure 3.1 shows the case when an Argon projectile with a charge Z_1 is moving with a velocity ν towards a target nucleus with a charge Z_2 at an impact parameter b . The systems, Z_1 of the projectile and Z_2 of the target, are considered in the rest frame of the target. As presented in figure 3.1, the projectile trajectory is considered to be a straight line in the Z_2 system since at relativistic energies the scattering angle from the interaction is very small and can be neglected. The electromagnetic field of the lead target is seen by the relativistically moving projectile and the electric components of the fields in inverse kinematics can be described as [63]:

$$E_{\perp}(t) = \frac{Z_2 e \gamma b}{(b^2 + \gamma^2 \nu^2 t^2)^{3/2}}, \quad E_{\parallel}(t) = \frac{Z_2 e \gamma \nu t}{(b^2 + \gamma^2 \nu^2 t^2)^{3/2}}, \quad (3.5)$$

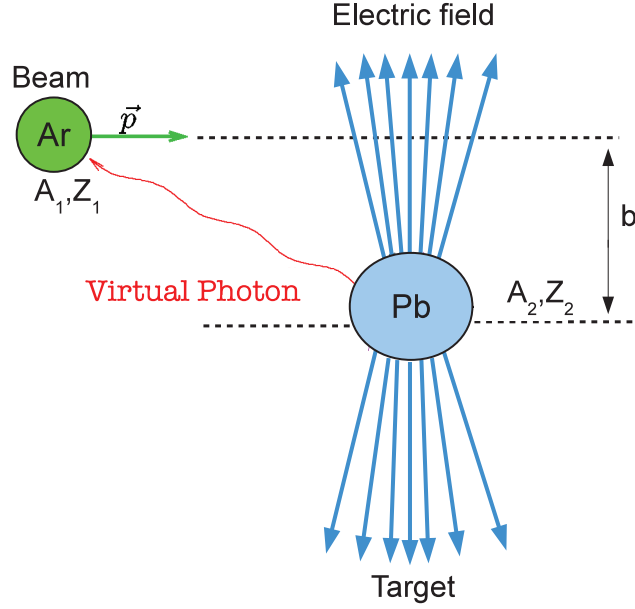


Figure 3.1: Coulomb excitation process between a projectile (Ar) and a target nucleus (Pb). The argon projectile impinges towards the lead target with an impact parameter b .

and the magnetic field components are written in the following way:

$$B_{\perp}(t) = \beta E_{\perp}(t), \quad B_{\parallel}(t) = 0. \quad (3.6)$$

Considering the fast relativistic beam, the interaction with the electromagnetic field is very short ($\Delta t = b/\gamma c \approx 10^{-23}$ s) and the transverse field components $E_{\perp}(t)$ and $B_{\perp}(t)$ are equivalent to a pulse (P) of plane-polarised radiation moving along the projectile's trajectory. The $E_{\parallel}(t)$ varies rapidly from positive to negative and has an integrated value of 0. The energy per unit area per unit frequency for the pulse P generated by the transverse component of the electric field is described via

$$\frac{dI}{d\omega}(\omega, b) = \frac{c}{2\pi} |E_{\perp}(\omega)|^2, \quad (3.7)$$

where $E_{\perp}(\omega)$ is the Fourier transform of $E_{\perp}(t)$ (time dependent electric field). As a result of the increased beam velocity, the higher frequencies in the radiation spectrum can be derived [65]. Evaluating the Fourier transformation $E(\omega)$ one can obtain:

$$\frac{dI}{d\omega}(\omega, b) = \frac{1}{\pi^2} \frac{(Z_2 e)^2}{c b^2} \left(\frac{c}{v}\right)^2 \cdot x^2 K_1^2(x), \quad (3.8)$$

where $K_1(x)$ is the first order of the modified Bessel function and $x = \omega b/\gamma v$. The energy per unit of frequency can be expressed without dependency on the impact parameter if one integrates over all possible values larger than b_{min} :

$$\frac{dI}{d\omega}(\omega) = 2\pi \int_{b_{min}}^{\infty} \frac{dI}{d\omega}(\omega, b) b db, \quad (3.9)$$

where b_{min} is the minimum impact parameter. The energy flux of the electromagnetic field in a frequency interval $(\omega, \omega + d\omega)$ can be calculated as a function of the number of the virtual quanta $N(\hbar\omega)$:

$$\frac{dI}{d\omega}(d\omega) = \hbar\omega N(\hbar\omega) d(\hbar\omega). \quad (3.10)$$

According to the virtual photon theory of Weizsäcker-Wiliams, the excitation of the target nucleus is described as the absorption of virtual photons whose spectrum is determined by the Fourier time-integral of the electromagnetic interaction. But, alternatively, one could also use the electromagnetic excitation (or Coulomb) cross section in order to obtain the virtual photon spectrum via the equation:

$$\sigma_C(E) = \int N(E) \sigma_\gamma(E) dE, \quad (3.11)$$

where $N(E)$ is the number of virtual photons which is computed by substituting equations 3.8 and 3.9 into 3.10. E is the energy carried by the photon $E = \hbar\omega$ and σ_γ is the photo-absorption cross section.

3.4 Semiclassical approach

In the classical Weizsäcker-Wiliams approach, the spectrum of virtual photons is independent of the multipolarity and for that another approach to calculate fields of all multipole components can be used. This approach was developed by C.A. Bertulani and V.Yu. Ponomarev [66] where the time-dependent electromagnetic field is described by using a Lienard-Wiechert potential [67, 68, 69, 70] which is expanded by a Taylor-series. Afterwards, the excitation amplitudes are calculated in first order perturbation theory depending on the potential as well as on the charge current density of the projectile. The Coulomb excitation cross section can be then derived from the square modules of the amplitude. Providing the derivation of the virtual photon numbers for different multiplicities, the total photo-absorption cross section then is the sum of all given multiplicities:

$$\sigma_C(E) = \int \left[\sum_{\pi\lambda} \frac{1}{E} N_{\pi\lambda}(E) \sigma_{\pi\lambda}^\gamma(E) \right] dE, \quad (3.12)$$

where $\sigma_{\pi\lambda}^\gamma$ is the photo-nuclear absorption cross section for a given multipolarity $\pi\lambda$ marked as the parity and angular momentum. The virtual photon number $N_{\pi\lambda}(E)$ is

independent of the nuclear structure coefficient. The virtual photon numbers for the three main multipolarities E1, E2 and M1 are given by

$$n_{E1}(E) = Z_2^2 \alpha \frac{2}{\pi} \left(\frac{c}{\nu}\right)_2 \left[\zeta K_0 K_1 - \frac{\nu_2 \zeta_2}{2c_2} (K_1^2 - K_0^2) \right], \quad (3.13)$$

$$n_{E2}(E) = Z_2^2 \alpha \frac{2}{\pi} \left(\frac{c}{\nu}\right)^4 \left[2\left(1 - \frac{\nu_2}{c_2}\right) K_1^2 + \zeta \left(2 - \frac{\nu_2}{c_2}\right)_2 K_0 K_1 + \frac{\zeta_2 \nu_4}{2 c_4} (K_0^2 - K_1^2) \right], \quad (3.14)$$

where α is the fine structure constant, $\zeta = Eb_{min}/\hbar\gamma\nu$ is the adiabaticity parameter corresponding to b_{min} , $K_0 = K_0(\zeta)$, $K_1 = K_1(\zeta)$:

$$n_{M1}(E) = Z_2^2 \alpha \frac{2}{\pi} \left[\zeta K_0 K_1 - \frac{\zeta_2}{2} (K_1^2 - K_0^2) \right]. \quad (3.15)$$

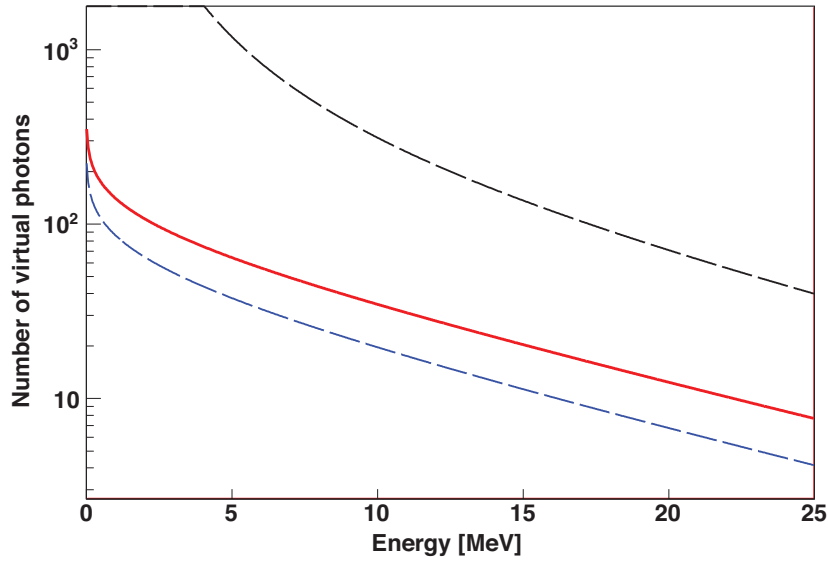


Figure 3.2: Virtual photon numbers for ^{32}Ar projectile impinging on a ^{208}Pb target with 650 AMeV as a function of photon energy for three multipolarities. The E1 (solid red line), M1 (dashed blue line) and E2 (dashed black line) virtual photon fields are represented.

Figure 3.2 shows a distribution of the three multipolarities of the virtual photon field in case when ^{32}Ar projectile incident on ^{208}Pb target with energy $E = 650$ AMeV.

3.5 Experimental approach

In the experiment carried out in this work a relativistic Ar beam impinges on a Pb target. It is important to identify the incoming heavy ions on an *event-by-event* basis

and identify the Coulomb dissociation reaction and reconstruct the excitation energy in each individual collision. The identification of the heavy ions before and after the reaction relies on the deflection in a magnetic field (B) using the relation for the magnetic rigidity $B\rho$:

$$B\rho \propto \frac{A}{Z}\beta\gamma. \quad (3.16)$$

In the reaction the incoming heavy ion is Coulomb excited. Immediately after the excitation the heavy ion may emit light particles and/or gamma radiation. The latter is detected by gamma-ray detectors surrounding the target. The forward going remaining heavy fragment is tracked through a (homogeneous) magnetic field to determine the magnetic rigidity using several sets of position sensitive detectors. The nuclear charge of the heavy fragment is determined by measuring the energy loss and its velocity is determined through a time-of-flight measurement.

Emitted light charged particles, like protons, are also going forward and are tracked through the magnetic field and their energy and momentum are determined.

The tracking of the charged particles enables momentum reconstruction and together with the detection of their energies as well as the total energy emitted via gamma radiation enable the reconstruction of the excitation energy of the Coulomb excited projectile via the concept of invariant mass. The methodology for the momentum reconstruction and the determination of the invariant mass are further described hereafter.

3.5.1 Momentum reconstruction

After all reaction products are identified and for each of them their trajectory before and after the magnet determined using the time of flight and the coordinates of the hits in the detectors, the four-momenta can be reconstructed in the following way ($\hbar = c = 1$):

$$\hat{P} = (E, \vec{p}). \quad (3.17)$$

By measuring polar and azimuthal angles θ and ϕ relative to the primary beam direction, the momentum components p_x , p_y and p_z can be determined:

$$\left\{ \begin{array}{l} p_x = p_0 \sin \theta \cos \phi \\ p_y = p_0 \sin \theta \sin \phi \\ p_z = p_0 \cos \theta \end{array} \right\}. \quad (3.18)$$

The total momentum in the laboratory frame can be calculated as

$$p_0 = m_0\beta\gamma, \quad (3.19)$$

where m_0 is the rest mass of the fragment, β is calculated by exploiting the time of flight and $\gamma = \sqrt{1/1 - \beta^2}$ is the Lorentz factor.

3.5.2 Invariant mass

The measurement of the excitation energy distribution E^* of exotic nuclei and determining the energy dependent differential cross section are the crucial parts in an electromagnetic excitation experiment. The current experiment has been performed in inverse kinematics at relativistic beam energies and as a consequence the direct measurement of the excitation energy of the reaction partners is impossible. The excitation energy provides information on the electromagnetic modes of the different reactions channels. It allows further studies of cross section components. The only way to reconstruct the excitation energy transferred to the projectile by a virtual photon is to identify all components of the reaction (incoming and outgoing particles) and to calculate the invariant mass on an *event-by-event* basis.

The invariant mass of an object (M^{inv}) is a relativistically invariant quantity and it is defined as a square of the four-momentum \hat{P} (see previous section 3.5.1) [36]. In the rest frame of a given object, e.g. a nucleus in its ground state, the invariant mass is equal to its relativistic rest mass. The invariant mass of the excited projectile (M_{proj}^{inv}), due to the relativistic energy-mass equivalence, is equal to a sum of the rest frame mass (m_{proj}) and the excitation energy (E^*):

$$M_{proj}^{inv} = m_{proj} + E^*. \quad (3.20)$$

The conservation of the invariant mass implies that after the excited nucleus transforms into a number of particles, the square of the sum of their four-momenta is still equal to the square of the invariant mass defined in equation 3.20. Therefore it can be written as following:

$$M_{proj}^{inv} = \sqrt{\left\{ \begin{array}{c} \sum_i E_i \\ \sum_i \vec{p}_i \end{array} \right\}^2}, \quad (3.21)$$

where the sums run over all i outgoing decay products with their $\hat{P}_i = (E_i, \vec{p}_i)$.

The energy and momentum for equation 3.21 can be expressed using masses and velocities where in the first step the energy of the emitted photons can be neglected:

$$\left(\sum_i E_i\right)^2 = \sum_i (\gamma_i m_i)^2 + \sum_{i \neq j} \gamma_i \gamma_j m_i m_j, \quad (3.22)$$

$$\left(\sum_i \vec{p}_i\right)^2 = \sum_i (\gamma_i \beta_i m_i)^2 + \sum_{i \neq j} \gamma_i \gamma_j \beta_i \beta_j m_i m_j \cos \theta_{ij}, \quad (3.23)$$

where i and j are the different particles involved in the analysis (incoming and outgoing), their masses (m), velocity (β), Lorentz factor (γ), relative angles between reaction products (θ) of all outgoing particles and γ -ray energy E_γ . Using $\gamma^2(1 - \beta^2) = 1$, equations 3.22, 3.23 are introduced into equation 3.21 where the gamma energy can be added resulting in the following expression:

$$M_{proj}^{inv} = \sqrt{\sum_i m_i^2 + \sum_{i \neq j} m_i m_j \gamma_i \gamma_j (1 - \beta_i \beta_j \cos \theta_{ij})} + E_\gamma. \quad (3.24)$$

By combining equations 3.20 and 3.24, the reconstruction of the excitation energy can be written as:

$$E^* = \sqrt{\sum_i m_i^2 + \sum_{i \neq j} m_i m_j \gamma_i \gamma_j (1 - \beta_i \beta_j \cos \theta_{ij})} + E_\gamma - m_{proj}. \quad (3.25)$$

This equation requires the identification of all particles and tracking of all outgoing particles. How this is carried out in the experiment is described in the next chapters.

Chapter 4

Experimental Facility and R3B/LAND Setup

The possibility to perform high-quality experiments is given at the GSI facility, utilizing the most recent achievements in production, acceleration, cooling and storing of heavy highly- charged ions at the SchwerIonen Synchrotron (SIS) and Experimental Storage and cooler Ring ESR (see Fig.4.1). One of the most important tools for such experiments is the FRagment Separator, where relativistic beams of exotic nuclei can be produced and separated. These secondary ions are transported further to the R3B/LAND experimental installations. In this chapter this procedures will be described in more detail. Also the description of the R3B/LAND experimental setup is given and all detectors are individually described according to their function.

4.1 Beam transportation

The GSI accelerator facility (see fig.4.1) consists of the UNIversal Linear ACcelerator (UNILAC), where low-charged ions can be accelerated up to an energy of 11.4 AMeV [43]. For acceleration to higher energies the ions are injected into a transfer line to the heavy ion synchrotron. In the transfer line the ions pass through stripper foils. The thickness and the material of the stripper foil is chosen in an optimal way so that the yield of the desired charge-state is maximal. From the emerging charge state distributions, the fraction of the ions with the desired charge state is magnetically separated and directed towards the heavy-ion synchrotron SIS18. In the SIS18, the ions are subject to a further acceleration up to the desired energy. A maximum magnetic rigidity of the ring is 18 Tm which corresponds to energies of 1-4.5 AGeV [44]. This accelerator complex allows to accelerate all stable ions from hydrogen to uranium, delivering high quality stable beams, which can be used for in flight production of secondary radioactive beams by hitting a thick production target at the exit of the SIS18. For the experiment discussed here two different primary beams had been used. Stable ^{40}Ar beam of energy 500 AMeV was produced using natural gas of ^{40}Ar and was used to performed the settings and the calibration procedure. An ^{36}Ar beam of energy

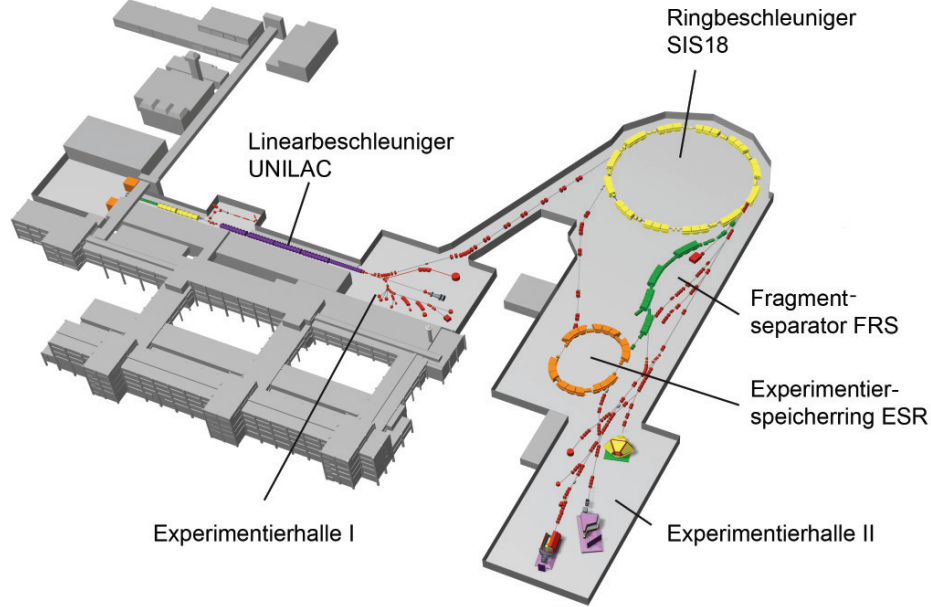


Figure 4.1: Layout of the accelerator facility at GSI, showing the linear accelerator UNILAC, the heavy-ion synchrotron SIS, the Experimental Storage Ring ESR and the FRagment Separator FRS.

825 AMeV, used as a main production beam during the experiment, was produced from enriched Argon gas. The maximum intensity of ions in the SIS18 was around 3×10^{10} particles per spill. Fragmentation of the primary beam on the production target results in a secondary beam which contains a large number of different nuclides which were selected and identified on an *event-by-event* basis. For this purpose the beam pass through the Fragment Separator described in the following section.

4.2 The Fragment Separator FRS

The FRagment Separator is an achromatic magnetic forward spectrometer located at the exit of the heavy-ion synchrotron SIS18 [43, 51, 46]. The high energy primary beam interacts with a 6.347 g/cm^2 beryllium production target at the FRS to produce the different secondary exotic isotopes via nuclear fragmentation. Reaction products are separated by means of the $B\rho - \Delta E - B\rho$ method in the FRagment Separator using four different stages, each consisting of a 30° dipole magnets and a system of quadrupoles placed before and after the dipole. The ions, passing through the first stage of the FRS, (see figure 4.2) are analyzed according to their magnetic rigidity $B\rho$:

$$B\rho = \frac{p}{Q} \propto \frac{A}{Z}\beta\gamma, \quad (4.1)$$

where B is the strength of the magnetic field adjusted for a given ion and ρ is the bending radius of the trajectory in the FRS bending magnets. p and Q are momentum and charge respectively of the particles passing through the magnet. A and Z are the mass and charge numbers, β is its velocity ($\beta = v/c$) and $\gamma = \sqrt{1/1 - \beta^2}$ is the Lorentz factor. Since the energy loss of the ions passing through matter depends on Z , it gives a possibility to separate different ions by passing them through a solid degrader in the middle of the FRS.

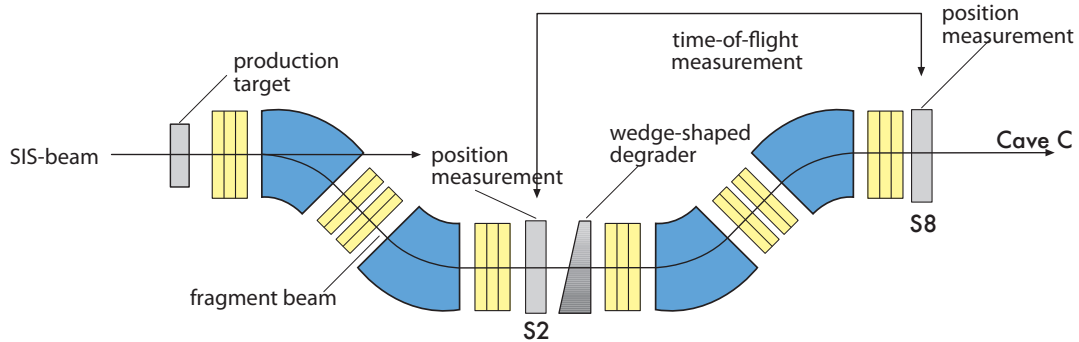


Figure 4.2: Schematic of the FRS setup with the primary target area. The secondary ions produced after the interaction fragmented incoming beam coming from SIS with the target placed at the entrance of FRS are selected and identified by the FRagment Separator before coming to the Experimental Hall in the Cave C [11].

The time of flight, energy loss and horizontal position of the ions are measured using a detection system located in the FRS such as scintillator detectors S2 and S8 as one can see from figure 4.2. The simulation for the settings of the FRagment Separator and the optimization for the beam production was done with a MOCADI simulation [34]. The program calculates the transport of particles through the ion optical systems of magnets and layers of degraders. For each isotope simulations with different degrader thicknesses were done in order to choose the one which gives the best values for the intensity of the primary fragment and the contamination from other isotopes in the secondary beam. The measured values for the transmission efficiency were 95% for $S2 \rightarrow S8$ and 36% for $S8 \rightarrow \text{Cave C}$.

4.3 Experimental Setup

As discussed in section 3.5, in order to determine the Coulomb excitation energy on the Pb target and investigate the pygmy and giant dipole resonances, one has to identify all reaction components and measure their momenta. The main purpose of the detector system is to identify all components of the reaction allowing reconstruction of the momenta with high resolution. The reconstruction of the excitation energy can be done using the invariant mass technique in an event-by-event mode.

The secondary ions selected and identified by the FRS, were transferred to the experimental hall with R3B/LAND setup, presented in figure 4.3. The beam was sent to different secondary targets (placed in the Crystal Ball which is used to detect the emitted photons) to separate Coulomb excitation from inelastic scattering. Different isotopes after the secondary reaction target are deflected to different angles by the ALADIN dipole magnet, and registered in a detection system placed after the ALADIN magnet. For the neutron deficient nuclei under investigation the de-excitation is dominated by proton emission and those are tracked by Si-strip detectors before the ALADIN magnet and by the drift chambers (PDC1/PDC2) and the big TOF Wall (TFW) after the magnet. Heavy fragments as well as protons from the decay are also tracked through the ALADIN dipole field. The time of flight of the fragments and their energy loss was measured with a plastic scintillating detectors (NTF), placed behind the fiber detectors (GFI1/GFI2) that are used for the horizontal position recording. The different detector components are discussed in details in the following sections 4.5-4.7.

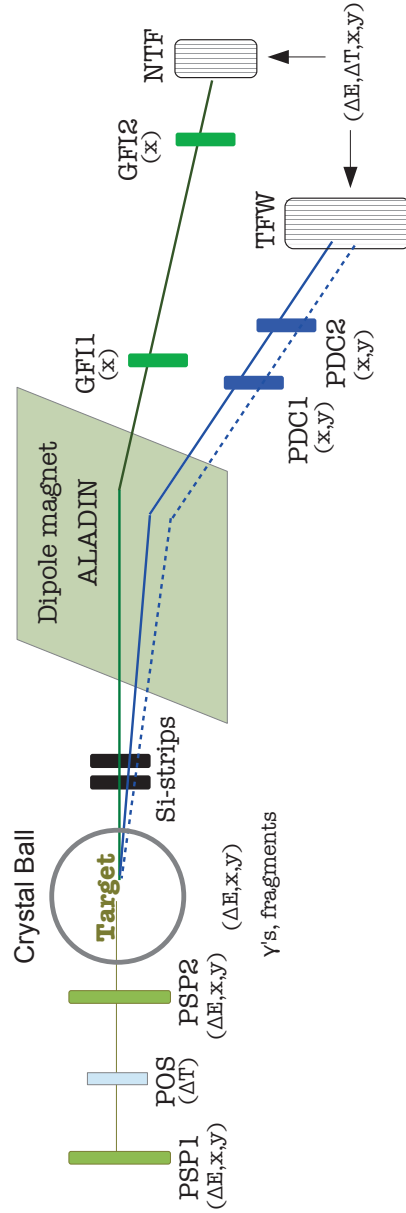


Figure 4.3: Schematic view of the R3B/LAND experimental setup in Cave C. The setup provides full kinematics measurements. Selected secondary beams are sent to the secondary Pb target, placed in the center of the Crystal Ball. The heavy reaction fragments are deflected to the different angles by the ALADIN dipole magnet and further detected by fibre detectors (GFI), placed after the magnet and a small ToF Wall (NTF). Protons are detected by drift chambers (PDC1, PDC2), Si-strip detectors and Big ToF Wall (TFW), while γ rays are detected by the Crystal Ball array.

4.4 Data acquisition system

The Data Acquisition system (DAQ) is used as a general term for the hard- and software for control, conversion and storage of the registered data. The data collection within the present experiment is performed on an event by event basis using the GSI internal development called the Multiple Branch System (MBS). The DAQ is adjusted before each experiment for the most effective and possibly lossless data collection. However the data conversion takes some time during which no other event can be recorded, the so called dead time. Once an event occurs in the setup, it produces a raw analog signal which has to be digitized and collected by the DAQ system. To allow a recording of a good event in the detectors a trigger decision has to be involved. The trigger decision is produced by checking the coincidence between the logical signals from different detectors. In case the trigger is accepted, gate and start/stop signals are generated for the QDCs/TDCs, and the signal conversion is performed. The DAQ system and the trigger logic together have to be able to identify, select (using the trigger information and their downscale) and store the good events into the data files. These files are then further used for the analysis.

4.4.1 Signal preparation

Most of the detectors of the R3B/LAND setup are scintillators which are read out by photomultipliers. Delivered signals need an additional amplification or/and shaping (time signal of the Crystal Ball). Otherwise the procedure described here is much the same for all detectors in the setup. Each detector delivers the pre-amplified analog electrical signal which is later split in order to have energy and time information. An overview of the electronics is presented in figure 4.4 for one typical detector channel with the time and energy readout modules. The analog energy signal is directed to Charge-to-Digital Converter (QDC) after being delayed by a passive delays (typically about 500 ns).

The time signal is first sent to the constant fraction discriminator (CFD). In order to distinguish from the noise, the signal needs to pass the threshold of the CFD. After the discriminator produces a logic signal which is split into two: one directed to the Time-to-Digital Converter (TDC) being again delayed in order to wait for the trigger to be accepted. The second one is sent to the module that creates a trigger. The time in the TDC is measured between a common start/stop signal generated by the trigger logic system and the individual logical signal from the CFD.

4.4.2 Trigger construction

Creating a detector trigger proceeds in several steps. From each individual channel of the detector the logical signals are combined [57]. The detector triggers are combined into a coincidence and anti-coincidence patterns, creating so called physics triggers for good beam or fragments. The trigger generation is based on coincidences and multiplicity, i.e. a certain number of channels is required to have produced signals

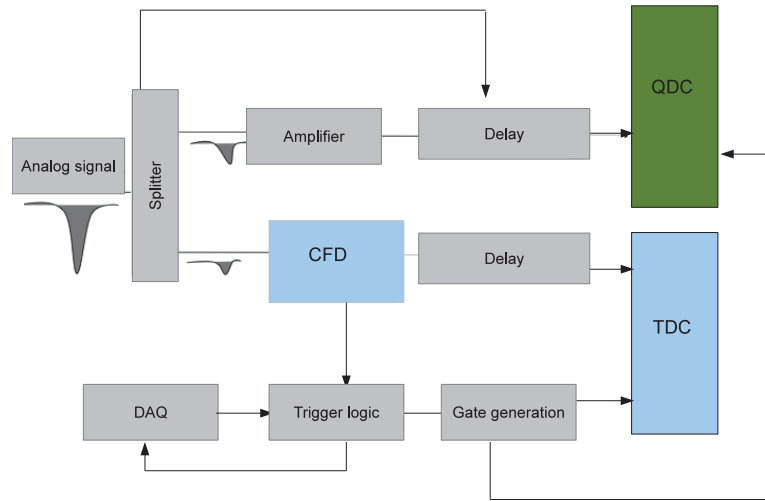


Figure 4.4: Schematic of the electronics with the time- and energy- readout modules.

in coincidence. For example, for the Crystal Ball trigger (CB OR) it is sufficient to have a signal in any of the crystals while for the POS detector, all four channels have to produce a signal in order to have a POS detector trigger. The triggers used (and their main purpose) in experiment S327, generated by combining the logic signals, are described in tables 4.1 and 4.2. There are two groups of physics triggers, on-spill and off-spill. During the time interval in which the beam is extracted from the synchrotron and expected in Cave C, the on-spill trigger appears. Off-spill triggers can only occur between beam spills and are used only for the calibration procedure and background subtraction. During that time, the data acquisition is running and collecting events for the detector calibration. In case there is no physics events, there are still events to be detected - the calibration triggers like "clock" and "tcal" are continually generated by designated modules.

More information on hardware and software aspects of data acquisition can be found in [58, 59].

4.5 Detectors before the Target

4.5.1 S2 and S8 detectors

The detectors placed at the S2 and S8 focal planes of the FRS (see figure 4.2) are scintillators which consist of a rectangular plastic material with dimensions of $218.6 \times 80 \times 1 \text{ mm}^3$ and $200 \times 80 \times 1 \text{ mm}^3$ respectively. The detectors placed in the beam line and read out by two photomultipliers from both sides delivering time and energy loss simultaneously. During the experiment, the S2 detector was not working properly because of the high intensity in the middle focal plane of the FRS. Therefore, the data from this detector are not used for the analysis and the time of flight measurement between S2 and S8 detectors is missing. Nevertheless, it was sufficient to use only one scintillating detector

Table 4.1: The summarized physics triggers and corresponding coincident logical signals used in the S327 experiment. The "•" symbol means AND condition while the "◦" corresponds a NOT-AND.

Tpat	Trigger name	TFW cosm	NTF cosm	CB sum	FRS S8	CB dlyOR	CB dlySum	Pixel	pileup	Spill on	TFW mult.	NTF mult.	LAND mult.	CB OR	Veto Wall	LAND cosm	POS!ROLU
1	Good Beam									•							•
2	Fragment								◦	•		•					•
4	CB OR								◦	•		•		•			•
8	CB Sum			•					◦	•		•					•
16	Proton								◦	•	•	•					•
32	Good Beam-PileUp								◦	•							•
64	Pixel							•		•							•
128	Neutron								◦	•		•	•				•
256	CB muon						•		◦								◦
512	LAND cosmic								◦							•	◦
1024	TFW cosmic	•							◦								◦
2048	CB gamma					•			◦								◦
4096	Clock																
8192	TCAL																
-	Spill on																
-	Spill off																

at S8 as a final detector of the FRS. The measurements of the time of flight between the S8 detector and POS in Cave C was performed in order to identify ingredients of the beam.

4.5.2 POS detector

For the timing purpose the POS detector placed before the secondary Pb target was used. The detector is a 2.5×2.5 cm² plastic scintillator with thickness of 200 μ m and it is connected to four fast photomultipliers (see Fig. 4.5) from each side.

4.5.3 PSP detectors (PSP1/PSP2)

The PSP is a Position Sensitive silicon Pin diode with an active area of 4.5×4.5 cm². The detector consists of 5 channels: four anodes on the resistive front side and one cathode on the back (see Fig. 4.6). The four independent signals from the anode (Q_1 , Q_2 , Q_3 , Q_4) at the corners allow to reconstruct the position of the hit of the ion passing

Table 4.2: The requirements (and main purposes) in order to create the certain logical signal.

Good Beam	The POS detector with anti-coincidence of the ROLU. (Any incoming ion arriving in the Cave C.)
Fragment	The heavy fragment detector NTF. (For the fragments reconstruction.)
CB OR	Any crystal of the Crystal Ball detector fired. (For the calibration with γ source), spill off.
CB Sum	The analog sum from all crystals in the Crystal Ball above a certain threshold.
Clock	(For determining the QDC pedestals), spill off.
TCAL	(For the TDC gain calibration), spill off
Spill on	The accelerator for begin/end of spill
Pixel	The active pixel mask (For the PSP calibration)
TFW cosmic	cosmic particles in Big Time of Flight Wall. (For the calibration of the TFW detector), spill off.
LAND cosmic	high multiplicity in LAND detector. (For the LAND calibration), spill off.
Proton	Big Time of Flight Wall (TFW). (proton reconstruction)
CB gamma	gamma candidates
FRS(S8)	For counts particles arrived to S8 for online monitoring and transmission to the Cave C

through the detector. The signal from the cathode corresponds to the total energy loss from which the charge Z can be determined. The achieved energy resolution is about 1% for a typical energy loss of 50 MeV in the detectors. Assuming that the collected charge fraction is proportional to the distance between an incident position and the electrode, the position in x and y direction can be reconstructed via the relations

$$x = \frac{(Q_2 + Q_3) - (Q_4 + Q_1)}{Q_1 + Q_2 + Q_3 + Q_4}; \quad y = \frac{(Q_1 + Q_2) - (Q_3 + Q_4)}{Q_1 + Q_2 + Q_3 + Q_4}. \quad (4.2)$$

Both detectors PSP1 and PSP2 are placed upstream of the target and are involved in the analysis to extract the energy loss information for the incoming beam and for the reconstruction of the position of the beam on target.

4.5.4 Veto detector

The Veto detector is located between the PSP2 and the target and consists of four movable scintillators with dimensions of $95 \times 100 \times 5$ mm³. Two scintillators placed vertically and the other two horizontally. The role of the veto detector is to veto

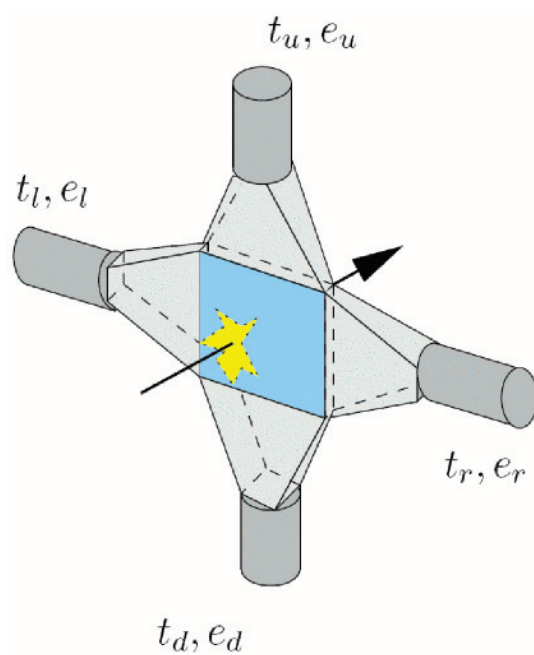


Figure 4.5: The POS detector which is mainly used for timing purposes.

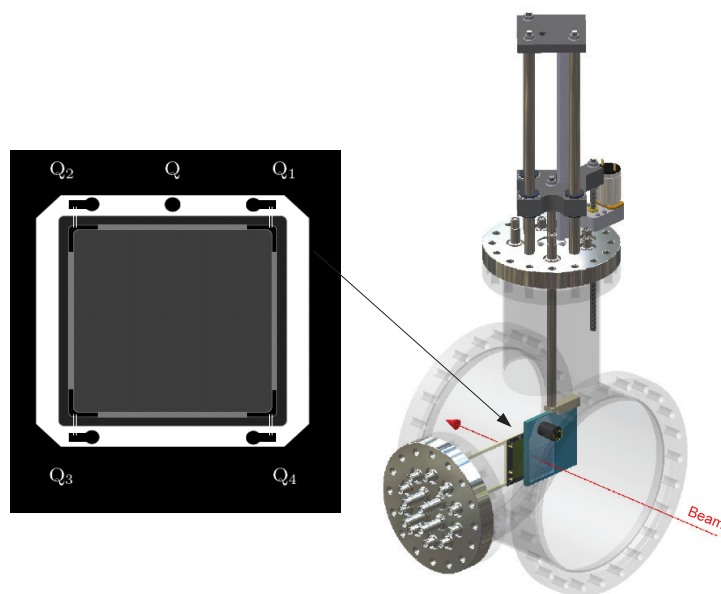


Figure 4.6: The Position sensitive PIN diode is readout by four anodes Q_1 , Q_2 , Q_3 , Q_4 and by a cathode Q from the back side of the detector.

those ions that are too far away from the center of the beam line. It is called ROLU

(from Rechts Oben Links Unten). Since the plates are movable, it allows to open and close a rectangular window in the center of the detector in x-direction and y-direction respectively. Only particles passing through this window are accepted and detected further.

4.6 Detectors after the Target

4.6.1 Scintillating GFI1/GFI2 detectors

The GFI scintillating fibre detectors are used to reconstruct the trajectory of the heavy fragments from the secondary reactions. The detectors are placed after the large-acceptance dipole ALADIN magnet. The active area of the detector consists of nearly 500 parallel thin and long [37] scintillating fibres, covering an area of $50 \times 50 \text{ cm}^2$. As indicated in the schematic view (see Fig. 4.7), the scintillator fibres are placed very close and parallel to each other. Each fibre is 1 mm thick with a square cross section [38] and is painted white in order to maximize light propagation and to avoid cross talk between neighboring fibers. Instead of reading out each individual fibre separately, the end of each fibre is glued and connected to a Position-Sensitive photocathode PM (PSPM), using a specially designed mask, in such a way that each fibre has distinct (u, v) coordinates on the plane of the mask (see Fig. 4.7). The PSPM is a $64 \times 58 \text{ mm}^2$ rectangular photocathode, consisting of a 16 mesh-type dynode and a multi-wire anode with 18 wires in the v direction and 16 in the u direction. Due to the special structure of the anode grid, the charge distribution is correlated with the position of the light spot on the photocathode. The other end of the fibres is read out using the photomultiplier for the good timing information and triggering [39].

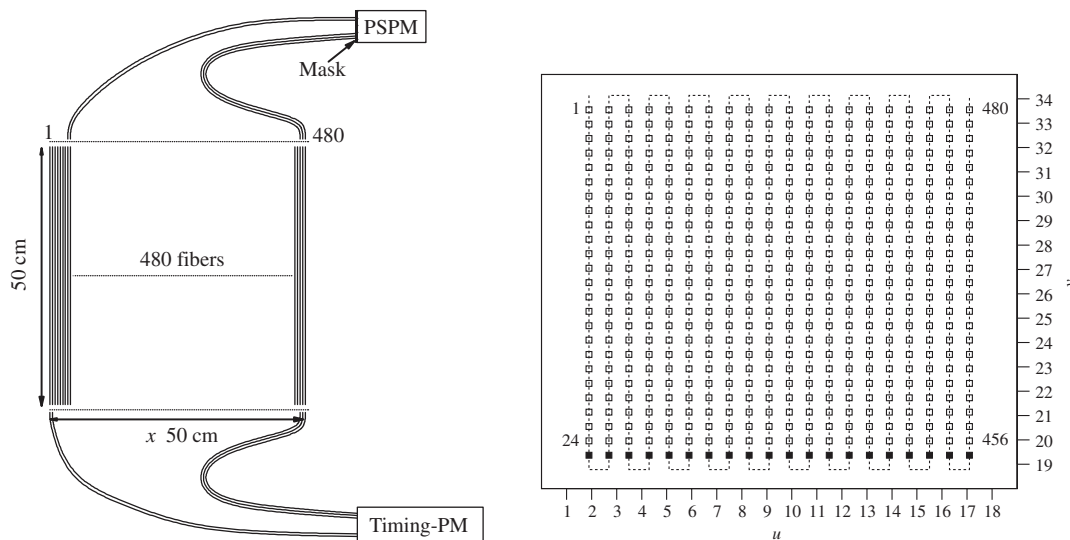


Figure 4.7: Schematic of the scintillating fiber detector (left) and the mask (right) to guide the fibres on the PSPM cathode [55].

4.6.2 New ToF Wall (NTF)

The reconstruction of the time of flight between POS detector and the last detector in the detection system for the heavy reaction products is performed with the New ToF Wall. The energy-loss information of the heavy ions can be obtained as well. The NTF is a fast-moving-ion detector made with plastic scintillator material and modern photomultiplier tubes (see Fig. 4.8). It is constructed of 16 paddles of plastic scintillator of 60 mm width, 480 mm length and 5 mm thick. The paddles are arranged in two layers with 8 vertical and 8 horizontal paddles. Each paddle is an independent unit read out at both ends by means of fast photomultipliers. The time of flight can be calculated as a mean from two paddles that delivered signals after being hit by a reaction product. The position within a paddle can be derived from a time difference between the two ends of the paddle and the charge of a particle is extracted from the energy loss in the scintillating material.

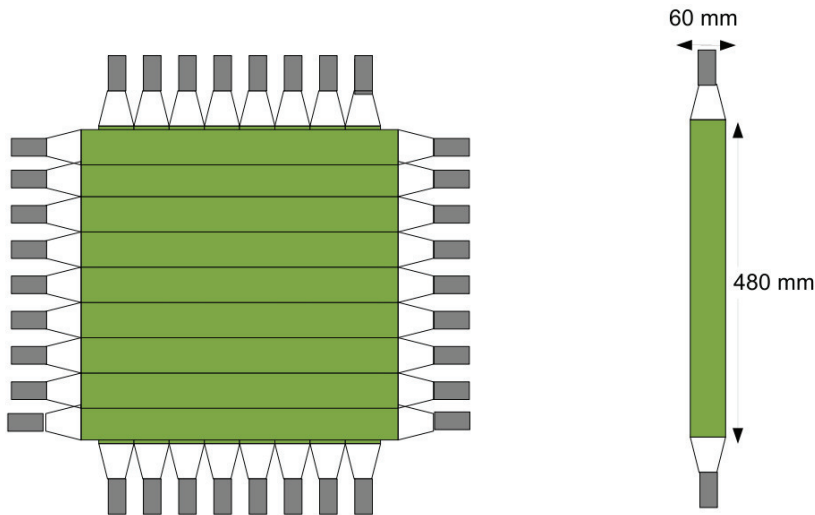


Figure 4.8: Schematic of the New ToF Wall used for the detection of the heavy reaction products.

4.6.3 Proton Drift Chambers (PDC1/PDC2)

The Proton Drift Chambers are gas-detectors providing an accurate measurement of the hit position of a charged particle, mainly protons. The protons from the reaction are deflected by the ALADIN magnet and tracked through the two drift chambers. The active area of the drift chambers is $100 \times 80 \text{ cm}^2$ each with two separate layers,

one for detection of the x-position, the other for detection of the y-position. There are 256 read-out channels, 144 vertical x-wires and 112 horizontal y-wires. The signal from each wire is digitized by the electronics which converts the voltage on the wires every 2.5 ns into a digital value. The parameters which characterize the drift chamber depend on the gas mixture with which they are filled which contains 80% argon and 20% methane.

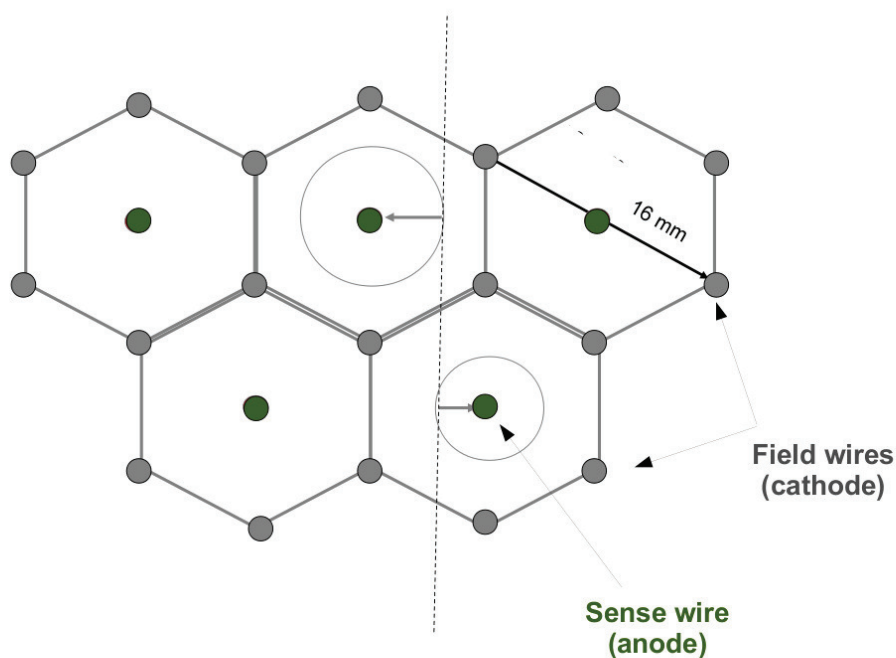


Figure 4.9: The schematic of one layer of the drift chamber and procedure of the electrical signal reordering. The sense wire anodes surrounded by cathode wires (field wires) forming a hexagonal structure. The inter-wire distance of 0.7 cm.

The protons which pass through the detectors ionize the gas and in the high-field region near the wires avalanches are induced, which provide the charge amplification at the read-out wires. Electrical signals that contain information about the original location and ionization density of the segment are recorded. There is a sense wire in the center of each cell (figure 4.9) which is surrounded by 6 field wires. Each individual drift cell has a diameter of 16 mm. The sense wires are built of 25 μm diameter gold-plated tungsten while the field wires consist of 75 μm diameter copper-beryllium.

4.6.4 Big ToF Wall (TFW)

For the time of flight measurements and deriving the energy loss information of the light reaction products the big Time of Flight Wall is used. The TFW detector contains two planes of scintillating paddles placed perpendicular to the beam direction. One plane consist of 18 horizontal paddles and the second with 14 vertical paddles, as presented in Fig. 4.10. The size of the vertical paddles is $147 \times 10 \times 0.5 \text{ cm}^3$ and that of the horizontal one is $189 \times 10 \times 0.5 \text{ cm}^3$. The expected time resolution of the detector is $\sigma = 100 \text{ ps}$. Both sides of the paddles are read out by two fast PMTs from which the energy loss and time can be delivered. By measuring the arrival time of the scintillation light from both photomultipliers, the position of the particles can be derived. The scintillation light should arrive at the same time at both photomultipliers of one paddle when the hit is in the middle. The position information is very important for the calibration procedure which has to be done first before any physical data can be used from the detector. The calibration procedure is described in chapter 5.

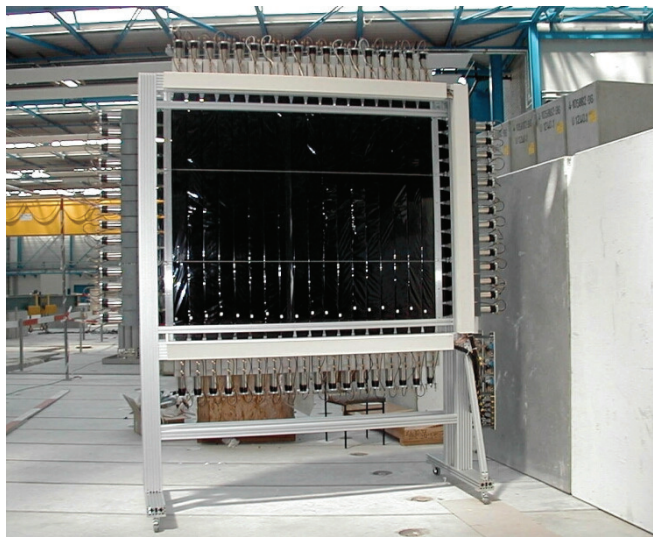


Figure 4.10: The big Time of Flight Wall for the detection of light particles, e.g. protons.

4.7 Detectors around the Target

4.7.1 Crystal Ball (XB)

In order to detect the instantaneously emitted γ rays from the reaction the Crystal Ball spectrometer, built in spherical 4π geometry, was used (see Fig. 4.11) [42]. It consists of 162 NaI crystals. A sphere of inner radius of 25 cm, thickness 20 cm and with four different shapes of crystals: regular hexagon (12 crystals) and irregular pentagons (60+60+30 crystals). Some important parameters and resolutions of the Crystal Ball are given in table 4.3. The time and energy is read out by PM photomultipliers

connected to each individual crystal. Using the sum energy measurements, the total excitation energy of the excited state in the emitting nucleus can be reconstructed. The high granularity of the detector allows for a correction of the Doppler shift of the γ rays emitted in-flight.

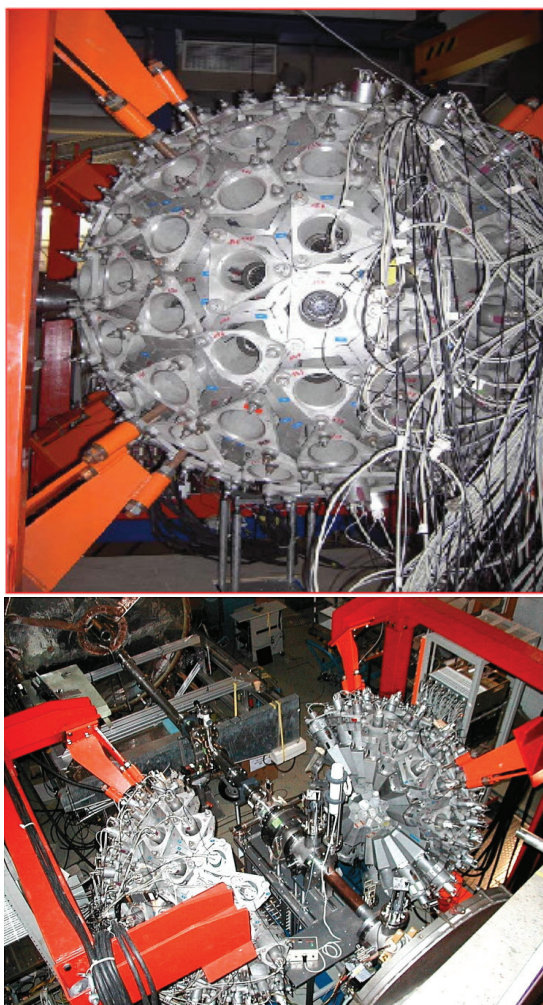


Figure 4.11: Crystal Ball γ -ray detector. The picture show a view of opened (bottom) and closed detector (top).

Any of the crystals can be easily dismantled making place for a beam-line while the target is mounted on the "target wheel", which is also movable. It gives a possibility to use different targets during the experiment without a vacuum interruption. In the described experiment several targets were used (see table 4.4) in order to induce the electromagnetic excitation and nuclear contributions. In order to clean up the useful physical data from reactions in materials outside the target, a measurement without a target was carried out as well.

Table 4.3: Crystal Ball parameters and resolutions.

E_γ	Total efficiency[%]
1.3 MeV	96
3.0 MeV	90
Energy resolution of single crystal[%]	
662 keV	7.8
1.3 MeV	5.5

Table 4.4: Targets used during the experiment.

Target	Density[g/cm ²]	Reaction Type
²⁰⁸ Pb	0.515	Electromagnetic excitation
¹² C	0.37	Nuclear contribution
empty target	-	Background contribution

4.7.2 Silicon STrip detectors (SST1/SST2)

Two Silicon-STrip detectors placed in the beam line directly behind the target are used to track and reconstruct the position of heavy ions and protons produced in high-energy reactions. The detector design is based on double-sided Si microstrip detectors (DSSD) and developed by the Alpha MAGnetic Spectrometer (AMS) collaboration especially to provide a large dynamic range. In order to detect simultaneously protons and the residual heavy nuclei it is necessary to have both low-noise and wide-range integrated-circuit amplifiers.

Each Si sensor (grey part in figure 4.12) has a size of 72×40 mm, and is 0.3 mm thick. The sensor has an implantation pitch on the junction side perpendicular to the long edge, called S-side, with 640 read-out strips. The corresponding size of the read-out pitch is 110 μm . Every fourth strip is connected to a read-out channel, while the others are left floating. The ohmic K-side of the sensor consists of 384 read-out strips and the implantation pitch is 104 μm with every strip being read out. Overall 640 strips are read out on the S-side and 384 on the K-side, resulting in a total of 1024 channels per sensor [47, 48, 49]. Ions passing through the SST create e-h-pairs in the vicinity of their tracks, usually firing a group of neighboring strips on S-side and K-side, respectively, creating a so-called cluster. More detailed information can be found in following articles [47, 49, 50].

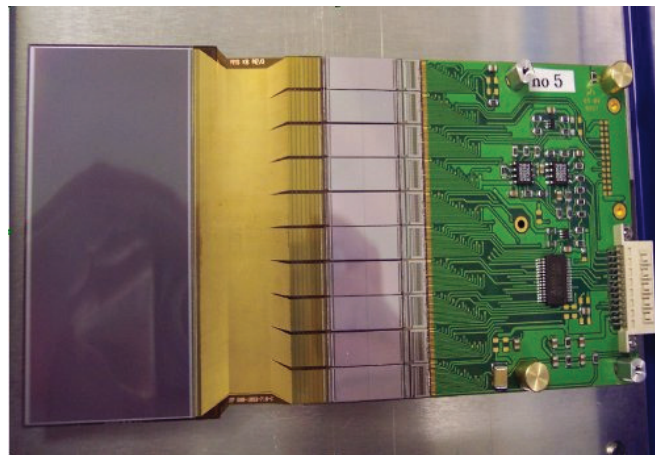


Figure 4.12: A single Silicon STRip detector with its front-end-electronics board (green part). Total 1024 strips are grouped in 10 visible and 6 (rear side) blocks of 64 read-out lines each, which strips are capacitively connected to 10+6 VA chips with pre-processing on the front-end board. The active area is rectangular with $4 \times 7 \text{ cm}^2$ with 640 vertical and 384 horizontal strips. The detector is used for the reconstruction of the position.

Chapter 5

Calibration

5.1 Calibration within the *land02* package

The main purpose of the detector system is to enable a way to reconstruct the four-momenta of the reaction products with high resolution. In order to reach the desired resolution and to derive any physics quantities, all detectors have to be calibrated and synchronized. The *land02* software package [58] is used to analyze the data from the experiment and contains the calibration and reconstruction routines for the experimental LAND setup. The four-momentum vectors can be reconstructed if the position of each individual detector is known, and the time of flight together with the particle hit position are measured. After the calibration parameters are set into *land02* package in text formats, the data can be unpacked from the binary data files to the special format used in the analysis. For this purpose a data unpacker has been used. The data reconstruction is performed step by step using the following unpack levels provided by the *land02*: RAW, TCAL, SYNC, DHIT, HIT and TRACK as shown schematically in figure 5.1:

RAW Level

The data stored directly by the DAQ is available in the RAW level. The data is not yet calibrated and all values are given in channels number. Using the data from the RAW level, one can easily check the status of all detectors.

TCAL Level

In the TCAL level time information is converted from TDC channel to nanoseconds. The QDC pedestal value from the measured energy values are subtracted. The necessary calibration parameters are calculated using the *clock* and *tcal* programs implemented within *land02* framework.

SYNC Level

The time and energy of the individual detectors are synchronized with respect to each other.

DHIT Level

DHIT level stands for detector-hit level. The time and energy information from the SYNC level are combined according to the setup geometry. This provides the position, mean time and energy loss of a hit in detector-internal coordinates. In detectors such as the NTF or TFW, hit position, time and energy are given for each paddle.

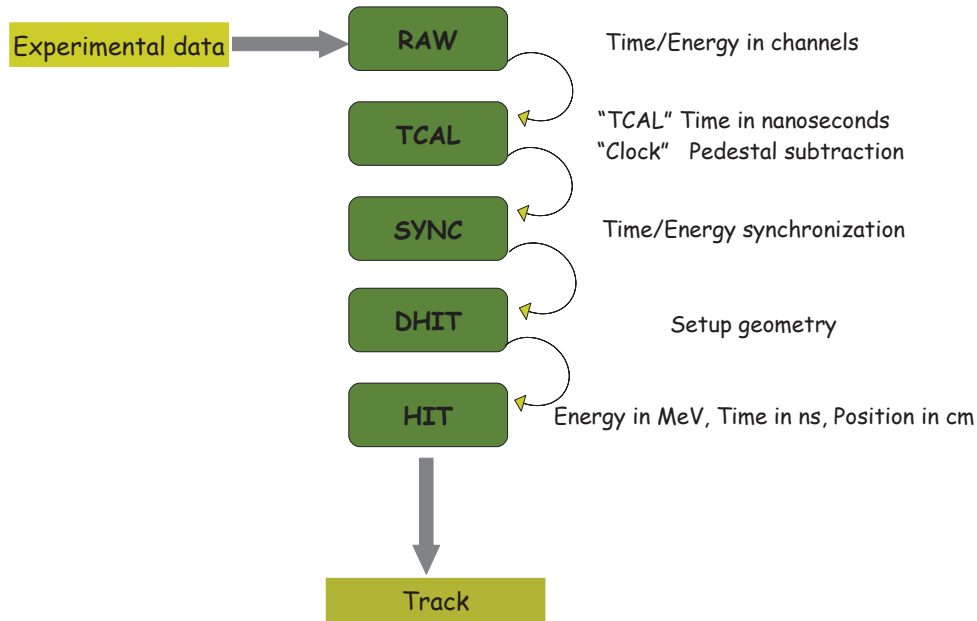


Figure 5.1: Schematic structure of the *land02* framework. Calibration levels are shown inside boxes with a short description of each steps.

HIT Level

All detectors are calibrated and treated as a whole unit by having only one energy and one time per hit. The time, energy and position of each hit are presented in units ns, MeV and cm.

TRACK Level

The information from each detector is combined with the others in order to express the physical data. The reconstruction for the incoming beam is implemented allowing to derive the identification information, such as β , Z , A/Z , T_0 .

5.2 Internal calibration of the scintillator paddles

In the LAND/R3B setup detectors which consist of plastic scintillator material can be split into two types of detectors. One type is consisting of a single scintillating unit, like POS and S8 detectors and the other type contains paddles which are readout from both sides by photomultiplier tubes. The big Time of Flight wall (TFW) and New Time of Flight wall (NTF) are examples of this kind of detectors. Since the structure of these detectors is almost the same, the calibration is performed using the same procedure.

In this section the calibration of those detectors will be described and specific problems during the process belong to the NTF will be presented.

5.2.1 Time reconstruction

The plastic scintillator paddle is readout by photomultiplier tubes from each side delivering time and energy signals.

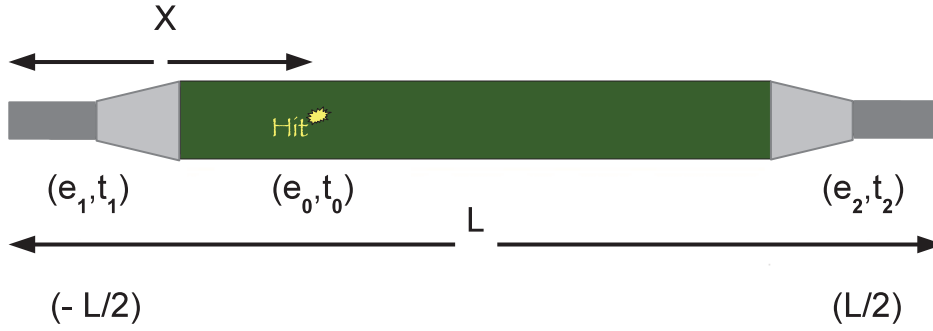


Figure 5.2: Schematic view of a single scintillator paddle. The position of the hit in the paddle can be reconstructed using the time and energy signals measured by the two PM tubes at the edges of the paddle. The time and energy signals measured by each PM depend on the distance of the hit (x) to the edges of each paddle.

Figure 5.2 shows a schematic view of the paddle that is hit by a particle at the distance x from the center at time t_0 . Then the position, energy deposition (e_0) and the time (t_0) of the hit can be reconstructed using the times and energies measured by the two photomultipliers. The quantities (t_1, e_1) and (t_2, e_2) from each photomultiplier are defined as:

$$t_1 = t_0 + \frac{\frac{L}{2} + x}{\nu}, \quad t_2 = t_0 + \frac{\frac{L}{2} - x}{\nu}, \quad (5.1)$$

where L is the length of the paddle, ν is the effective speed of light in the material of the paddle. The time of the hit (t_0) can be expressed by averaging the two time signals (t_1, t_2) from PMT1 and PMT2 as:

$$t_0 = \frac{t_1 + t_2}{2} + \frac{L}{2\nu}, \quad (5.2)$$

which is independent of the position of the hit. From equation 5.1 the time delivered by each photomultiplier depends on the x position of the hit. Accordingly, the x position can be reconstructed as a linear function of the time difference of the two PMTs:

$$x = \nu \cdot \frac{t_1 - t_2}{2}, \quad (5.3)$$

5.2.2 Energy reconstruction

The energy measured at each end of the panel has an exponential dependence on the position of the hit. The energies measured from both photomultipliers are derived as following:

$$e_1 = e_0 \cdot \exp\left(-\frac{L/2 + x}{\lambda}\right), \quad e_2 = e_0 \cdot \exp\left(-\frac{L/2 - x}{\lambda}\right), \quad (5.4)$$

where λ is the light attenuation length in the scintillator material. One can derive the following expression for the total energy (e_0) deposit of the hit in the detector:

$$e_0 = \exp\left(\frac{L}{2\lambda}\right) \sqrt{e_1 e_2}, \quad (5.5)$$

which is also independent of the position of the hit. This is true under the simple assumption of an exponential attenuation. Using equation 5.6 the x position of the hit can be reconstructed as a linear function of the natural logarithm of the energy signals ratio from both PMTs:

$$x = \frac{\lambda}{2} \ln\left(\frac{e_2}{e_1}\right). \quad (5.6)$$

The equations 5.3 and 5.6 are related to the first step of the calibration procedure within the *land02* package, which is the internal time and energy synchronization of one paddle. This requires two parameters: a time difference offset in order to synchronize both PMTs, and the effective speed of light in the scintillator in order to calculate the position. A time difference offset (T_{diff}) is introduced. The synchronized times can be expressed using the measured ones as:

$$\acute{t}_1 = t_1 - T_{diff}, \quad \acute{t}_2 = t_2 + T_{diff}. \quad (5.7)$$

Once the hit occurred in the middle of the paddle, the light arrives at both PMTs simultaneously. Therefore, the calibrated time difference has to be zero and the x position can be expressed as:

$$x = \nu \frac{\acute{t}_1 - \acute{t}_2}{2}, \quad x = \nu \frac{t_1 - t_2}{2}. \quad (5.8)$$

5.2.3 Crossed paddles algorithm

For a single paddle the calibration parameters are difficult to obtain because in order to determine T_{diff} and ν , the position of the hit has to be known from a different source. Therefore, crossed paddles are used to determine those parameters. The extra position information of where the two perpendicular paddles cross can be used: the coordinates of a particle hit of two perpendicular paddles provides a rough information about the position of the hit. The x position is known from the crossing of the paddles and time signals are measured in a way that the needed calibration parameters are delivered from the linear fit of x versus $(t_1 - t_2)/2$.

Exactly the same way is used to obtain the energy calibration parameters, providing a value for λ and the energy difference parameter E_{diff} for the gain matching of the PMTs. The synchronized energies can be expressed using the measured ones as:

$$\acute{e}_1 = e_1 \cdot E_{diff}, \acute{e}_2 = e_2 \cdot \frac{1}{E_{diff}}. \quad (5.9)$$

The next step of the calibration procedure is the synchronization of all paddles with respect to each other. For this purpose it is assumed that the particle hits both crossed paddles at the same time. That means that the measured time in both paddles is equal and the energy deposited in both paddles is the same. Consequently, the T_{sync} and E_{sync} parameters are calculated for all crossed paddles. However, particular attention has to be paid to the method of deriving those parameters. In the case when the parameters are calculated for different groups of files, each group may receive a different offset which needs to be applied to the *land02* framework. When calibration parameters are applied, it is recommended to check them by plotting time/energy versus the number of files (or event). One can investigate their behavior during the experiment.

5.3 Calibration of the individual detectors

Before any physics can be derived from the data, all detectors have to be calibrated and internally/externally synchronized in energy and time. Since different detector types are used, such as NaI crystals, semiconductors, plastic scintillators and drift chambers, all detector types need to be calibrated individually. For that reason different beam settings, such as a sweep run and a pixel run, were used during the experiment in order to be able to calibrate those detectors.

The sweep run is used to calibrate detectors like TFW, NTF which consist of plastic scintillators with PM tubes. The beam is swept horizontally across the detector in order to illuminate the active area of the detectors in the horizontal direction. A vertical sweep, while desirable, is not possible.

The pixel run is used to calibrate the position of the PSP detector. A special grid mask is implemented in front of the detector with a well-known distance between holes on this mask.

The description of the calibration procedure of some individual detectors using the different beam settings is provided in the following subsections.

5.3.1 ToF Walls: NTF and TFW

NTF

As already mentioned, the New Time of Flight wall, placed after the ALADIN magnet, is used to derive the time of flight of the heavy ions between the target and NTF and to measure their energy loss. The latter allows to determine the charge Z of the detected fragments which is proportional to the square root of the energy loss and the velocity, using the Bethe-Bloch formula:

$$Z \propto \beta\sqrt{\Delta E}. \quad (5.10)$$

In order to calibrate the detector, a special **sweep run** is used which allows to illuminate all vertical paddles by modifying the horizontal position of the beam. Most parts of the calibration and reconstruction procedures are done within the *land02* framework as:

- RAW level

The energy and time of each paddle of both PMTs are described as:

$$E_1, T_1 \text{ (PMT1)} = E_{1raw}, T_{1raw};$$

$$E_2, T_2 \text{ (PMT2)} = E_{2raw}, T_{2raw};$$

- TCAL level

QDC Pedestal calibration

The QDC pedestal is obtained by determining the real zero of the energy scale, when no event occurred in the detector. It is done by a pulse generator ("clock" trigger), typically at a rate of 100 Hz. Figure 5.3 shows a typical pedestal distribution for one energy channel of the NTF detector. The peak mean value of the distribution has to be subtracted from the energy entries. This is done by the DAQ for the zero-suppression.

The energy of each paddle from both PMTs are presented as:

$$E_{1tcal} \text{ (PMT1)} = E_{1raw} - \text{Pedestal};$$

$$E_{2tcal} \text{ (PMT2)} = E_{2raw} - \text{Pedestal};$$

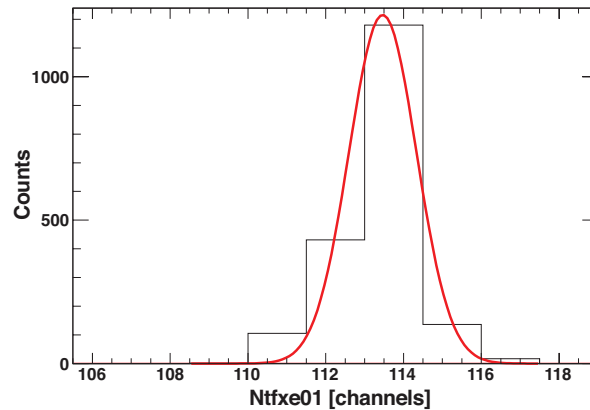


Figure 5.3: Typical example of the pedestal distribution of one channel NTF detector.

TDC Gain calibration

The TDC modules, that were used during the whole experiment, contain a nominal slope value, which is typically 25 or 50 picoseconds per channel. Due to the fact, that the real value of the gain during the experiment can slightly deviate from the nominal value, the TDC gain has to be measured. Using the data from a time calibrator pulser, running during the whole experiment, one can convert time from the electronic channels to nanoseconds. The random time pulser is generating start and stop signals with an adjusted range between 100 - 400 ns. The upper plot of figure 5.4 shows a distribution of the time calibrator data. The calibration Time_{gain} and Time_{offset} parameters are extracted from the linear fit T_{cal} data (in ns) versus Time_{raw} data (in channels) by using the *tcal* program within the *land02* package. Figure 5.4 presents typical calibration plots for the the NTF detector by selecting the corresponding trigger for the time calibrator events.

The calibrated time value of each paddle of both PMTs are presented as:

$$T_{1tcal} (\text{PMT1}) = T_{1raw} * T_{gain} + T_{offset};$$

$$T_{2tcal} (\text{PMT2}) = T_{2raw} * T_{gain} + T_{offset};$$

where T_{offset} does not contain any physics information and is set to zero.

The provided input file with the calibration parameters (slope and offset) for each channel has to be implemented in the *land02* framework for further analysis. In order to complete the calibration procedure, the time of each individual signal of the same detector or between the different detectors had to be synchronized.

- SYNC level

Time/Energy synchronization for each PMTs

$$E_1 (\text{PMT1}) = (E_{1raw} - \text{Pedestal}) * \text{Energy}_{diffgain} * \text{Energy}_{syncgain};$$

$$E_2 (\text{PMT2}) = (E_{2raw} - \text{Pedestal}) * 1/\text{Energy}_{diffgain} * \text{Energy}_{syncgain};$$

$$T_1 (\text{PMT1}) = T_{1tcal} + T_{offset};$$

$$T_2 (\text{PMT2}) = T_{2tcal} + T_{offset}.$$

After applying calibration parameters in the SYNC level for the energy and time of each paddle and each PMT, it converts to one energy and one time for each paddle (DHIT level). The time and energy for each paddle with two photomultipliers are calculated as:

$$t = \frac{t_1 + t_2}{2} \tag{5.11}$$

and

$$E = \sqrt{e_1 \cdot e_2}/2. \tag{5.12}$$

Finally, the HIT level within the *land02* framework considers the full detector and delivers only one energy and one time for each event and the position of the hit is derived via $\text{position} = \nu \cdot (t_1 - t_2)/2$, where ν is the effective speed of light in the paddle. An example of the synchronization procedure for the NTF detector for the

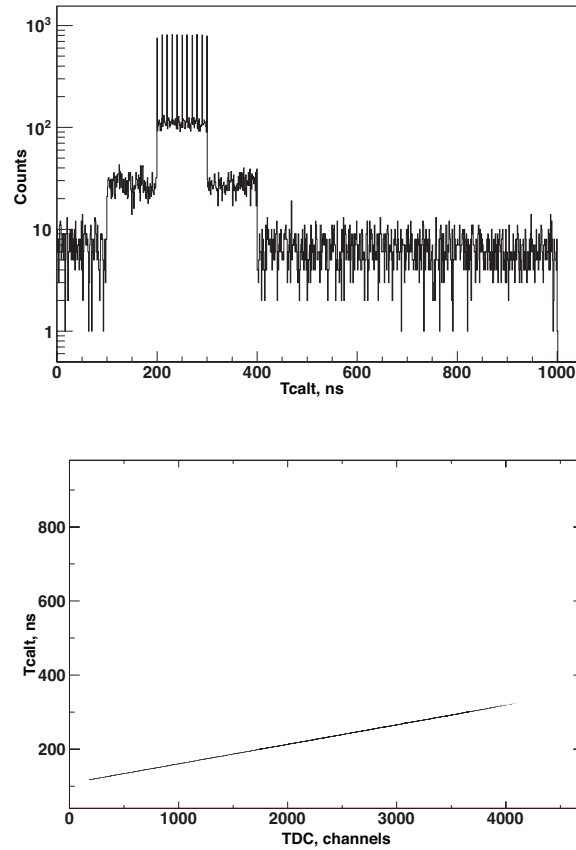


Figure 5.4: The time calibrator (Tcal) events. A linear correlation is plotted between the time presented in nanoseconds (Tcalt) and time in channels from the TDC.

individual PMTs of one paddle is shown in the figure 5.5. The time resolution (see Fig. 5.6) derived from the Gaussian fit is $\sigma = 42.13 \pm 0.34$ picoseconds. The resolution for the whole detector can be estimated via $1/\sqrt{2} \cdot \sigma_t$.

TFW

Since the TFW, the big Time of Flight wall, is very similar to the NTF, but larger, the calibration procedure is the same and will not be described in detail here.

5.3.2 GFI and PSP position calibration

The main goal of the calibration of GFI and PSP is to get precise position information from both detectors expressed in centimeters relative to the center. The procedure relies on the read-out masks. For the PSP detectors, an active mask is equipped, which has a square shape alike the PSP detector and consists of 21x21 square pixels made

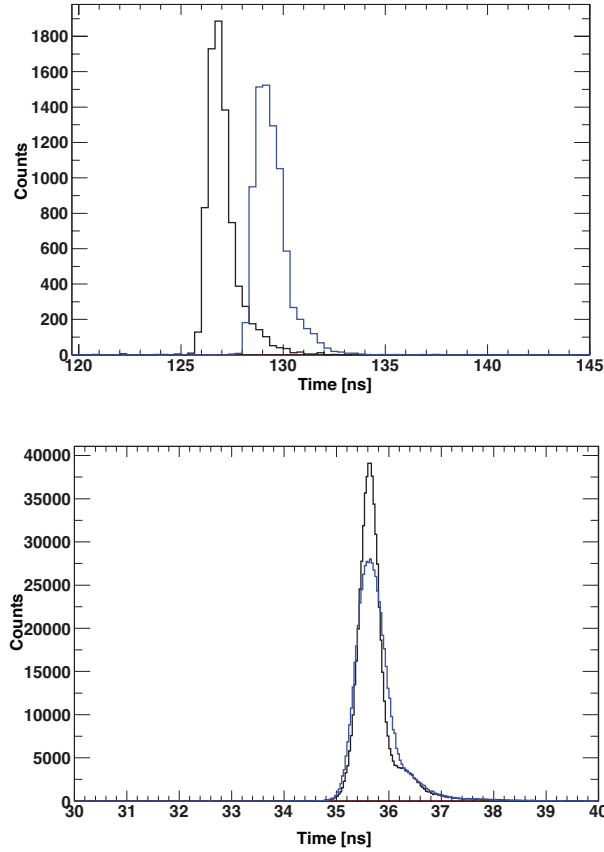


Figure 5.5: The time of the NTF detector before (top) and after (bottom) the synchronization. The time of the hit in the NTF detector is derived from each photomultiplier of each paddle (TCAL, SYNC levels). The blue spectra represents the time from the first PMT1 and black one is from the second PMT2.

of scintillator material. The pixels are arranged in a grid in a way that the distance between them is 2 mm, while each side of the pixel has a length of 0.5 mm (see figure 5.7). The pixels are inlaid into a transparent plastic plate which at the same time serves as a light guide and is coupled to a single photomultiplier tube. The mask can be embedded in and removed after collecting the calibration data from the beam line by a remotely controlled device. During the experiment a **pixel run** is used in order to collect calibration data for the PSP. In case of the GFI, in order to hit all fibers and illuminate the full readout grid mask and to be able to proper gain-match all anode wires of the detector, a **sweep run** was used. The mask was built-in in the detector in a way that all fibers are located in a two dimensional pattern on the surface of the PSPM photocathode. During the calibration run only particle that hit a pixel and produces a light is guided through the fibers and causes a well-defined light spot on the photocathode. An electrical signal is thus produced in some of the anode wires of

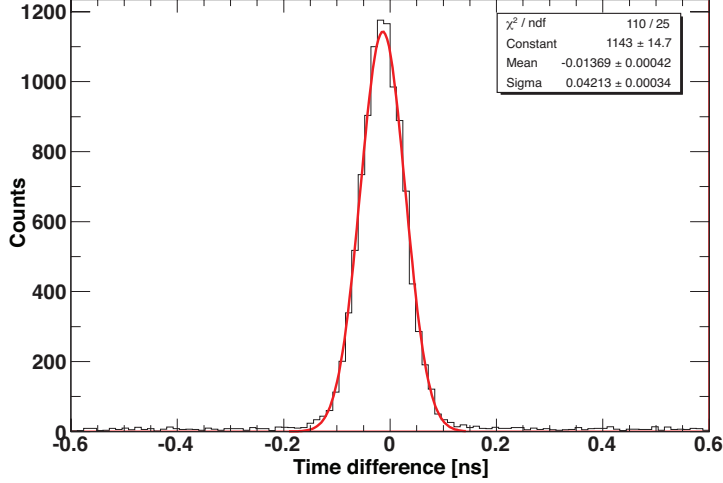


Figure 5.6: The time resolution of the NTF detector is $\sigma = 42.13 \pm 0.34$ picoseconds.

the detector, depending on the 2D position of the light spot on the photocathode. By combining information from these signals, one can precisely reconstruct the position of the light spot on the photocathode and identify the hit fiber.

The main steps of calibration algorithm [54, 55] which was used in the analysis are the following:

- Determination and subtraction of the QDCs pedestals (TCAL level). Using the "clock" program installed within the *land02* package, pedestals are subtracted for all ν and $\bar{\nu}$ PSPM wires.
- PSPM anode gain matching (DHIT level).
- Finding the $(\nu, \bar{\nu})$ clusters. (Finding and assigning an internal $(\nu, \bar{\nu})$ coordinate to each cluster).
 - Indexing. (Assigning indexes to the grid points and finding neighbors).
- Real coordinates position reconstruction (HIT level).

For both types of detectors (GFI and PSP), on the DHIT level, the position is defined in their internal length units or a set of $(\nu, \bar{\nu})$ coordinates. Later on in the HIT level these $(\nu, \bar{\nu})$ coordinates need to be transformed into the real (x, y) for the PSP or just (x) for the GFI. In the following as an example the GFI reconstruction will be described. As mentioned above, the light produced by the hit in the detector is guided through the fibers thus creating a light spot on the photocathode. In principle, combining information from these signals one can precisely reconstruct the light spot position on the photocathode and identify the hit fiber. Since the amplitude of the

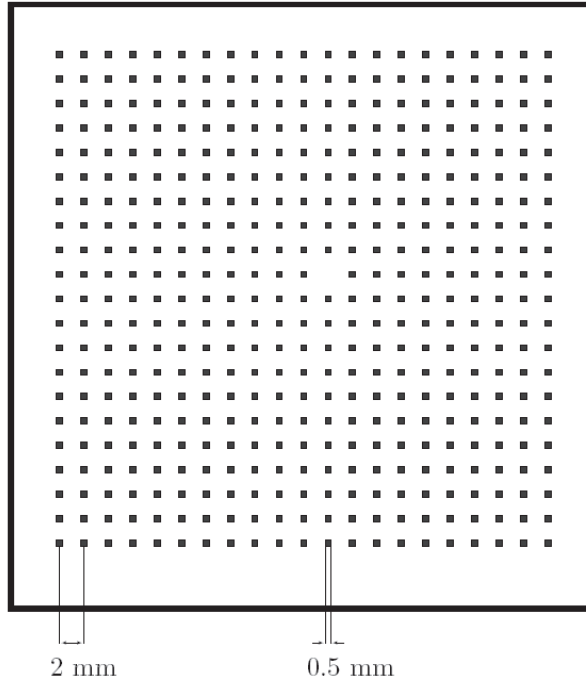


Figure 5.7: Schematic view of the pixels detector.

signals depend on their amplification (which can be different for each signal) and on their positions on the PM tube (see top figure 5.8), a proper gain matching needs to be performed before proceeding with the hit position reconstruction.

In general, the charge distribution of a hit will produce electrical signals in several neighboring wires (clustering) in each (ν, ν) direction. Their amplitudes are expected to form a Gaussian-like distribution which can be used to gain-match the wires by requiring all signals from neighboring wires to fit in this shape [54]. Since the gain matching is performed in the sweep run (i.e. the whole range of the detector is covered homogeneously), the gains for each wire are derived simultaneously for all wires. Due to the gain-matching, the mean position of the charge distribution for each hit provides the (ν, ν) coordinates of the light spot. Usually a sweep run results in a proper reconstruction of all the light spots which correspond to the fibres. The reconstructed fibres in the (ν, ν) coordinates before (top) and after (bottom) gain matching are shown in figure 5.8. As can be seen in this illustration, for each (ν, ν) pair there is a point and most of these points form in principle well-defined clusters, but there are also points in-between the clusters (noise), which have to be considered. Apart from that, as a result of the geometrical construction of the PSPM mask in GFI, the clusters are expected to orthogonal grid (k, l) in the xy -space. However, in the $\nu\nu$ -space this image is distorted due to non-linearities (Fig. 5.8). In order to account for this effects and extract

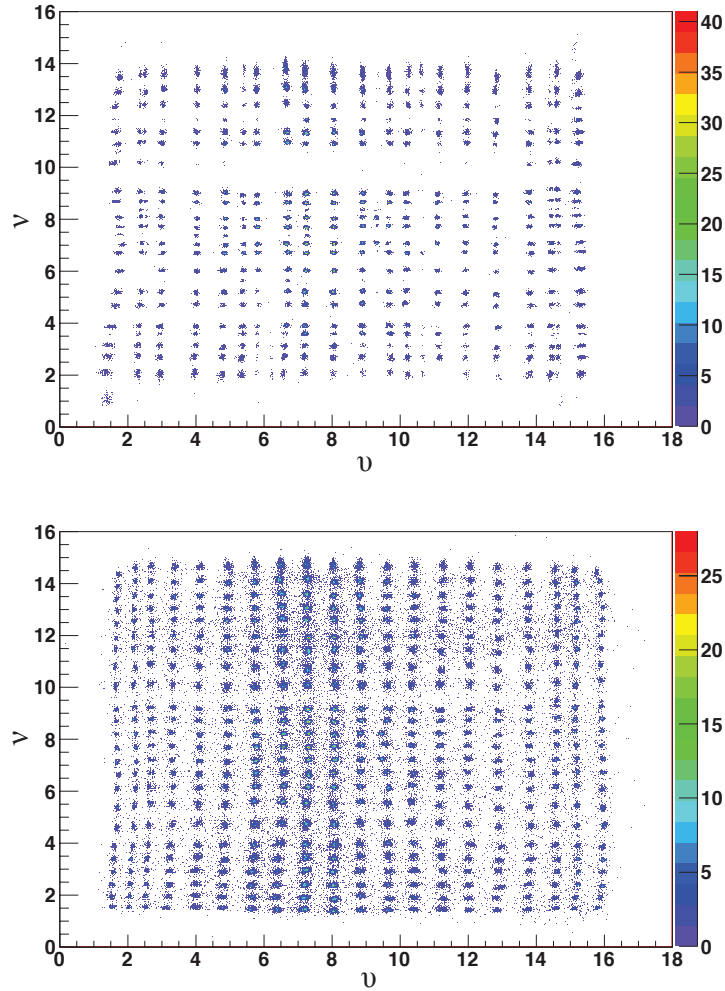


Figure 5.8: The plot of the GFI detector in (v, ν) coordinates before (top) and after (bottom) gain matching. Each cluster of dots corresponds to a fibre.

the exact (v, ν) positions of each cluster and then associate them with corresponding fibres a specially developed algorithm is used [54, 55]. In its first step, based on density of points and a signal-over-noise, certain points are assigned to their clusters. In the second step of the algorithm, the clusters are indexed in two dimensions (k, l) in order to associate each cluster in the v, ν -space with its expected position on the orthogonal grid of the xy -space.

Once the (v, ν) position of each fibre on the mask is found and indexed (k, l) , a transformation is needed to connect each point of the $\nu\nu$ -space to the corresponding x -position. In order to reconstruct the x -position, a weighted average of the candidate

fibres is used:

$$Position = \frac{\sum p_{kl} x_{kl}}{\sum p_{kl}}, \quad (5.13)$$

where x_{kl} is the position of the corresponding fibre in the detector and p_{kl} is the probability of the hit to belong to the grid point (k, l) (i.e. probability of the hit to belong to the kl -fibre). The probability p_{kl} depends on the distance of the hit from the kl -cluster and on the widths of the cluster in both v - and ν -directions. The sum is required in order to include both closest grid points and their neighbors.

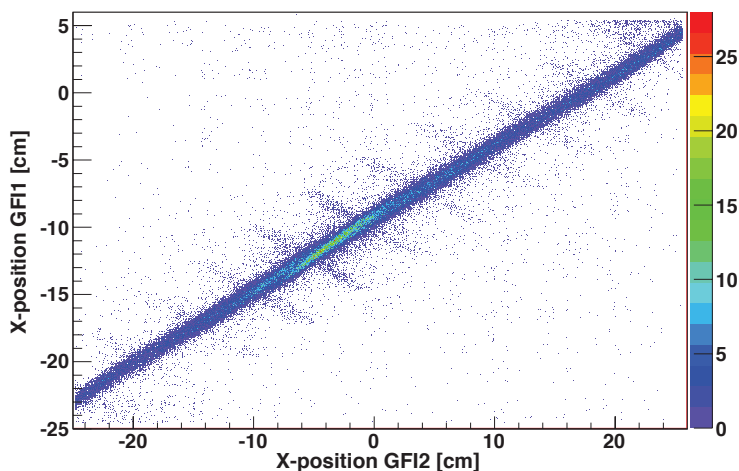


Figure 5.9: Figure shows a reconstructed position correlation between two fiber detectors GFI1 and GFI2. Some bars along the correlation line are coming from wrong position identification.

After the calibration parameters are applied into the *land02* framework one can check how well position reconstruction works for both detectors by plotting the correlation of the x -positions of the GFI1 and GFI2. Figure 5.9 shows that the detector is fully illuminated by the sweep run used for the calibration. Some anti-correlated bars along the correlation line can be explained by insufficient statistics to fully reconstruct the (ν, ν) points.

5.3.3 Proton Drift Chamber (PDC)

Position reconstruction procedure

The main principle of work of the drift chamber is based on the ionization of the chamber gas along the trajectory of a the interacting particle. Due to the potentials in the cells, the produced electrons drift towards the read-out wires producing avalanches, thus inducing currents on these wires. The timing information from the induced signals is related to the interaction position in the detector. This relation between the signal

(or avalanche) arrival time t and the drift distance r from the corresponding hit position is the subject of the calibration procedure.

As described in section 4.6.3, the PDC has hexagonal forms of the cells. This design simplifies the identification of the drift distances, because due to the semi-cylindrical symmetry the drift distance relation depends only very weakly on the particles incident angle. The calibration procedure is as follows:

- Time calibration from channels to ns (SYNC level).

The time is extracted from the PDC header which is stored in the data file and hence does not need any external calibration. To obtain time in ns, each channel value is multiplied with 2.5 ns, what allows the electronics settings for the current experiment.

- Position calibration of the hit in cm (DHIT level).

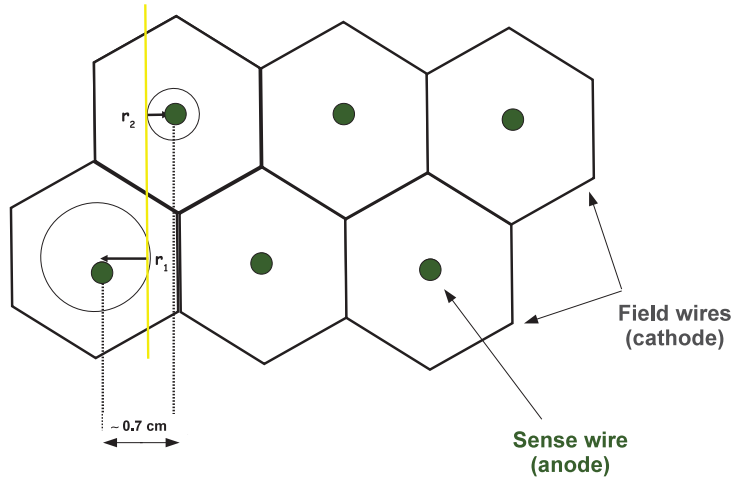


Figure 5.10: One layer contains two rows of sense wire anodes and having hexagonal structure cathode wires. To reconstruct the distance the drift lengths r_1 and r_2 derived from the measured drift times are used.

A proton passing the PDC in the direction approximately perpendicular to the detector surface crosses two adjacent cells of each (x and y) layer (see figure 5.10), and thus can be defined by two radii r_1 and r_2 for each cell. Already here the position of the track within the inter-wire distance 6.92 mm can be determined. Particles passing through the cells number k and $k + 1$ with the corresponding sense wire coordinates x_k and x_{k+1} respectively, the position can be determined as:

$$Position = \frac{x_k + x_{k+1}}{2}. \quad (5.14)$$

In other words, the position of a hit is in the first order determined by the location of the wires which were hit. However, one can determine the position of a track with a much higher accuracy by taking into account the drift time of the electrons. The measured drift time t can be converted into radius r . Assuming that the dependence between the drift time t and the drift length r is known, the position between two sense wires x_k and x_{k+1} can be expressed as:

$$Position = \frac{x_k + r_k + x_{k+1} - r_{k+1}}{2}. \quad (5.15)$$

The dependence between the drift time t and the drift length r , so called $x(t)$ -curve, can be determined using experimental and simulation methods. In this thesis this was done using experimental data. Assuming that all positions between adjacent x_k and x_{k+1} sense wires have the same probability to occur and the hits are perpendicular to the PDC, the drift lengths follow a box-like distribution of drift lengths between 0 and 6.92 mm (cell size). Even though, this is a rather rough assumption, it can be used as a first order approximation. Now taking the measured arrival times into account along with the box-like drift length distribution, the mapping between x and t is defined and can be deduced. However, some quality requirements for the calibration need to be fulfilled in order to select from the real data the events useful for the calibration. These events require, that hits occur in two cells in a way that the distances of the trajectory from the centre of the cell can be determined and the area of all particles passing through the detectors has to be compared to the cell size to ensure that all drift lengths are equally occupied. In addition it is required that the protons are impinging the detector perpendicularly. Preliminary $x(t)$ -curve is then copied into the calibration file of the *land02* framework. It allows to calculate an approximate value for r_1 and r_2 (see figure 5.10). An event is taken to the calibration only if $r_1 + r_2$ is equal to the cell size of 6.92 mm. The start-time value (figure 5.11) is varied until the final result reaches a rectangle of 6.92 mm length.

As an example, a part of the $x(t)$ -curve for the PDC1, represented by a list of points assigning the drift time to the drift length, looks as following:

```
PDC_XTC_POINT (SIGNAL_ID (PDC, 1) , (19.0, 0.013), (0.0) );
```

```
PDC_XTC_POINT (SIGNAL_ID (PDC, 1) , (32.6, 0.051), (0.0) );
```

where the first value represents the drift time 19.0 ns, which is equivalent to the drift length of 0.013 cm. The full table (list) is finally provided as the calibration data to the *land02* framework.

The bottom frame of figure 5.11 shows the status of wires for the first drift chamber PDC1. One can easily see two holes in the distribution meaning that two wires are broken. Since the analysis is very sensitive to the correct determination of the number of emitted protons of the reaction, this effect needs to be corrected. The efficiency and acceptance correction for the proton arm is applied and it's described in the sections 6.3 and 6.4.

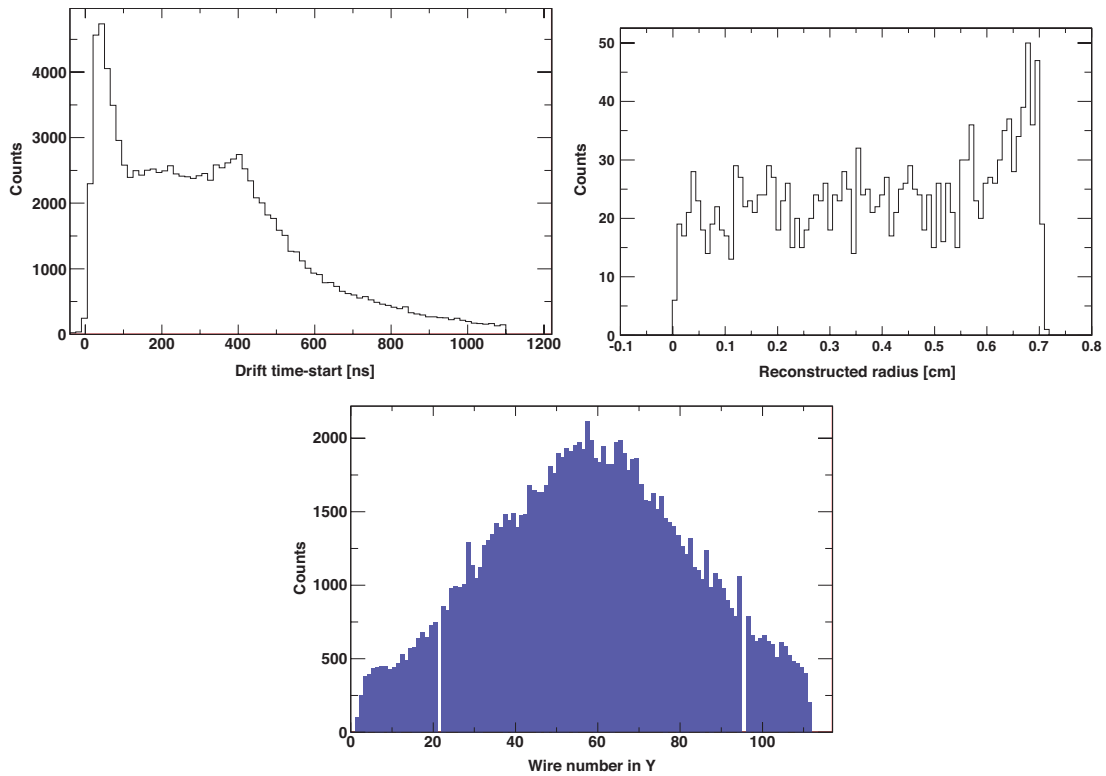


Figure 5.11: One dimension spectra (top right) presents an example of the reconstructed radius r_1 in cm after the $x(t)$ -curve applied. Top left represents a measured arrival time used to calculate an $x(t)$ -curve. The status of wires for the first drift chamber PDC1 is shown (bottom). One can see two holes in the distribution meaning that two wires are broken.

5.3.4 Calibration of the gamma detector

Energy calibration

For the detection of the γ -rays emitted by heavy fragments after a transition from an excited state to a lower state, the Crystal Ball detector is used. Gamma rays need to be detected in order to have a full reconstruction of the excitation energy of the projectile. The γ -rays are emitted by relativistically moving particles, leading to very large Doppler shifts and Doppler broadening. Before extracting the gamma-radiation emitted in the reaction, each 162 crystals of the photon-detector has to be calibrated individually. For the energy calibration, different runs with three different γ -ray sources were implemented. Each source was placed on the empty target position in the middle of the Crystal Ball using the XB OR trigger. The calibration sources used in the S327 experiment are presented in table 5.1.

Peak positions for the raw ^{22}Na , ^{88}Y and PuC (a composite of α -radioactive ^{238}Pu and stable ^{13}C) single crystal spectra were determined assuming a linear background under the peak in the vicinity of the peak $= \pm 3\sigma$. Examples of the fitted raw spectra

Table 5.1: The calibration γ sources and their characteristics. Three different sources give an opportunity to check the linearity of the energy calibration of the Crystal Ball.

Source	E_γ [keV]	Activity [kBq]
^{22}Na	511, 1275	154
^{88}Y	898, 1836	10.9
PuC	6130	4 (γ)

for crystal 131 for ^{22}Na , ^{88}Y and PuC γ -lines are shown in figure 5.12. Due to the fact that long-lived ^{22}Na source cannot deliver high energy range, ^{88}Y and PuC sources, which emit photons with the high energies (up to 1.84 MeV for ^{88}Y and 6.13 MeV for PuC), are used. Since the PuC source is predominantly a neutron source, the spectra contain a considerable amount of background from high-energy neutrons. In order to see the γ -peak, the spectra have to be purified from a large neutron background using an additional cut on a multiplicity of one. The effect of the multiplicity cut condition on a single crystal 131 spectrum is shown in figure 5.12. The energy calibration is performed using the relation between the energy in QDC channels and 5 known photo peak energies in keV. The *land02* framework requires a linear conversion from channels to keV units, therefore the calibration parameters such as slope (gain) and the offset (zero energy in terms of QDC) for each individual crystal are needed:

$$E(\text{MeV}) = E(\text{ch}) \times \text{slope} + \text{offset}. \quad (5.16)$$

Time calibration

The measured times from each crystal needs to be synchronized relative to all other and an additional global time offset needs to be applied. By knowing the time from the gamma detector, the data can be cleaned up from the background in order to have only events which come from the same nuclear decay. Using the *gamma2* program, within the *land02* framework, the time calibration procedure was performed. The program looks for the full energy peak coming from a coincident-cascade from the ^{88}Y source in all possible pairs of crystals. In this process, the time differences between all crystal pairs are set to zero.

5.3.5 Hit Reconstruction

Addback Algorithm

During the analysis one can see that the γ -rays are scattered to the neighboring crystals. These gamma-rays interact again with the detector material and registered further. In order to define how many crystals fired and have registered signals, a special algorithm needs to be applied. This algorithm combines the energies of the emitted γ -rays from neighboring crystals and creates a cluster with one final energy. To define the neighboring crystals, the map of the positions of all crystals in the Crystal Ball is used. The result of the add-back procedure is an information of γ clusters (Doppler corrected)

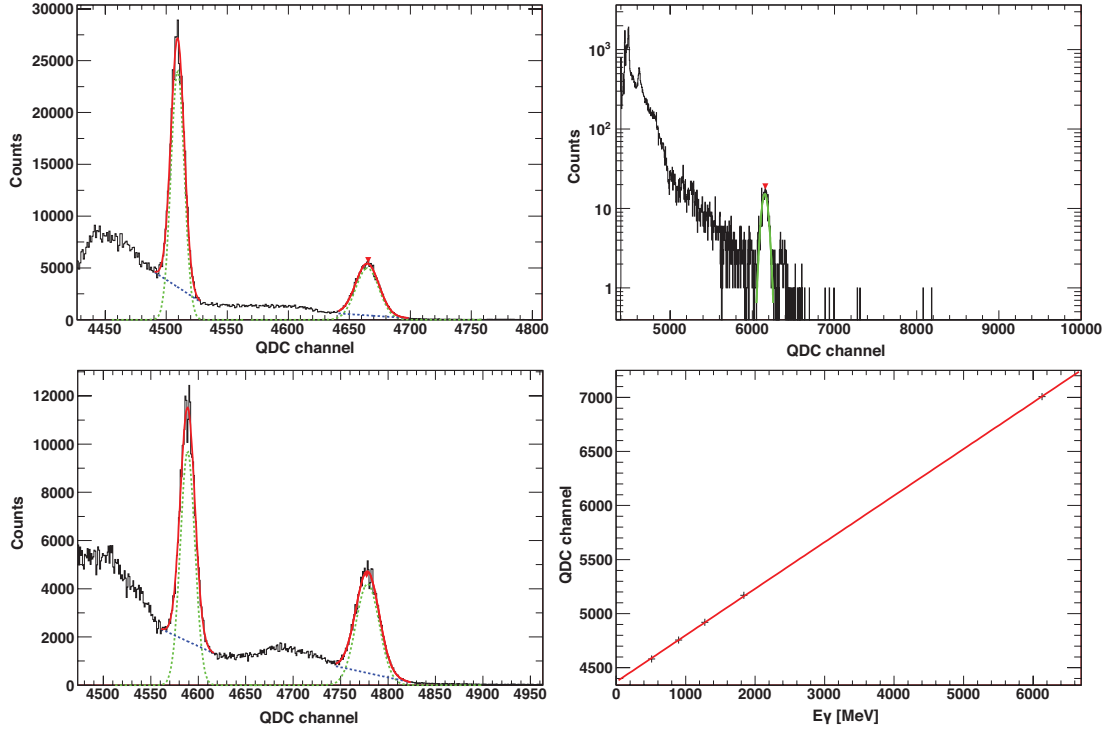


Figure 5.12: Upper left frame of the plot presents an example of the peak fitting for the ^{22}Na (511 keV, 1275 keV), ^{88}Y (898 keV, 1836 keV) and PuC (6130 keV) sources (upper right frame). Red solid lines represent the fit function for the peaks. A background of the function is shown with blue dashed lines. The Gaussian peak component are presented in green dotted lines. The sharp peaks (channel number 4450) at the left side of the spectra can be explained as a reminders of the cut-off pedestals. Bottom right: Energy calibration curve for crystal 131. The linear correlation between the known energies (5 points) of calibration γ -rays and their positions measured in raw QDC channels. The procedure has been done for each individual crystal. Parameters of the linear calibration function, such as gain and offset, are found by linear regression.

for each event which characterize a certain reaction channel. The Doppler correction procedure applied to the gammas is described in the following subsection.

Doppler correction

Each identified gamma cluster energy which is specific for a certain reaction channel is corrected for the relativistic Doppler shift using the known formula:

$$E_{c.m.} = E_{lab} \cdot \gamma_{frag} \cdot (1 - \beta_{frag} \cdot \cos \theta), \quad (5.17)$$

where β is the velocity of the de-excitation fragment, θ is the polar angle between the central crystal of the cluster and the flight direction of the fragment in the laboratory system. For the analysis presented in this thesis, the gamma data from the Crystal Ball are used for the invariant mass reconstruction.

5.4 Stability of the calibration parameters

After the calibration parameters are calculated and applied into the *land02* code, they are carefully checked. During the procedure, one can investigate their behavior during the experiment and find that calibration parameters are moving during the experiment. This effect has to be corrected. Typically, a width of the position spectra is determined by the length of the paddle and the effective velocity of light in the scintillator. It should be independent of the difference of the time offsets in the various time circuits. In order to adjust them, all position spectra need to be centered. This can be done if one adds T_{diff} offset to one photomultiplier tube time signal of one paddle and subtracts from the other. One has to take into account that two hits of the same particle in neighboring crossing paddles happen at the same time. The adjustment of this T_{sync} offset is described thereafter. Considering that fact that there is no way to introduce a "reference" paddle, a common condition is applied:

$$\sum_{allpaddles} T_{sync} = 0. \quad (5.18)$$

After all offset parameters are calculated, the time signal can be expressed by

$$Time = T_{raw} \cdot k + T_{tcal} + T_{diff} + T_{sync}, \quad (5.19)$$

where k is a gain (nanosecond/channel), T_{raw} is the raw time signal expressed in channels and T_{tcal} is the time calibrator offset which applied in order to have time calibrator pulses started at time zero. The T_{tcal} and gain k are calculated for all channels first using the *tcal* routine implemented in the *land02* software. Afterwards, T_{diff} and T_{sync} are calculated.

As an example, the calibration of the time signals in the NTF is described.

The T_{tcal} parameters are calculated for each channel and each photomultiplier. Due to this all parameters depend on T_{tcal} and need to be corrected first. Since we mainly operate with the time differences, a common drift of all channels is equivalent to a stable behavior. However, it is found that sometimes for some channels the parameters during the experiment are drifting with time as shown in the plots of Fig. 5.13. Therefore, the individual channels with not normal drift have to be corrected. Thus, for each channel motion of the parameter can be split into two groups, one which are common to all channels, other which are specific only to problematic channels. The further corrections will be applied only to problematic channels. The procedure is as following.

If there is a difference between T_{tcal} parameters, calculated for the 1st file and for the 2nd, the mean value of them (after the gaussian fit of the distribution) may be defined as a common shift for all channels between the 1st and 2nd files. This procedure should be done for the 2nd and 3rd, 3rd and 4th files and so on. By knowing all shifts, the common motion of the parameters can be eliminated as:

$$T_{tcal}^{cor}(k) = T_{tcal}(k) - T_{tcal}(1) - \Delta T(k, 1), \quad (5.20)$$

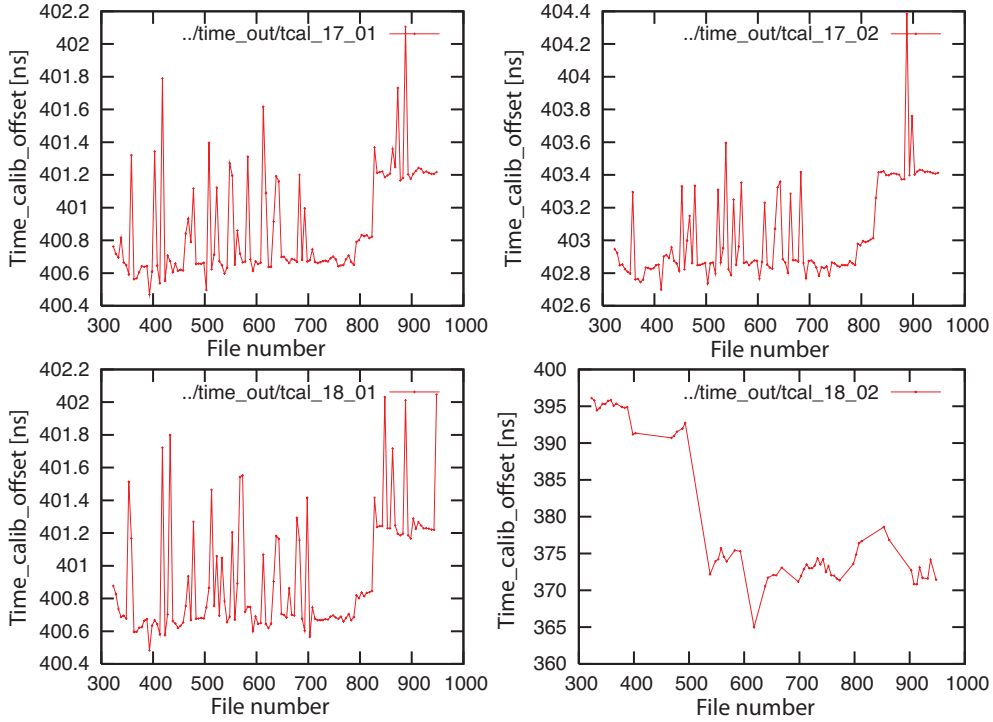


Figure 5.13: Dependence of T_{tcal} parameter as a function of data-file number on time. Lower plot (left) shows the example of the drifting channel for paddle 18 of TWF, second PM tube. The rest plots, represents a "normal" motion, common to all channels.

where $T_{tcal}(k)$ is the time calibrator offset calculated for the k^{th} file and $T_{tcal}(1)$ is the time calibrator offset calculated for the 1^{st} file respectively. $\Delta T(k, 1)$ is the mean value of the shifts between k^{th} and first files. After the corrections have been applied into the *land02* code to the problematic channels, one can check the calibration parameter by plotting $T_{tcal}^{cor}(k)$ (see figure 5.14). After all the correction for T_{tcal} parameters for all problematical channels are applied, T_{diff} and T_{sync} parameters have to be recalculated and further checked in the same way as for the T_{tcal} .

5.4.1 Possible NTF issues

The NTF detector is used to measure the time of flight and the energy loss measurements of the heavy fragments. To calibrate and synchronize all individual paddles of the detector, a sweep run is used which swept through the all vertical paddles. During this procedure, a few problems related to the energy calibration were discovered. Looking to figure 5.15 one can see that the measured energy along the paddles does not have the same values (upper right frame in figure 5.15), even though the beam energy is fixed. Moreover it has a twisted distribution at the edges of the paddle, producing a so called "smiley effect" (upper left frame in figure 5.15). The light propagation model, used

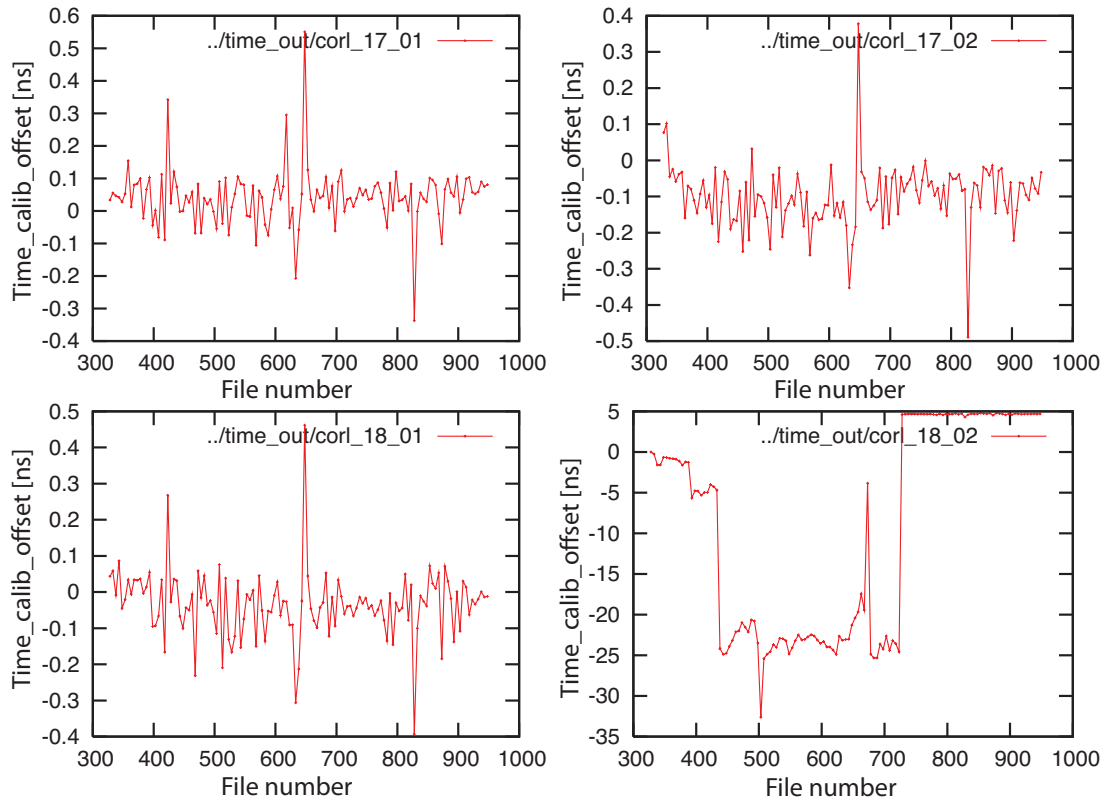


Figure 5.14: Corrected T_{tcal} parameter as a function of data-file number on time. Lower left plot shows an example of pure "anomalous" motion.

within the *land02* package, expects that the energy measured by each photomultiplier has an exponential dependence with the position of the hit (see equations 5.4). In that case higher order effects are not taken into account and the reconstructed energy shows a position dependence, that should not be there. This effect can be corrected as shown in the figure 5.15 (bottom right frame). The other effect might be due to the large energy deposition, that occurs in the paddle close to the photomultiplier, saturating the scintillating ability of the material. The twisted distribution at the edges might appear from partial particle penetration in the paddle and not exact distance between two paddles. The "smiley" effect can be easily corrected as shown in the figure 5.15 (bottom left frame) but since the production beam is distributed around the center of the detector, it does not spoil the energy loss distribution for the different reaction products.

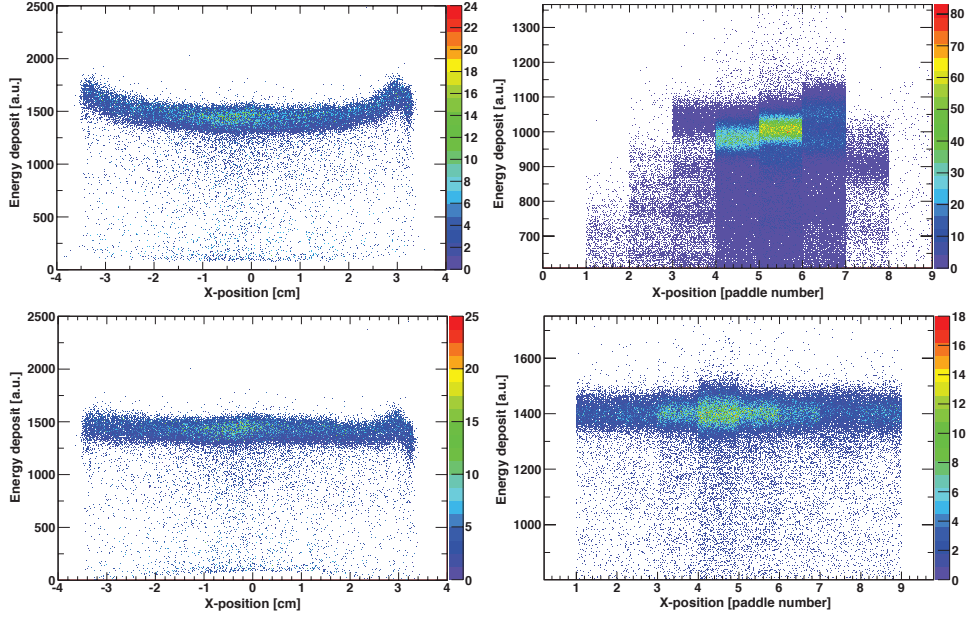


Figure 5.15: The energy deposit distribution versus x position for the horizontal paddle 5, using the sweep run. The x position is derived from the time difference as $0.5 \cdot (t_1 - t_2)$. The smiley effect and the spoiled energy distribution is observed during the calibration procedure which is possible to correct. The lower frames show the energy deposit distribution after the corrections are applied.

5.5 Incoming beam calibration

Velocity calibration

The reconstruction of the invariant-mass requires knowledge of the velocity (β) of the projectile in the moment of decay, i.e. instantaneous velocity inside the target material. The velocity of the ions can be calculated from the time-of-flight (ToF) measurements between the S8 detector placed at the exit of the Fragment Separator (FRS) and POS detector placed at the entrance of the experimental hall. In order to obtain time-of-flight measurements (ToF) from the time measured by the required detectors, the time signals have to be synchronized relative to each other. Knowing the paths length (S) between S8 and POS detectors, the velocity of the projectile can be estimated as:

$$\beta = \frac{S}{(ToF) \times c}, \quad (5.21)$$

where c is the speed of light. The path and offsets (T_{offset}) can be determined as:

$$\Delta t = ToF + T_{offset}, \quad (5.22)$$

where T_{offset} is a time offset due to the different cable lengths. Combining equation 5.21 and equation 5.22 the following equations can be derived:

$$\beta = \frac{S}{\Delta t - T_{offset} \cdot c}, \quad \beta \Delta t - \beta T_{offset} = \frac{S}{c}, \quad (5.23)$$

$$\beta \Delta t = \frac{S}{c} + \beta T_{offset}. \quad (5.24)$$

Runs with three different beam energies of primary ^{40}Ar beam and well-known corresponding magnetic rigidities ($B\rho$) given by the FRS setting were taken to calibrate the identification of the incoming ions, namely for the energy loss calibration in the PSPs and for the velocity calibration (see table 5.2).

Table 5.2: Characteristics given by the FRS setting for runs with three different energies required for the velocity calibration.

Run Number	E (primary) [MeV]	E (S8-POS) [MeV]	FRS Target(Be) [g/cm ²]	β [v/c]	$B\rho$ [Tm]
183	500	486.8	-	0.7541	7.9204
196	500	362.3	6.347	0.6940	6.6499
198	790	778.8	-	0.8386	10.622

By plotting the time difference (Δt) between the S8 detector and POS for three different energies one can extract the mean value for each time difference by fitting of the peaks with a Gaussian (see table 5.3). By knowing the mean values for each time

Table 5.3: Derived parameters for runs with three different energies required for the velocity calibration.

Run Number	Mean Value (POS - S8)	β	$\Delta t\beta$
183	28.08	0.7541	21.1751
196	48.87	0.6940	33.9158
198	3.071	0.8386	2.5762

of flight allows us to calculate the nominal velocity (β) for each different beam energy. The flight path (S) between S8 and POS detectors can be obtained from the offset (-184.59 ns) of the linear fit by plotting $\Delta t\beta$ versus β for three different known beam velocities. The flight path is 55 m. At the same time the global offset for time of flight due to cabling and electronics can be obtained from the slope (216.95 ns) of the linear fit as is presented in figure 5.16.

This offset has to be applied as a calibration parameter in the *land02* framework for the whole experiment.

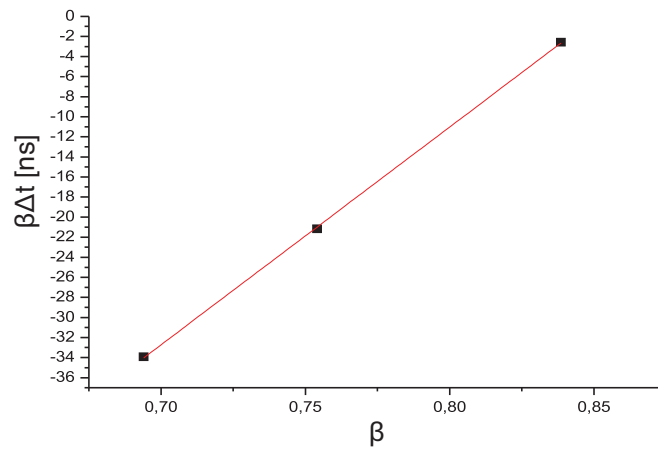


Figure 5.16: Linear fit of $\beta \Delta t$ versus β for the three different calibration runs. The offset of the linear fit is related to the flight path between S8 detector placed at the FRS and POS counter placed in Cave C. The slope from the fit is related to the time offset due to cabling and electronics.

Chapter 6

^{32}Ar and ^{34}Ar data evaluation

After the calibration and reconstruction procedures have been applied, the interesting physical information can be extracted from the experimental data. Since the FRS was set up to have a mixed composition of the secondary beam, the incoming ions of interest have to be selected properly in order to be able to calculate their Coulomb dissociation cross section. Different conditions to select incoming and outgoing reaction channels must be applied. In this chapter the analysis procedure for ^{32}Ar and ^{34}Ar data for one and two proton emission are described. The tracking algorithm with related efficiency and acceptance corrections for the proton branch will be described as well.

6.1 Projectile

6.1.1 Mass identification

After the primary target, the produced secondary beam must be identified in terms of mass-over-charge ratio (A/Z). For this purpose the velocity of the projectiles has to be determined via a time-of flight measurement and its energy loss in a ΔE detector has to be measured. The latter is related to the nuclear charge (Z) via the Bethe Bloch formula (see section 6.1.2). By using the following equation the A/Z ratio of the projectile from the time of flight can be calculated as:

$$B\rho \propto \frac{A}{Z}\beta\gamma, \quad (6.1)$$

where $\gamma = \sqrt{1/(1 - \beta^2)}$ is the relativistic Lorentz factor, $B\rho$ is magnetic rigidity of the projectile. Note, that the energy loss depends on the velocity of the passing ions. The velocity can be calculated from the ToF between S8 detector and POS (see section 5.5):

$$\beta = \frac{\nu}{c} = \frac{S}{(ToF) \cdot c}. \quad (6.2)$$

Figure 6.1 shows extracted velocities β of the different incoming isotopes.

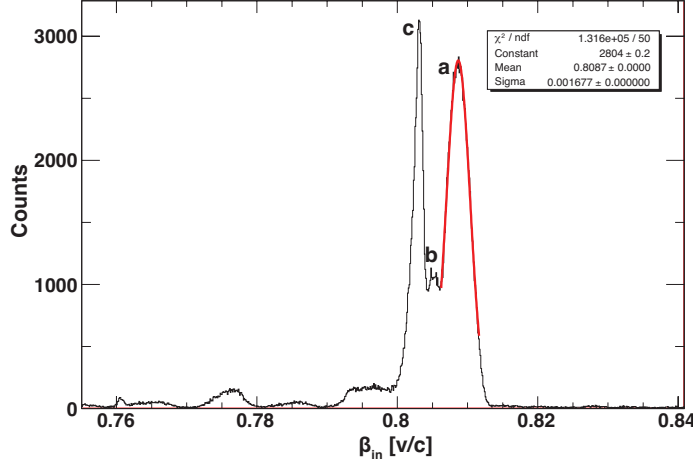


Figure 6.1: An example of the velocity β for the incoming ^{33}Ar (b), ^{31}Cl (c) and ^{32}Ar (a) isotopes.

6.1.2 Charge identification

The silicon PIN diodes (PSP1/PSP2), placed before the target, are used for the energy loss measurements of the incoming beam. The velocity of the incoming beam (β) is measured by means of time of flight measurements between S8 detector, placed at the exit of the FRS, and POS. The charge Z of a particle with velocity ν can be determined by measuring its energy loss when passing through matter, which is related to Z via Bethe-Bloch formula [41]:

$$-\frac{dE}{dx} = \frac{4\pi Z^2 e^4}{m_e c^2 \beta^2} N_z \left[\ln \frac{2m_e c^2 \beta^2}{I} - \ln(1 - \beta^2) - \beta^2 \right]. \quad (6.3)$$

Here, e is the electron charge, m_e is mass of the electron, c is the speed of light, I is the mean ionization potential, velocity $\nu = \beta c$ of the particle, N and z are the number density and the atomic number of the material. Figure 6.2 shows the deduced mass to charge ratio versus the element charge for the incoming projectiles, shows a clear separation of different isotopes coming from the mixed beam.

6.1.3 Selection of incoming projectiles

In order to reconstruct the four-momentum of all outgoing particles after the target, the angle of the incoming beam after the collision with the target has to be measured. What is also important to know, is the position of the incoming ions on the target T_0 (x_0, y_0). This information will be used for the further analysis as a starting point for the trajectory reconstruction of the outgoing reaction products mainly protons.

Using a two-dimensional histogram a graphical cut on the particular incoming ions of interest, i.e. ^{32}Ar and ^{34}Ar , are applied and used for further analysis (see figure 6.2).

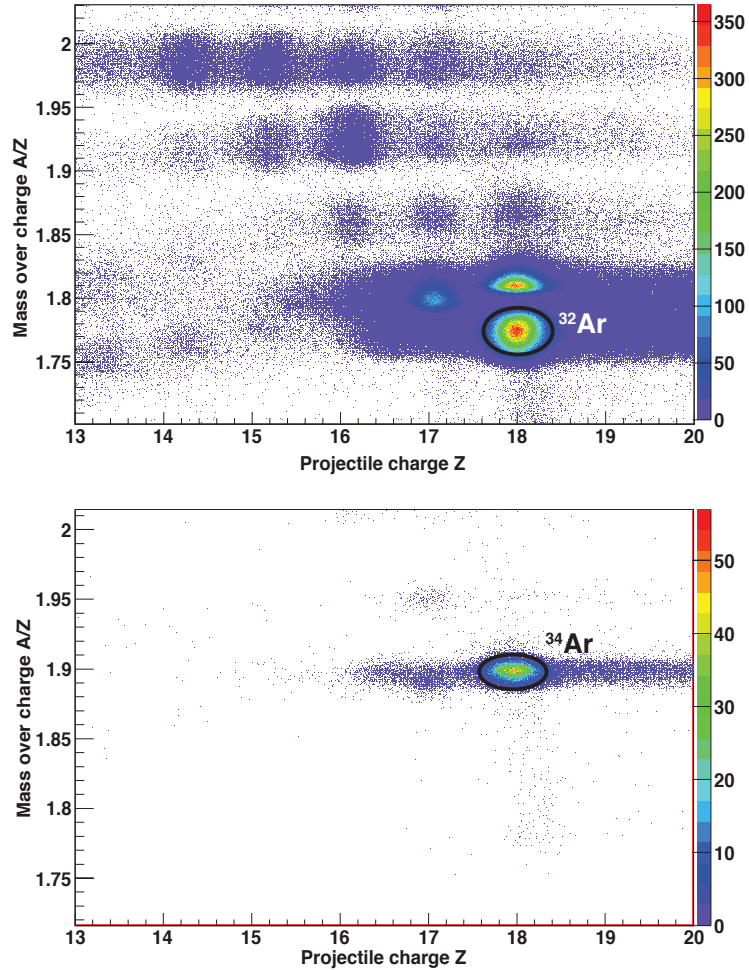


Figure 6.2: An example of a two-dimensional identification plot of mass to charge ratio versus Z of the incoming particles. The graphical cut to select ^{32}Ar and ^{34}Ar are shown.

The important parameters of ^{32}Ar and ^{34}Ar incoming beams are summarized in Table 6.1.

Table 6.1: Properties of the secondary beam. During the experiment there were set up different settings for ^{32}Ar and ^{34}Ar .

Ion	Energy AMeV	Energy (Cave C) AMeV	A/Z	$B\rho$ [Tm]	β_{in}	Δt_{S8-POS} [ns]
^{32}Ar	825	652.1	1.77	7.5936	0.8087	228
^{34}Ar	759.8	592.0	1.88	7.5911	0.7913	332

6.2 Outgoing Channels

When the incoming channels have been specified, the next step is to select the outgoing particle after the secondary reaction target placed inside the Crystal Ball. The reaction target is mounted on a movable wheel in order to be able to switch between different targets without interruptions of the vacuum. In the target many different reaction channels are open, leading to a various reaction products which must be detected and identified by looking at the trajectory, mass A , charge Z and the velocity of the reaction products, obtained from tracked data through the ALADIN magnet. In this experiment three different types of particles need to be identified and characterized: heavy ions, protons, and γ rays. The reconstruction of the trajectory of heavy ions and protons of the chosen reaction is performed simultaneously using Silicon strip detectors (SST) located directly after the reaction target and before the ALADIN magnet which leads to a separation of the heavy ions and protons inside the magnetic field of the magnetic spectrometer. In order to detect all reaction products which are deflected to different angles and to have an accurate tracking through the ALADIN magnet, the magnetic field has to be properly chosen. During the experiment the current was set to $I = 2475$ A which corresponds to a magnetic field of approximately 1.3 Tesla.

6.2.1 Fragment Detection

Before tracking particles through the field of the ALADIN magnet and looking to the masses of the outgoing ions, the proper cut on the outgoing channels has to be applied. In order to reconstruct the trajectory of the heavy fragments the tracking detectors GFI1, GFI2, SST1 and SST2 are used.

The SST detector

In order to distinguish between a proton and a heavy ion and to reconstruct the position of their interaction, the SST1 and SST2 detectors are used. Since the SSTs are the only detectors which detect both particle types it is important to investigate the difference between them. From the correlation between two energy-loss measurements, one at the beginning of the outgoing track (SST1/SST2) and one at the end (NTF) one can select the outgoing channels of interested such as reaction products with $Z - 2$ and even some events with $Z - 1$ (see figure 6.3) for reactions of the incoming $^{32,34}\text{Ar}$ projectiles. A 2D cut on the energy loss correlation plot for the outgoing heavy fragments allows to reduce the background and eliminate secondary reactions coming from different materials along the beam line after the target like detectors, vacuum windows, air etc. which can produce break-up reactions after the target.

From table 6.2 one can see how many particle survived during the experiment up to the end of the setup. From the proposal [28] it was expected to detect about 500 events in the region up to 10 MeV excitation energy of the measurement on Pb target with 40 ions/per second. This would be sufficient to reach the goal of the experiment. The detected amount of the reaction products in the performed experiment is statistically sufficient for a physics analysis.

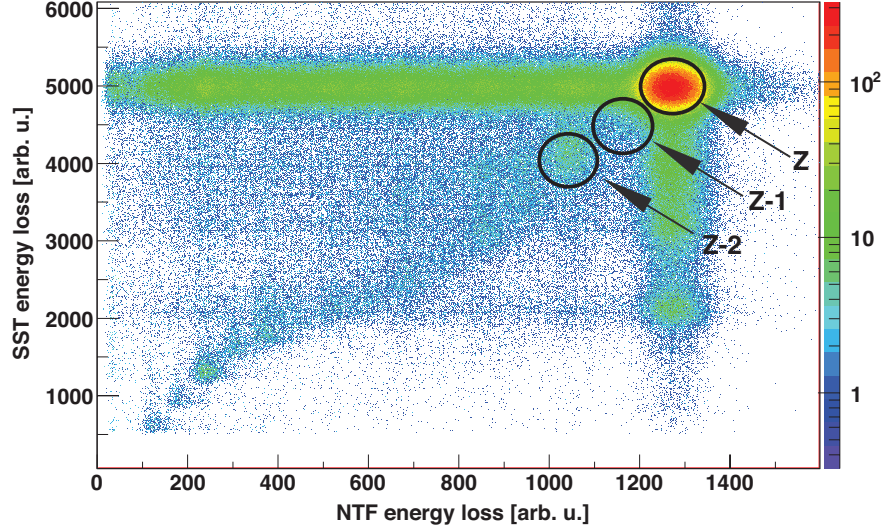


Figure 6.3: Example for incoming ^{32}Ar : Correlation of the energy loss between the Silicon Strip detector placed before the ALADIN magnet and NTF located behind the magnet. Looking to the left part of the NTF distribution one can see a long tail which comes from the secondary break-up reactions occurring between these two detectors. Such events occur with different charges in the NTF but one energy on the SST. Z corresponds to the primary ^{32}Ar beam, $Z - 1$ and $Z - 2$ are reaction products after photodissociation and emission of 1 and 2 protons, respectively. The energy loss information gives a possibility to make a clean cut on the outgoing channels.

Table 6.2: Estimation of good particles that survived up to the end of the setup for ^{32}Ar and ^{34}Ar beam.

Primary beam	Secondary beam	Energy [AMeV]	Target [mg/cm ²]	$B\rho$	Primary beam intensity	T_{pat}	Identified reaction products
^{36}Ar	^{32}Ar	825	Pb [515]	7.5936	1.25×10^{10}	NTF+GB	3180
^{36}Ar	^{34}Ar	759.8	Pb [515]	7.5911	2×10^9	NTF+GB	4320

6.2.2 Magnetic field

The tracking of particles through the ALADIN magnet requires knowledge of the magnetic field along the trajectory of the particles. All components of the magnetic field

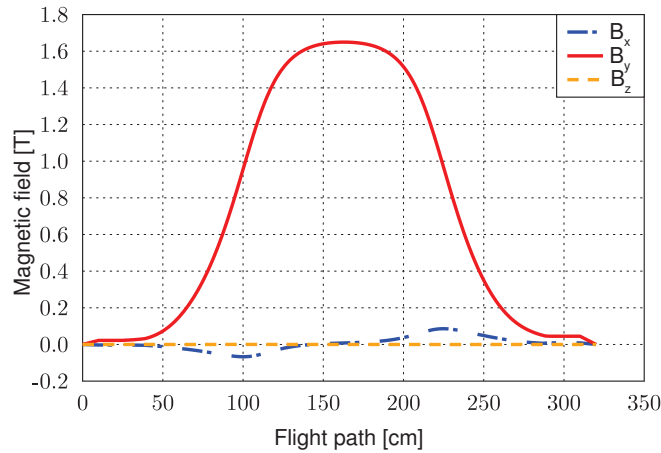


Figure 6.4: The magnetic field components of the ALADIN magnet are shown. The main y-direction of the field is clearly prominent if all particles pass the field in the x-z plane.

vector \vec{B} were measured by moving a hall sensor through the magnet. The magnetic field was set to the optimal value which allowed to deflect all particles into the respective downstream detectors. Figure 6.4 shows the three components (B_x , B_y , B_z) of the field. The ALADIN current used during the experiment, aside from the sweep and pixel runs, was $I = 2475$ A.

6.2.3 Tracking through ALADIN

Mass identification

After events from secondary reactions in materials after the target were removed from the data set, good events were tracked through the magnetic field of the ALADIN magnet in order to get a mass identification with sufficient mass resolution. For charged particles passing through a magnetic field, the magnetic rigidity $B\rho$ is related to the mass-to-charge ratio (A/Z) via the following equation:

$$B\rho \propto \frac{A}{Z}\beta\gamma. \quad (6.4)$$

β and γ are derived from time-of flight measurement. To obtain the mass A of the fragment, an additional condition that a proton triggered the TFW is applied, since otherwise everything is dominated by unreacted beam. Using the proton trigger helps to estimate the background coming from secondary break-up reactions and to exclude such events for the proper reconstruction of the four-momentum. Heavy fragments as well as protons from the decay of ^{32}Ar and ^{34}Ar are tracked through a dipole field. A particle tracking procedure through a dipole field was used, that has been developed by Ralf Plag for the R3B/LAND collaboration[51]. With this procedure the reconstruction of the trajectories of fragments and protons through the whole setup can be performed.

The fragments and the protons get separated by the ALADIN magnetic, and it is possible to track particles step-by-step and to determine the mass, the charge and momenta for 1p and 2p decays in the following approach:

1. Determination of x and y position and entrance angles of the particles before the ALADIN magnet using the SSTs.
2. Calculation of a trajectory depending on the measured β , an assumed mass (A) and the measured charge (Z) informations.
3. Tracking of the particles through the ALADIN step-by-step. This means that deflection of the particle was recalculated every millimeter. Thus, the step size is every 1 mm and the magnetic field was interpolated from the field maps, and the deflection according to this field was calculated and the particle was moved forward in the corresponding direction by 1 mm.
4. The calculated and measured positions on the detectors are compared. In case there is some difference, the mass is adjusted accordingly and the step 2 needs to be repeated in order to get the correct value.

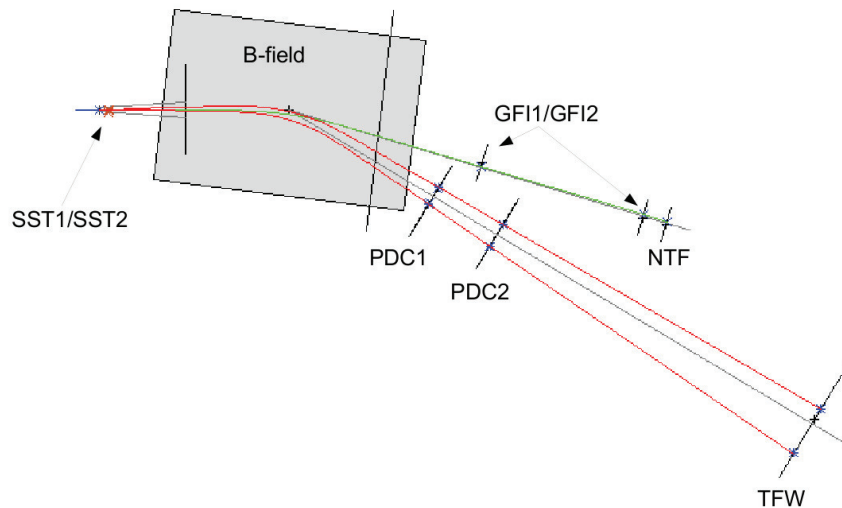


Figure 6.5: The plot shows an example of the reconstructed detectors hits of fragment and 2 protons by the tracker algorithm. The green lines represent the track of the heavy fragments while the red lines represent proton tracks. The blue crosses indicate the measured positions of the particles in the various detectors. Starting from the middle of the target, the SSTs detectors placed before the magnetic field, the GFIs and the NTF detectors used to track the heavy fragment are shown. The PDC drift chambers and the big ToF wall (TFW) are used to track protons.

Figure 6.5 shows the tracks of two protons together with the corresponding track of heavy fragment of the certain reaction. One can see how well tracks match to the real events for all used detectors.

Unreacted beam

The tracking algorithm is first used for tracking the unreacted beam, for which ample statistics is available. Fig. 6.6 shows the reconstructed fragment mass for ^{32}Ar (top) and ^{34}Ar (bottom), clearly demonstrating that the tracking algorithm used to reconstruct the masses is working well.

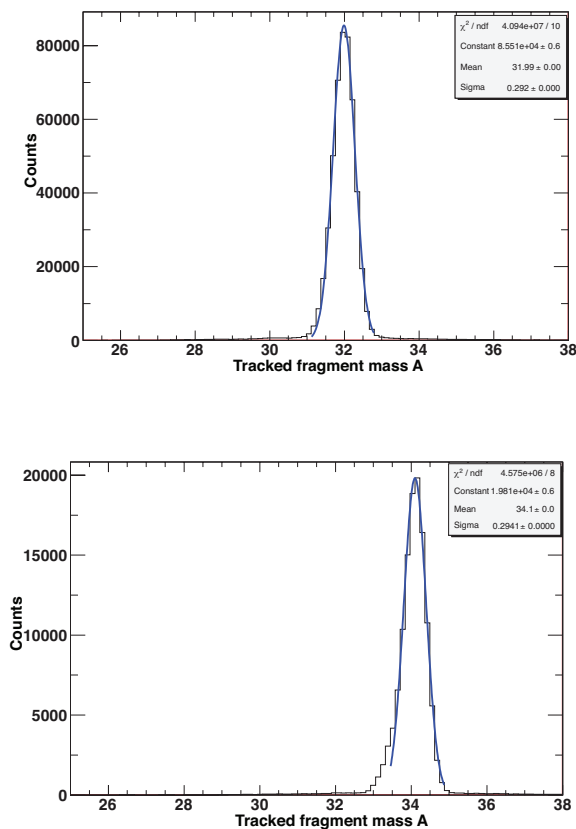


Figure 6.6: The plot shows an example of mass distribution for non-interacting ^{32}Ar (top) and ^{34}Ar (bottom) isotopes passing Pb target. Expected peak positions for non-reacted ^{32}Ar and ^{34}Ar to be at 32 and 34 respectively proves the proper working tracking algorithm. The mass resolution is around 0.8%.

Reaction products

After demonstrating that the tracking algorithm works properly, it can be used to derive the mass distribution of fragments and protons coming from a different reaction. Figure 6.7 shows the extracted mass distribution for the $^{32}\text{Ar}(\gamma, 2p)$ and $^{34}\text{Ar}(\gamma, 2p)$ reaction channels.

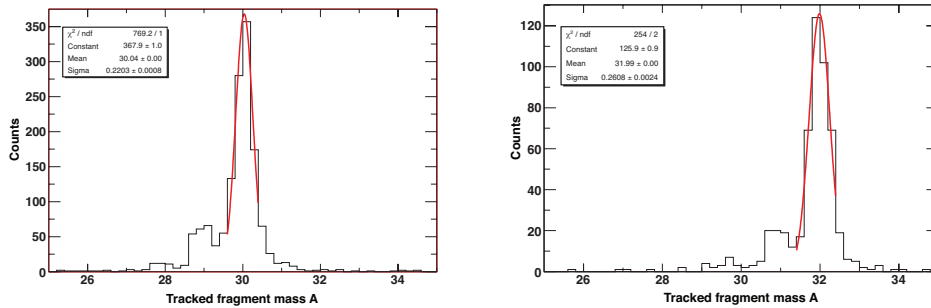


Figure 6.7: Fragment mass distributions for $^{32}\text{Ar}(\gamma, 2p)$ (left) and $^{34}\text{Ar}(\gamma, 2p)$ (right) reaction channels after the tracking through the ALADIN magnetic field.

Position resolutions of the fragment and protons are presented in figure 6.8 where the distribution for fragments is much narrower providing better resolution. Due to the limited opening angle in beam direction behind the target, an acceptance cut of the protons momentum distribution in y-direction is observed. From the correlation plot (Fig. 6.8, top right) one can observe the two wires which are missing in the first drift chamber (PDC1). Both of these effects can be corrected using the acceptance and efficiency corrections for the protons. The correction procedure will be described in the following section. The protons deflected to larger angles are stopped in the material of the beam line and absorbed there. They are not measured.

6.3 Acceptance corrections

To understand the response of all detectors, a simulation using the R3BROOT package has been carried out [52]. The simulation does not consider any detector specific effects. It contains information on the active areas of all detectors in the experimental setup and starts from the secondary production target placed in the centre of the Crystal Ball (see figure 6.9). The event generator in the simulation produces fragment and proton events with a certain momentum and they are propagated through the magnetic field to the drift chambers and TOF walls. For a certain momentum (for a certain excitation energy E_{exc}) the acceptance can be estimated as: $\text{acceptance} = N_{detected}/N_{started}$. Where $N_{detected}$ and $N_{started}$ are number of detected events and started within the simulation package. Figure 6.10 shows particle tracks through the magnetic field where some protons are stopped inside the ALADIN magnet in vertical direction. Protons with

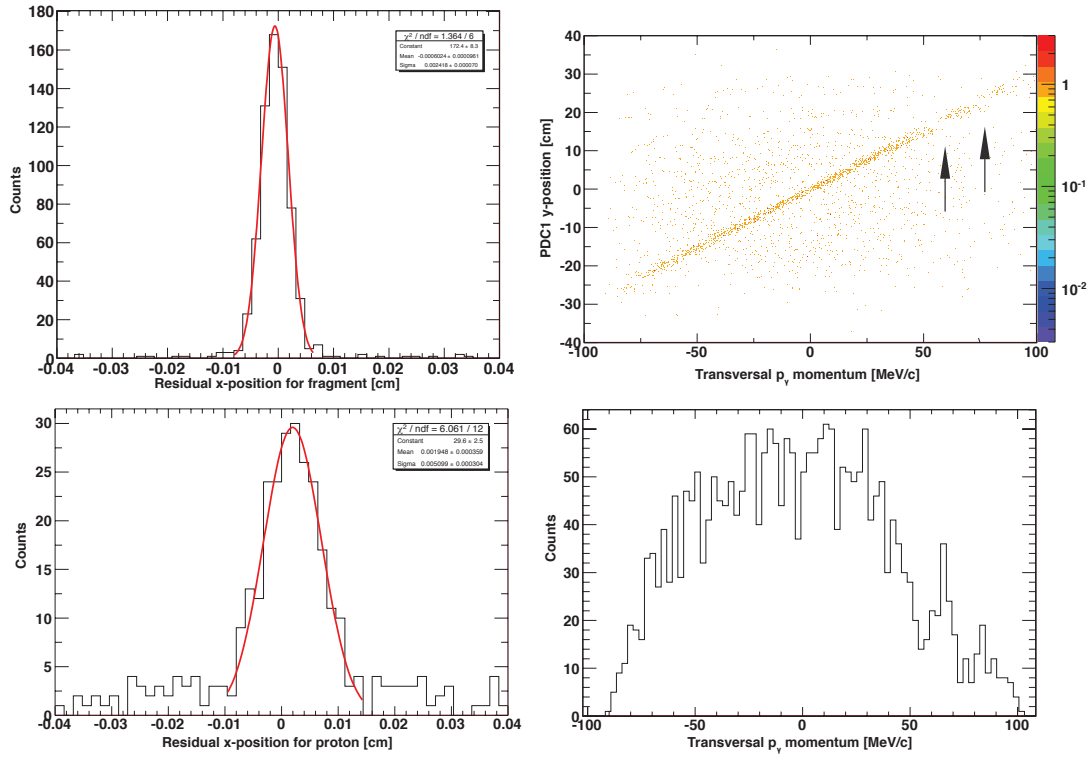


Figure 6.8: The x-residual position resolutions for the fragment (top left) and protons (bottom left) on the SST1 are shown. Due to the narrow position distribution for the fragment, the resolution as expected is much better ($\sigma = 0.02$ mm) compare with the protons. The projection on the x-axis (bottom right) shows a visible acceptance cut of the protons in y-direction due to the limited opening angle of the beam in y-direction behind the target. The correlation between the transversal p_y^\perp component and the y-position on the first drift chamber (top right) shows a place where two wires are missing.

higher excitation energies in the final nucleus are deflected to larger angles and simply absorbed by the ALADIN wall. The acceptance curves determined for the reactions $^{32}\text{Ar}(\gamma, p)$, $^{32}\text{Ar}(\gamma, 2p)$, $^{34}\text{Ar}(\gamma, p)$ and $^{34}\text{Ar}(\gamma, 2p)$ are presented in figure 6.11. One can see that the acceptance for high-momentum protons, which correspond to high excitation energies, is reduced due to the protons lost at the ALADIN window.

This effect has to be corrected for in the analysis by multiplying the excitation energy spectrum with a correction factor to yield an acceptance corrected excitation function.

6.4 Efficiency of the proton arm

The detection efficiency of each detector, depending on material, connected electronics, interaction mechanism and other properties, has to be considered for the analysis. In

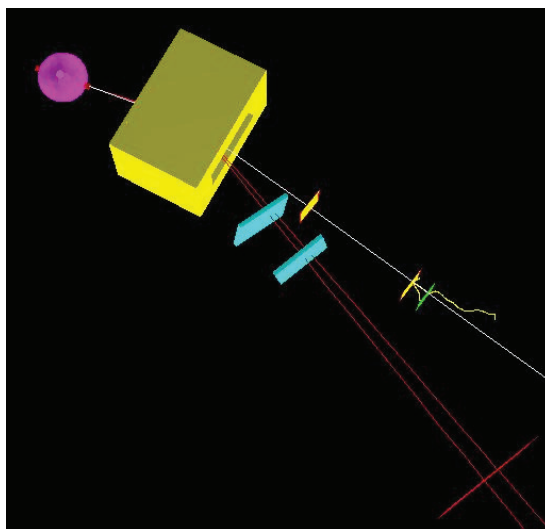


Figure 6.9: Experimental setup in the R3BROOT simulation package. Protons (red line) are tracked as well as fragments (white line) from different reactions.

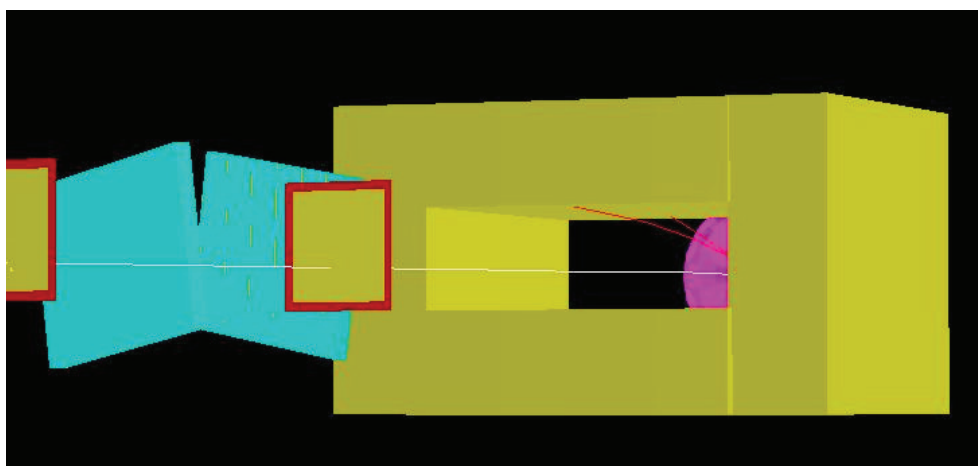


Figure 6.10: Protons with high excitation energies are deflected to larger angle and stopped in the ALADIN wall. It reduced the proton acceptance.

order to determine the efficiency of the proton arm, three individual detectors need to be considered: first drift chamber (PDC1), second drift chamber (PDC2) and big Time of Flight Wall (TFW). The schematic view of basic principle of the proton efficiency determination is shown in figure 6.12.

The one- and two-proton detection efficiencies of the drift chambers is determined using the data from the DHIT level of the *land02*. The detection of the protons is considered in all detector layers (PDC1-x, PDC1-y, PDC2-x, PDC2-y and TFW-x,

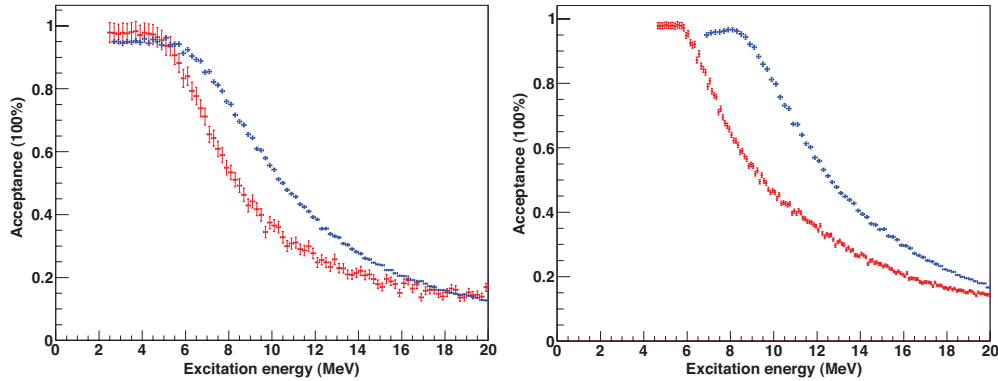


Figure 6.11: Acceptance curves for the one proton and two proton channels of incoming ^{32}Ar (left) and ^{34}Ar (right) respectively. Each curve starts from the certain specific energy separation threshold. The red curves describe one proton emitted in the reaction and the blue curves show the two proton cases.

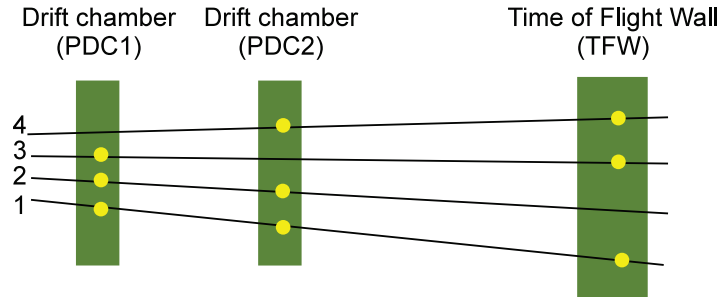


Figure 6.12: The combination of the proton efficiency detection. The total number (N_{total}) of events requires hits in all detectors (see case 1). Then the number of proton hits in each individual detector layers (unpacked in DHIT level) is counted by requiring that some events are missed in one plane of the detectors (see case 2, 3, 4).

TFW-y). The efficiency is obtained by counting for each detector the number of proton hits relative to the total number of crossing protons. In this algorithm, the TFW is not used for tracking, but only as a proton trigger. Since its triggering efficiency for one proton is more than 95% and even higher for the two protons, in the tracking procedure it is assumed to be 100% for each case.

In order to exclude random hits or wrong events and thus clean the data, a correlation between two layers of drift chambers PDC1 (x_1, y_1) and PDC2 (x_2, y_2) is required (see figure 6.13). This condition is applied to select events, which have correlation between the PDC1 and PDC2, e.g. if an event is detected on the right side of the PDC1 it has to also be detected at the right side of the PDC2, otherwise it is identified as noise and can't be tracked by the tracker because it will not be on a "straight" line (see figure 6.5). This procedure allows to avoid noise from particles coming from the

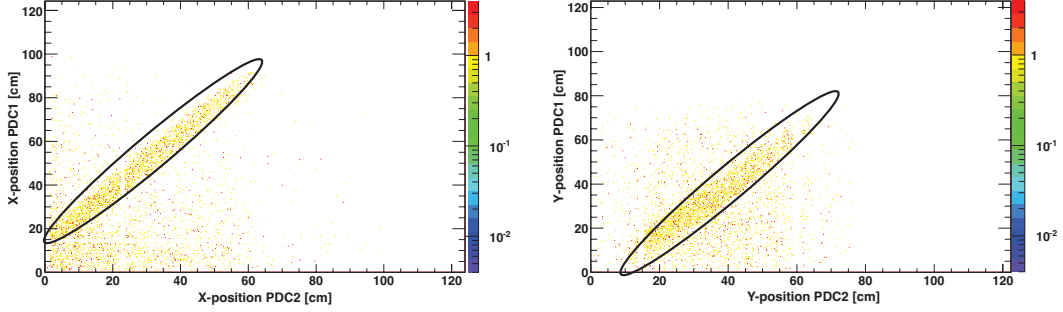


Figure 6.13: The correlation between two drift chambers PDC1 and PDC2 required to reduce the background.

neighboring detectors or from the single wires of the drift chambers.

There are several possible combinations of mixing entries and all those combinations of multiplicities of entries and layers need to be considered in order to calculate the efficiency. Let us look at the 1p case where all these combinations are considered in a following way:

N_{total} : $P_{dx1mul}=1, P_{dy1mul}=1, P_{dx2mul}=1, P_{dy2mul}=1, T_{fxmul}>0, T_{fy-}$
 $mul>0$

Correlation cut:

$(P_{dx1}, P_{dx2}), (P_{dy1}, P_{dy2})$

N_{PDCx1} : $P_{dx1mul}=0, P_{dy1mul}=1, P_{dx2mul}=1, P_{dy2mul}=1, T_{fxmul}>0, T_{fy-}$
 $mul>0$

Correlation cut:

(P_{dy1}, P_{dy2})

N_{PDCx2} : $P_{dx1mul}=1, P_{dy1mul}=1, P_{dx2mul}=0, P_{dy2mul}=1, T_{fxmul}>0, T_{fy-}$
 $mul>0$

Correlation cut :

(P_{dy1}, P_{dy2})

N_{PDCy1} : $P_{dx1mul}=1, P_{dy1mul}=0, P_{dx2mul}=1, P_{dy2mul}=1, T_{fxmul}>0, T_{fy-}$
 $mul>0$

Correlation cut:

(P_{dx1}, P_{dx2})

N_{PDCy2} : $P_{dx1mul}=1, P_{dy1mul}=1, P_{dx2mul}=1, P_{dy2mul}=0, T_{fxmul}>0, T_{fy-}$
 $mul>0$

Correlation cut:

(P_{dx1}, P_{dx2})

Identification of the detection efficiency for each layer is done by means of setting the multiplicity conditions for each layer (Pdx1mul, Pdy1mul, Pdx2mul, Pdy2mul, Tfxmul and Tfymul) and accepting only events which are in the correlation cuts (Pdx1, Pdx2) and (Pdy1, Pdy2) as shown in figure 6.13. The total number of events (N_{total}) detected by all detectors for one proton is determined using all combinations together (see case 1 in Fig. 6.12). The notations with signs "==" represent the multiplicity conditions to have 1 proton in the "x" or "y" - plane of PDC1/PDC2 detectors while "==0" defines the multiplicity "0" for the "x or y"- plane of the detectors, respectively. Tfxmul>0 and Tfymul>0 sets the multiplicity for the "x" and "y"-layer of TFW to be greater than "0". The correlation notation (Pdx1, Pdx2) or (Pdy1, Pdy2) requires protons to be in the correct place in the "x"-layer of the "PDC1/PDC2" or in the "y"-layer, correspondingly (see figure 6.13). Only "good" events, which are in the applied correlation cut, are used for the efficiency calculation.

Further on, e.g. for the one proton case, a multiplicity is set to 0 for the detector plane of interest and a number of detected events (N_{det}^{plane}) is determined, which allows to calculate the detection efficiency for the chosen plane (ϵ^{plane}) in the following way:

$$\epsilon^{plane} = 1 - \frac{N_{det}^{plane}}{N_{total}}, \quad (6.5)$$

where *plane* stands for the chosen detection plane (PDC1-X, PDC1-Y, PDC2-X, PDC2-Y).

For the two proton case the procedure is done in a similar manner, however the situation can be more tricky, because the two protons are indistinguishable. The algorithm is getting more complicated for two protons passing detector layers simultaneously which cannot be easily resolved in the first drift chamber. But since the second drift chamber is geometrically placed a few meters behind the first drift chamber, we assume that these protons can be resolved in the second drift chamber and this effect can, therefore, be corrected by the efficiency correction. All combinations for the two proton case are considered in a more complicated way:

N_{total}: Pdx1mul==2, Pdy1mul==2, Pdx2mul==2, Pdy2mul==2, Tfxmul>1, Tfymul>1

Correlation cut:

(Pdx1[0], Pdx2[0]), (Pdx1[1], Pdx2[1])

(Pdx1[0], Pdx2[1]), (Pdx1[1], Pdx2[0])

(Pdy1[0], Pdy2[0]), (Pdy1[1], Pdy2[1])

(Pdy1[0], Pdy2[1]), (Pdy1[1], Pdy2[0])

N_{PDCx1}: Pdx1mul <2, Pdy1mul==2, Pdx2mul==2, Pdy2mul==2, Tfxmul >1, Tfymul >1

Correlation cut:

(Pdy1[0], Pdy2[0]), (Pdy1[0], Pdy2[1])

(Pdy1[1], Pdy2[0]), (Pdy1[1], Pdy2[1])

$\mathbf{N}_{\text{PDCx2}}$: Pdx1mul==2, Pdy1mul==2, Pdx2mul<2, Pdy2mul==2, Tfxmul>1, Tfy-
mul>1

Correlation cut:

(Pdy1[0], Pdy2[0]), (Pdy1[0], Pdy2[1])
(Pdy1[1], Pdy2[0]), (Pdy1[1], Pdy2[1])

$\mathbf{N}_{\text{PDCy1}}$: Pdx1mul==2, Pdy1<2, Pdx2mul==2, Pdy2mul==2, Tfxmul>1, Tfy-
mul>1

Correlation cut:

(Pdx1[0], Pdx2[0]), (Pdx1[1], Pdx2[1])
(Pdx1[0], Pdx2[1]), (Pdx1[1], Pdx2[0])

$\mathbf{N}_{\text{PDCy2}}$: Pdx1mul==2, Pdy1mul==2, Pdx2mul==2, Pdy2mul<2, Tfxmul>1, Tfy-
mul>1

Correlation cut:

(Pdx1[0], Pdx2[0]), (Pdx1[1], Pdx2[1])
(Pdx1[0], Pdx2[1]), (Pdx1[1], Pdx2[0])

Here, the total number of events (N_{total}) detected by all detectors for two protons is determined using all combinations together (see case 1 in fig. 6.12). The notations with signs "==" represent the multiplicity conditions to have 2 protons in "x" or "y" - plane of PDC1/PDC2 detectors while "<2" defines the multiplicity less than 2 for the "x or y"- plane of the detectors, respectively. Tfxmul>1 and Tfy-
mul>1 sets the multiplicity for the "x" and "y"-layer of TFW to be greater than "1". In turn, in the correlation cut conditions the number in brackets "[]" stands for either the first [0] or the second [1] proton in "x" or "y" - layers of PDC1/PDC2. Considering that two protons are emitted simultaneously one needs to be careful since an entry 1 in the first PDC1-X layer does not necessarily corresponds to an entry 1 in the second PDC2-X layer and so on. And that is true for each event in the detectors. Using this method one by one each individual detector layer is considered. The correlation cuts are also applied in the two proton efficiency calibration (see figure 6.13). However, since two protons are involved, the correlation conditions have to include all possible combinations (Pdx1[0], Pdx2[0]), (Pdx1[1], Pdx2[1]) and (Pdx1[0], Pdx2[1]), (Pdx1[1], Pdx2[0]).

The resulting total efficiency of the proton arm for the drift chambers PDC1 and PDC2 and corresponding statistical errors are presented in table 6.3.

6.5 γ -ray contribution

The reconstruction of the invariant mass (formula 3.24) contains the energy E_γ carried by γ -rays. E_γ in the formula is the total energy of a cascade of a few gamma-rays emitted in the projectile's rest frame. It is detected using the sum over all individual

Reaction	Total efficiency \pm Error _{stat} [%]
$^{32}\text{Ar}(\gamma,1\text{p})$	63 ± 8
$^{32}\text{Ar}(\gamma,2\text{p})$	36 ± 5
$^{34}\text{Ar}(\gamma,1\text{p})$	66 ± 8
$^{34}\text{Ar}(\gamma,2\text{p})$	35 ± 4

Table 6.3: Total proton efficiencies obtained for a certain reaction channel for ^{32}Ar and ^{34}Ar beams.

crystals of the Crystal Ball above the common threshold value of 100 keV. This threshold allows to minimize the background without significantly reducing the number of real γ rays. However, the detected total γ -ray energy in each reaction event contains an admixture of real γ rays with an unknown contribution of the x-ray background. To understand the x-ray background produced in the target by atomic reactions a Monte-Carlo simulations has been performed. The x-ray event generator, using the simulated atomic interactions in the Pb target, has been inserted into R3B root which considers the full setup of the Crystal Ball [56]. Figure 6.14 shows that the experimental data

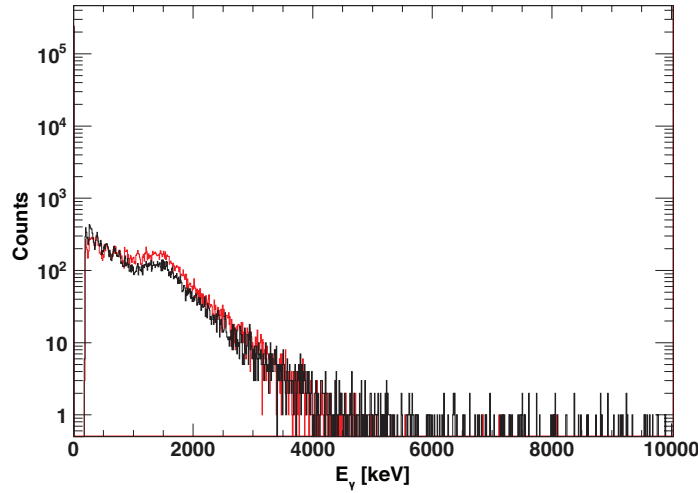


Figure 6.14: The simulation of the x-ray background have been performed and compared with the experimental data. The experimental (black line) and simulated (red line) x-ray background from the Crystal Ball are compared for the ^{32}Ar isotope.

is in reasonable agreement with the simulated data. The small difference can be a result of missing information in the simulation, such as absorption effects by the Silicon detectors and cables. Since the information of the experimental setup has not been fully implemented in the simulation, there is less absorption occurring in the simulation than in the real experiment. Nevertheless, the measured data is in reasonable agreement with the simulated data which demonstrates that the x-ray background is understood.

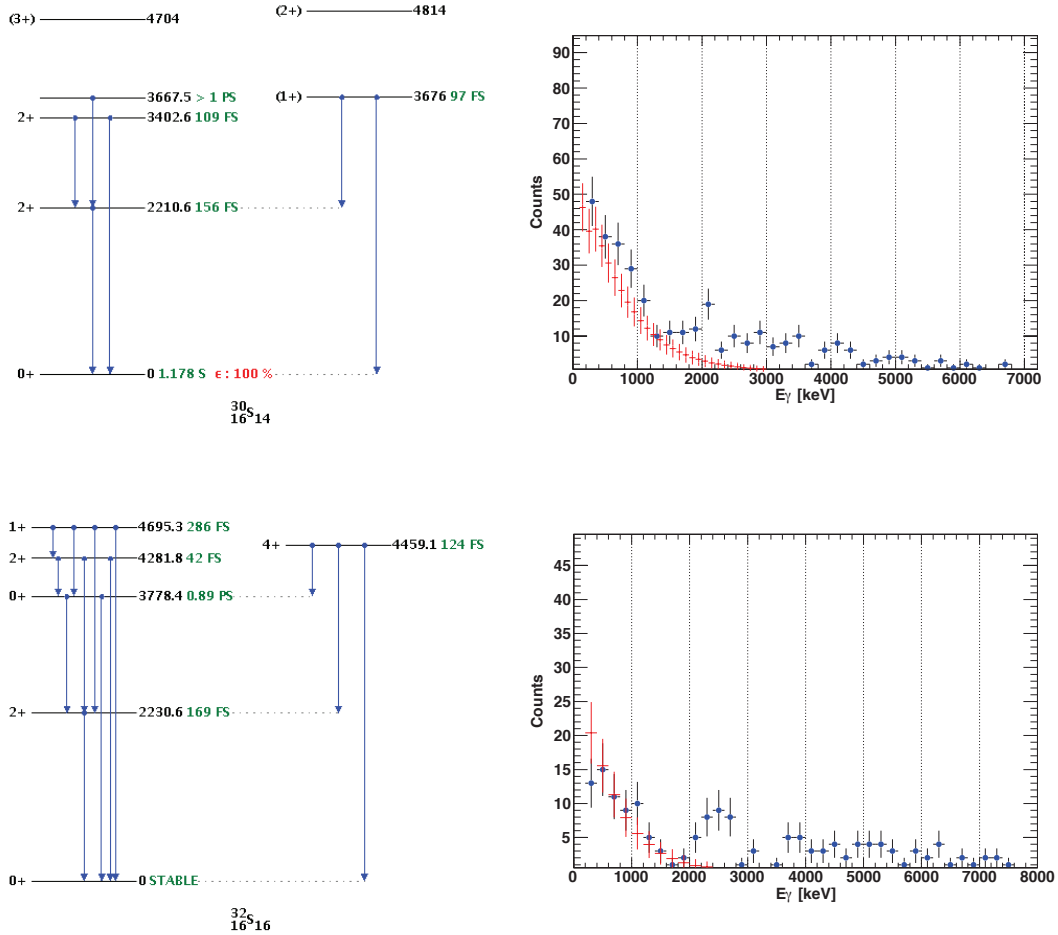


Figure 6.15: The γ -sum spectra represent $2^+ \rightarrow 0^+$ transitions in ^{30}S and ^{32}S ions. The background (red) is derived using the non-reacted beam and scaled to the number of incoming particles.

Figure 6.15 presents the measured γ -sum spectra for ^{30}S and ^{32}S isotopes. The x-ray background (red line) from the unreacted beam is scaled to the number of incoming events and compared with the real gamma-ray data. The transition from the 2^+ state to the 0^+ ground state in ^{30}S with an energy of 2.21 MeV and ^{32}S with an energy of 2.23 MeV are shown. In case of ^{30}S , the 2^+ transition to the ground state is not very strong, only about 0.5%, while for ^{32}S 13% of all gamma-decays proceed through the 2^+ to the ground state.

6.6 Background contamination

In this section the measures required to ensure that only the electromagnetic process induced by virtual photons at the target has contributed to the analyzed reaction channels are considered. The accompanying processes of two main types have to be taken into account: reactions with target nuclei due to nuclear interactions and reactions in the materials outside of the target. In order to properly subtract the background data with Carbon target and without target have been taken. Reactions outside the target are measured using runs where no target was implemented (so called "empty target"), while the nuclear contribution is estimated with the measurements on a carbon target. Since the atomic number of carbon is much lower ($Z=6$) than for lead ($Z=82$) and the flux of the virtual photons is proportional to Z^2 , it was chosen to investigate the nuclear contribution. The distribution measured with the carbon target can be considered to be pure nuclear cross section, since electromagnetic excitation obtained with carbon target is much smaller compared to the lead target. In order to have the same efficiencies for the three different measurements and to avoid additional corrections, the applied cuts and conditions must be the same as for the runs with target.

Since the nuclear interaction cross section depends on the radii of the interacting nuclei, the cross section measured on carbon target must be rescaled for comparison with the data from the lead target:

$$\sigma_{Pb}^{nucl} = \alpha_{Pb} \sigma_C, \quad (6.6)$$

where α_{Pb} is the nuclear scaling factor. There are several different approaches to define this scaling factor.

One of the ways to determine the α_{Pb} factor is based on the black-disk model [60] where the nuclear mass (A_{proj}) of the incoming $^{32,34}\text{Ar}$ projectile, lead and carbon nuclei are involved as:

$$\alpha_{Pb} = \frac{A_{proj}^{1/3} + A_{Pb}^{1/3}}{A_{proj}^{1/3} + A_C^{1/3}}. \quad (6.7)$$

This simple model leads to a scaling factor of $\alpha_{Pb} = 1.67$.

A more precise estimation of the scaling factor can be done using a semi-empirical model [61], where α_{Pb} is defined as following:

$$\alpha_{Pb} = \frac{1 + a \cdot A_{Pb}^{1/3}}{1 + a \cdot A_C^{1/3}}, \quad (6.8)$$

where a is a factor that accounts for the density distribution of the projectiles and targets used in the experiment. In the analysis of the present thesis the α_{Pb} -factor was determined (via a) using the experimental data itself in the following way.

In the mass distribution spectra of $^{32}\text{Ar}(\gamma, 2p)$ and $^{34}\text{Ar}(\gamma, 2p)$ reactions channels (see figure 6.16) one can see the contributions of ^{29}S and ^{31}S channels. The neutron separation threshold S_n for ^{32}Ar equals 21.5 MeV, which is above the adiabatic cutoff energy of the virtual photon spectra. Consequently, neutron removal contributions

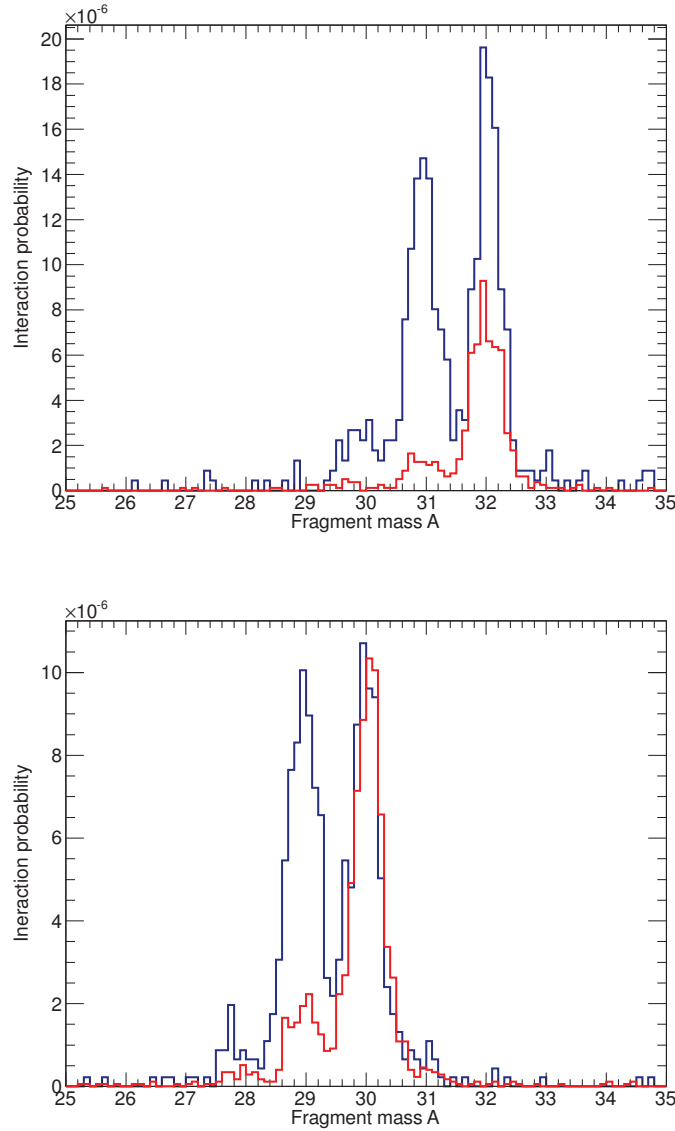


Figure 6.16: Mass distribution for $^{32}\text{Ar}(\gamma, 2p)$ (bottom) and $^{34}\text{Ar}(\gamma, 2p)$ (top) reactions channels in Pb (red line) and C (blue line) targets. The main peaks around the ^{30}S and ^{32}S are obtained using the cuts on outgoing fragment masses. The second peaks around the ^{29}S and ^{31}S coming from the nuclear reaction also contribute.

to the mass distribution can only be induced by the nuclear reactions. Assuming that those isotopes can be produced only in nuclear reactions one can check this supposition and derive α_{Pb} by using the runs with carbon target. Important is that the data for different targets (lead and carbon) are properly scaled to each other. Once the mass spectra are scaled and correctly subtracted one can derive the α -factor from the

experimental data using the method of selection, where the peak coming from the nuclear contribution vanishes meaning that the integrals of $^{29}\text{S}/^{31}\text{S}$ are equal to 0 (see figure 6.17). After using the derived a -factor in equation 6.8, the scaling factor was derived $\alpha_{Pb} = 1.45 \pm 0.3$. This experimentally derived value is in agreement with the

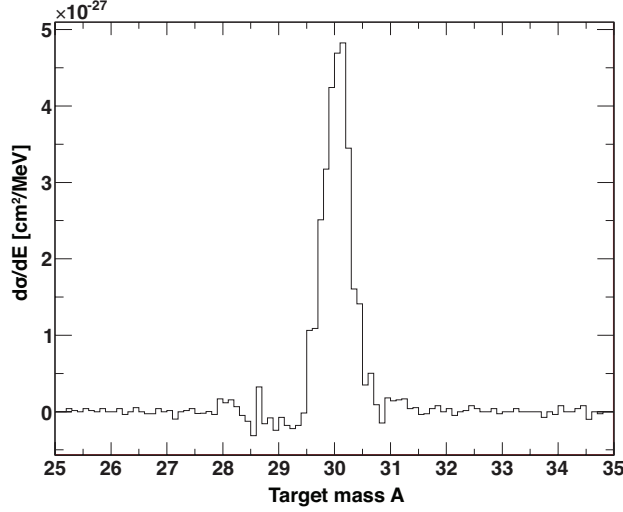


Figure 6.17: An example of the mass distribution for $^{32}\text{Ar}(\gamma, 2p)$ reactions channels after applying the experimentally derived α_{Pb} . The peak coming from the nuclear contribution vanishes meaning that the integrals of ^{29}S is equal to 0.

calculated one $\alpha_{Pb} = 1.67$ (by equation 6.7).

More sophisticated models can also be applied, giving different values for α_{Pb} factor. However, the total contribution of the nuclear background to the integrated Coulomb dissociation cross section is 15%. The variation of the α_{Pb} factor between different theoretical models is about 20%. Thus, the systematic uncertainty for the electromagnetic cross-section resulting from the variation of α_{Pb} is only 3% which is small compare to the statistical uncertainty of the measured cross-section and can therefore be neglected in the further discussion.

In order to calculate the Coulomb dissociation cross section the following equation is used:

$$\sigma_{C.D.} = p_{Pb} \left(\frac{M_m(Pb)}{d_{Pb} N_A} \right) - p_C \left(\alpha_{Pb} \frac{M_m(C)}{d_C N_A} \right) - p_{empty} \left(\frac{M_m(Pb)}{d_{Pb} N_A} - \alpha_{Pb} \frac{M_m(C)}{d_C N_A} \right) \quad (6.9)$$

where p is the interaction probability for a given target (Pb, C and empty), M_m is the molar mass of the target material [g/mol], d is the target thickness [g/cm²] and N_A is the Avogadro number [mol⁻¹]. Using this equation the cross section can be calculated for any target thickness (d) and nuclear interaction scaling (α_{Pb}).

Chapter 7

Results and Discussions

7.1 Excitation energy spectra

In order to conclusively prove existence or absence of low-lying dipole strength (pygmy resonance) in proton rich ^{32}Ar and ^{34}Ar nuclei, measurements of the excitation functions have to be performed. The excitation energy distributions for 1p- and 2p-channels are reconstructed from the measured fragment momenta and energies. Since ^{31}Cl has no bound excited state, the excited ^{32}Ar isotope decays mostly via two proton emission to ^{30}S (see figure 7.1). As one can see in fig. 6.3, applying the cut to select the data with only one tracked proton is complicated due to the low statistics. However, some events can still be identified as a 1p-reaction channel.

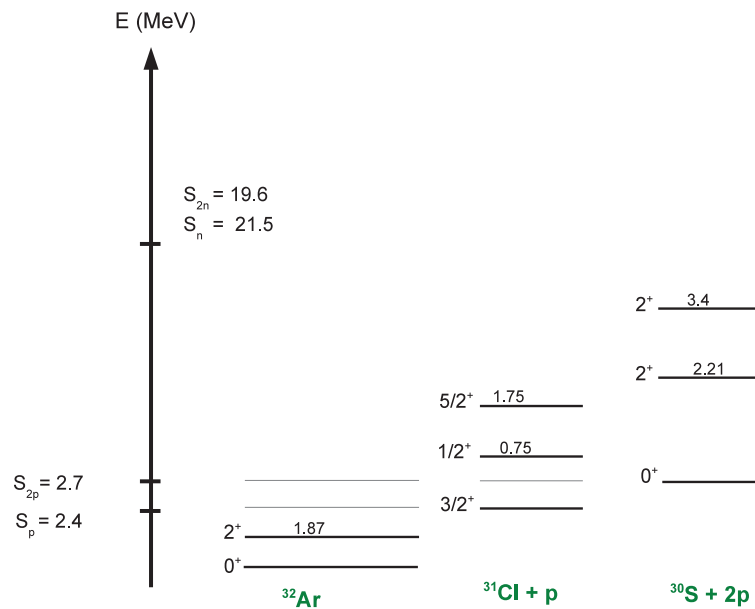


Figure 7.1: The energy of different isotopes for ^{32}Ar case. Due to the fact that ^{31}Cl has no bound excited state the excited ^{32}Ar isotope decays mostly via two (or more) proton emission.

For the proton branch the corresponding proton efficiency and acceptance correction must be applied (see sections 6.3 and 6.4). The energy reconstruction for the 2p-channel is more difficult than for the 1p-channel, because both protons must be identified and their trajectories have to be measured. The efficiency corrections must be applied due to different detection efficiencies for protons. In turn the proton acceptance correction is applied because of geometrical constrains of the setup which leads to the fact that the protons with high momenta may be cut (see chapter 6.3). Therefore, this correction is in particular crucial for a high excitation energy.

Figure 7.2 shows the resulting excitation energy distributions for the $^{32}\text{Ar}(\gamma, 2p)$ reaction, obtained by the reaction channel selection and reconstruction via the invariant mass approach (see equation 3.25). There are neither efficiency and acceptance corrections nor γ -ray contributions taken into account in the spectra. The excitation energy distributions were measured for both ^{32}Ar and ^{34}Ar isotopes with Pb, Carbon and empty targets. The excitation energies for the measurements with carbon target and without a target were reconstructed similarly as in the measurement with the lead target. However, γ -ray contributions measured by the Crystal Ball detector have to be treated differently for each target. That is because for the empty target case, the projectile reacts only with materials located outside the area around the Crystal Ball detector and therefore there is basically no γ -ray contribution in this measurement. Also there is little to no photon contribution in the measurement with the carbon target, because the γ -ray background originating from the target is very much suppressed due to a low atomic number of carbon. Nevertheless, it is necessary to measure the photon spectra with both (carbon and empty) targets in order to be able to subtract the photon background from the measurement with the lead target. In further analysis the γ -ray contribution, which amounted to more than 10% of the total counts was included in the excitation energy distribution for the reaction $^{32}\text{Ar}(\gamma, 2p)$. For the $^{32}\text{Ar}(\gamma, p)$ reaction, the γ -ray contribution is about 4%. However because of the low statistics in the $^{32}\text{Ar}(\gamma, p)$ case, inclusion of this contribution significantly reduces the excitation energy resolution (large uncertainties), therefore it is neglected in the excitation energy. In contrast, for the $^{34}\text{Ar}(\gamma, p)$ and $^{34}\text{Ar}(\gamma, 2p)$ reactions the statistics is substantially higher and the γ -ray contributions amounting 8% and 13%, respectively, do not lead to significant changes in the resolution as in the previous case. Therefore, both contributions are added to the final excitation energy. The corresponding spectra are shown in figure 7.3.

Figure 7.4 shows the excitation energy distributions of ^{32}Ar and ^{34}Ar isotopes derived from the 1p- and 2p-evaporation channels, where all corrections were applied and the γ -sum energy was added.

7.2 Coulomb excitation cross sections

In the carried out experiment the isotopes $^{30,32}\text{S}$ and $^{31,33}\text{Cl}$ were selected (by means of the previously discussed two-dimensional cuts), which are the decay products of $^{32,34}\text{Ar}$ undergoing a Coulomb excitation reaction on a lead target. In this work, there are two

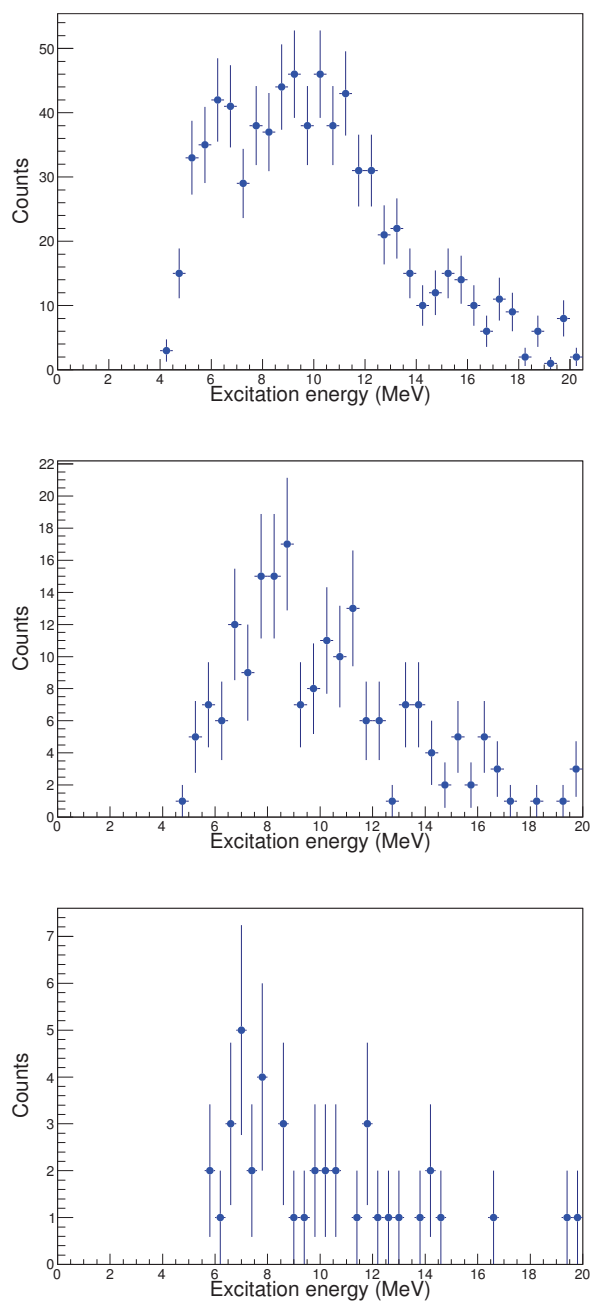


Figure 7.2: The histograms represent excitation energy distributions for ^{32}Ar isotope measured with lead (top), carbon (middle) and empty targets (bottom). Neither efficiency and acceptance corrections nor γ -ray contributions were applied to the spectra.

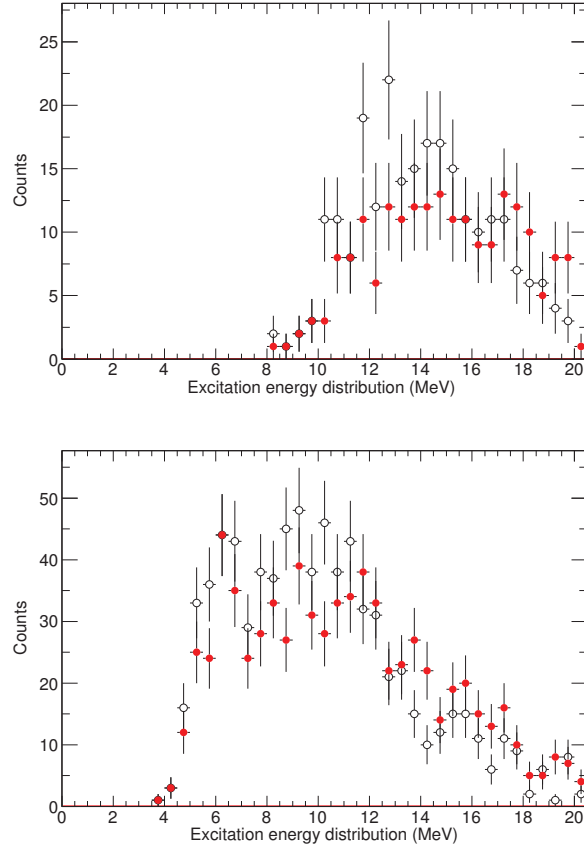


Figure 7.3: The excitation energy distributions for $^{32}\text{Ar}(\gamma, 2p)$ (bottom) and $^{34}\text{Ar}(\gamma, 2p)$ (top) isotopes measured with the lead target. The black dots represent the pure spectra and the red ones - the spectra with included γ -ray contribution. Neither acceptance nor efficiency correction were applied to the spectra.

complementary methods used to derive the Coulomb dissociation cross section.

In the first method, by means of a proper normalization and background subtraction, a spectrum of the measured excitation energy can be directly transformed into an energy differential electromagnetic excitation cross section

$$\sigma = \int \frac{d\sigma}{dE} dE. \quad (7.1)$$

As was already mentioned in section 6.6, the background events, resulting from the break-up occurring in different materials outside the target area, need to be taken into account. Therefore, a measurement without a target has been performed. The runs with the carbon target have been performed in order to exclude the nuclear contributions in the reactions on the lead target. The data for different targets have to be normalized first (see section 6.6). After normalization these contributions are sub-

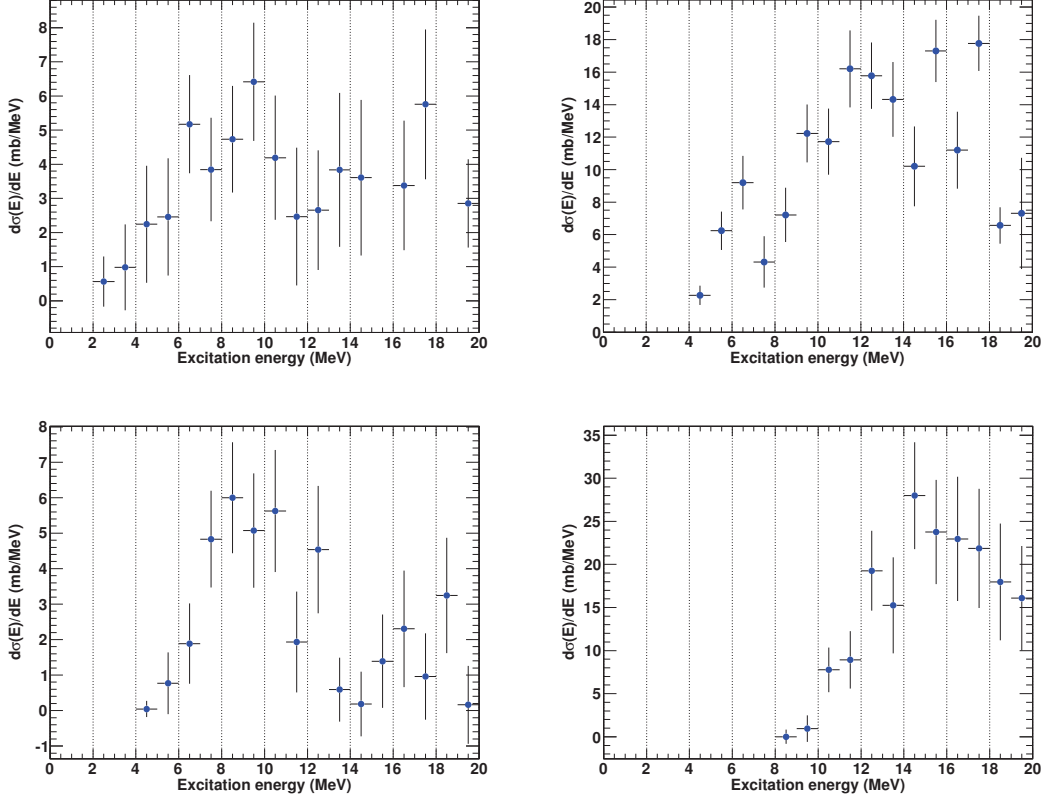


Figure 7.4: ^{32}Ar excitation energy distribution reconstructed from the data measured with lead target in one-proton (top left) and two-protons (top right) channels and as well as for ^{34}Ar in one-proton (bottom left) and two-protons (bottom right). Efficiency and acceptance corrections are applied. Since for $^{32}\text{Ar}(\gamma, p)$ reaction, the number of measured γ -rays is less than 4% of all data, they are not added. For $^{32}\text{Ar}(\gamma, 2p)$ reaction the γ -sum energy is added. Statistical errors are displayed.

tracted from the spectra measured with the lead target and the Coulomb dissociation cross section is derived using following equation:

$$\sigma_{C.D.} = p_{Pb} \left(\frac{M_m(Pb)}{d_{Pb} N_A} \right) - p_C \left(\alpha_{Pb} \frac{M_m(C)}{d_C N_A} \right) - p_{empty} \left(\frac{M_m(Pb)}{d_{Pb} N_A} - \alpha_{Pb} \frac{M_m(C)}{d_C N_A} \right) \quad (7.2)$$

where M_m is the molar mass of the target material [g/mol], d is the target thickness [g/cm²] and N_A is the Avogadro number [mol⁻¹]. p is the interaction probability for a given target (Pb, C and empty). If N_{proj} is the number of incident projectile and N_{react} is the number of events in a specific reaction channel, the interaction probability can be expressed as:

$$p = \frac{N_{react}}{N_{proj}}. \quad (7.3)$$

Due to limited efficiency and acceptance of the detectors, only a fraction of all particles

is registered. The efficiency correction factor ε (see section 6.4) and acceptance of the detectors (see section 6.3) have to be taken into account. If all the corrections are applied, the final formula for the cross section transforms into:

$$\sigma_{C.D} = \frac{\sigma_{C.D.} \cdot \varepsilon}{\text{acceptance}}. \quad (7.4)$$

In the second method, the cross sections are derived from the fragment mass distributions neglecting the proton branch measurements in order to avoid proton efficiency and acceptance corrections (see table 7.3). The number of incoming events and events in a specific reaction channels are determined using the same cut conditions and the same detectors. Only those events that have produced signals in all of the detectors are used for further analysis. Therefore, efficiencies of particular detectors do not play a role for the cross section derivation. Figure 7.6 shows the final mass distributions for the $^{32}\text{Ar}(\gamma, 2p)^{30}\text{S}$ and $^{34}\text{Ar}(\gamma, 2p)^{32}\text{S}$ reactions after subtraction of the scaled nuclear contribution and background (see equation 3.25). The blue line shows the Gaussian fit of the data points. The error bars represent the statistical errors of the measurements. The integrals of the spectra were taken in order to derive the Coulomb dissociation cross sections using formula 7.2 and these results are presented in table 7.4. In the mass distribution spectrum of $^{32}\text{Ar}(\gamma, 2p)$ reaction channel (see figure 7.5) one can see a contribution from ^{29}S occurring due to the neutron evaporation induced by nuclear reactions. The neutron separation threshold (S_n) for ^{32}Ar is 21.5 MeV, which is above the adiabatic cutoff energy of the virtual photon spectrum. Therefore, the mass distribution may contain contribution only from the neutron evaporation that is induced by the nuclear reactions and can be well handled (see section 6.6). The peak at a larger mass appears from a contamination of the cut and represents a wrongly tracked reaction channel that needs to be considered as systematical uncertainty in the analysis.

Consequently, there are several contributions that have to be taken into account as systematic uncertainties. As was just mentioned, one appears from differences in the applied incoming and outgoing two-dimensional cuts, where a small contamination from neighboring charges are affecting the results. In order to estimate the contribution from this variation, the overlap of gaussian distributions of the mass spectra with the wrongly (within 2σ) tracked isotopes is considered and the ratio gives an estimate of possible variation to be below 4%. The second contribution to the systematic error comes from differences in the two-dimensional cut sizes. In principle, the cross section has to be independent of the cut sizes, however this is not the case. When the size of the two-dimensional cut is too large, it can contain more events from other neighboring reaction channels as well as background events. However too small cut sizes result in larger statistical errors. In order to avoid the effect of the cut size and to reduce the systematic error, the two-dimensional cuts of the reacted and unreacted beam in the analysis have been set to have the same sizes. By varying the cut size, the systematic uncertainty in the integral cross section was estimated for each reaction and the results are summarized in table 7.1. The error in the areal densities of the carbon and lead targets results in another systematic uncertainty of about 2% that can be neglected.

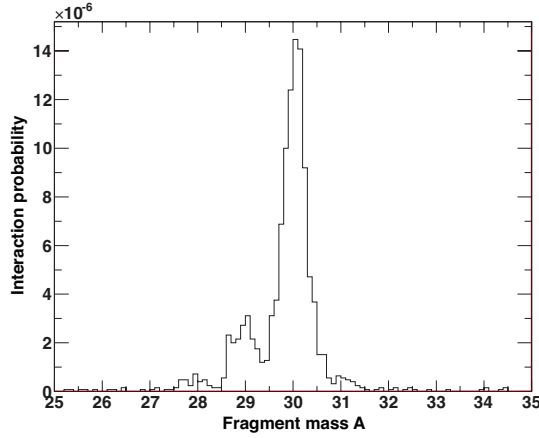


Figure 7.5: $^{32}\text{Ar}(\gamma, 2p)$ mass spectrum for the Pb target before the subtraction of background. The main peaks around ^{30}S is obtained using the cut on an outgoing fragment mass. The second peak around the ^{29}S is produced from the nuclear reactions. The tail of the peak at larger mass appears from contamination of the cut and presents a wrongly tracked neighboring reaction channel.

Table 7.1: Systematical errors due to cut variation for the Coulomb dissociation cross section measured without the proton branch.

Reaction	Cut variation error
$^{32}\text{Ar}(\gamma, p)^{31}\text{Cl}$	10%
$^{32}\text{Ar}(\gamma, 2p)^{30}\text{S}$	12%
$^{34}\text{Ar}(\gamma, p)^{33}\text{Cl}$	10%
$^{34}\text{Ar}(\gamma, 2p)^{32}\text{S}$	12%

From the data analysis implemented within the proton branch there are a few systematic uncertainties that have to be considered in the final results. The wrongly identified trajectory of all tracked protons (by the tracker) is estimated to be on the level of 1%, that can therefore be neglected. Another uncertainty comes from the errors of the proton efficiency estimation (see table 7.2).

Table 7.2: Systematical errors of the Coulomb dissociation cross section measurement derived from the excitation energy spectrum.

Reaction	Efficiency correction
$^{32}\text{Ar}(\gamma, p)^{31}\text{Cl}$	19%
$^{32}\text{Ar}(\gamma, 2p)^{30}\text{S}$	18%
$^{34}\text{Ar}(\gamma, p)^{33}\text{Cl}$	19%
$^{34}\text{Ar}(\gamma, 2p)^{32}\text{S}$	17%

From the presented data one can conclude that two different methods for determining the cross section are in a good agreement and can be used to calculate the cross

section for the other channels.

Table 7.3: Summary of the total Coulomb dissociation cross sections for specified channels on the lead target derived from the mass spectrum. The statistical and systematical uncertainties are shown for each cross section value.

Reaction	C.S. from mass spectrum (Err_{stat})(Err_{syst})
$^{32}\text{Ar}(\gamma, p)^{31}\text{Cl}$	58 (8)(6) mb
$^{32}\text{Ar}(\gamma, 2p)^{30}\text{S}$	236 (6)(31) mb
$^{34}\text{Ar}(\gamma, 1p)^{33}\text{Cl}$	34 (5)(4) mb
$^{34}\text{Ar}(\gamma, 2p)^{32}\text{S}$	176 (6)(23) mb

Table 7.4: Summary of the total Coulomb dissociation cross sections for specified channels on the lead target derived from integration of the Coulomb excitation spectrum. The statistical and systematical uncertainties are shown for each cross section value.

Reaction	C.S. from excitation energy distribution (Err_{stat})(Err_{syst})
$^{32}\text{Ar}(\gamma, p)^{31}\text{Cl}$	51 (6)(10) mb
$^{32}\text{Ar}(\gamma, 2p)^{30}\text{S}$	240 (12)(43) mb
$^{34}\text{Ar}(\gamma, 1p)^{33}\text{Cl}$	38 (7)(8) mb
$^{34}\text{Ar}(\gamma, 2p)^{32}\text{S}$	182 (9)(31) mb

7.3 Low-energy excitation

As one can see (Fig. 7.4), the excitation energy distribution of the 2p-channel is shifted towards higher energies. This channel does not open sharply at the two-proton separation energy of $S_{2p} = 2.7$ MeV (see table 7.5) but at around 4 MeV, and that can be explained by the presence of the Coulomb barrier. The strength is overlapping with the 1p-channel even if the excitation energy exceeds the 2p binding energy. The 3p channel in both isotopes is not considered in the present work. Because of the high background, stemming from the break up after the target, and a low three proton detection efficiency of the drift chambers (PDC1/PDC2), there is not enough statistics to extract a reasonable Coulomb excitation cross section.

Isotope	Proton separation threshold [MeV]		
	1p	2p	3p
^{32}Ar	2.4	2.7	7.1
^{34}Ar	4.7	6.9	15.7

Table 7.5: Proton separation energy thresholds for $^{32,34}\text{Ar}$.

In turn, the excitation energy distribution for the 1p channel does open at the separation threshold of $S_p = 2.4$ MeV (see Fig. 7.4). Since there is no competing decay present at the low energy, the protons can already be emitted at energies below the

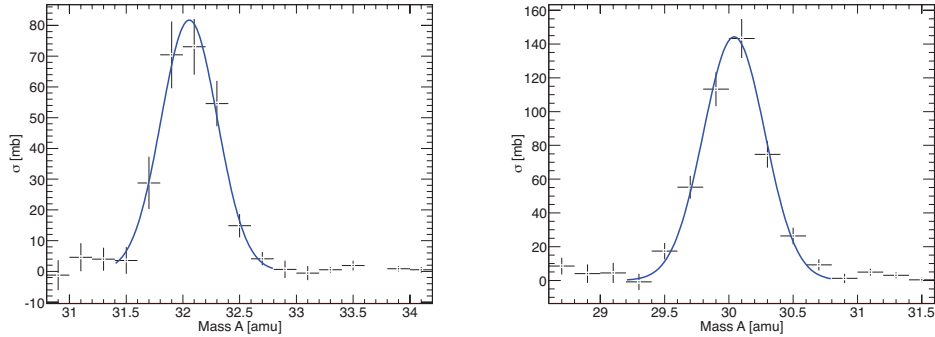


Figure 7.6: The mass distribution for the $^{32}\text{Ar}(\gamma, 2p)^{30}\text{S}$ (right) and $^{34}\text{Ar}(\gamma, 2p)^{32}\text{S}$ (left) reactions. The mass spectra are normalized to the numbers of incoming projectiles. After scaling and subtraction of nuclear contribution and background, the Coulomb cross sections spectra are obtained.

Coulomb energies. One has to mention, that since the γ -ray contribution for the 1p channel is less than 4%, it could be neglected in the final analysis. However, for all the other channels the photon contributions were significant and the corresponding γ -sum energies were included in the final analysis.

Furthermore, in order to compare the Coulomb excitation energy distributions between ^{32}Ar and ^{34}Ar , both reaction channels (1p and 2p) were added together for each isotope and the resulting spectra are shown in figure 7.7. There is a clear signature of a presence of the dipole excitations at low excitation energies in the case of ^{32}Ar . In contrast in the ^{34}Ar isotope case, this feature seems to be absent. These additional strengths in ^{32}Ar are observed in the area of 6 and 10 MeV excitation energy. An integration of the spectral regions below 10 MeV (the region where appearance of the resonances was predicted for ^{32}Ar) resulted in the cross sections of 71 *mb* and 17 *mb* for the ^{32}Ar and ^{34}Ar isotopes, respectively. One can conclude that there is a clear signature of a presence of additional excitations at low energies appearing in the ^{32}Ar isotope. Even though, the cause of this appearance of the low-lying strength still needs to be justified, however it strongly suggests for the first observation of a possible pygmy resonance in a neutron-deficient nucleus.

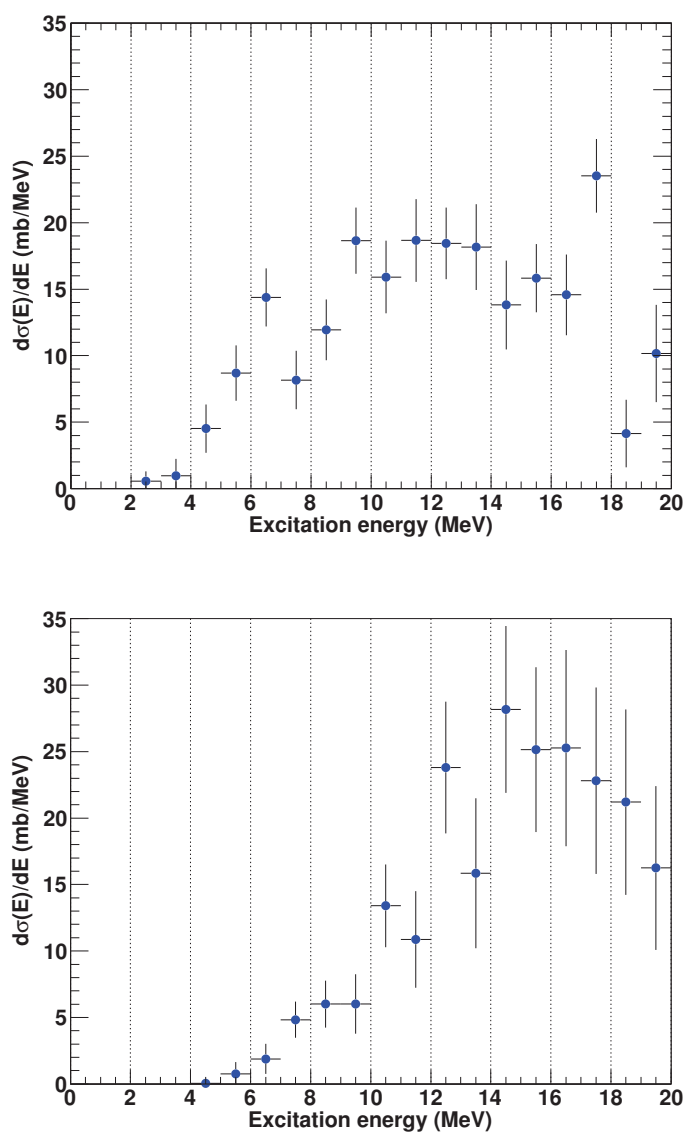


Figure 7.7: Excitation energy distributions for ^{32}Ar (top) and ^{34}Ar (bottom) isotopes, where both 1p- and 2p-reaction channels were summed up.

Chapter 8

Summary and outlook

The reactions $^{32}\text{Ar}(\gamma, p)$, $^{32}\text{Ar}(\gamma, 2p)$, $^{34}\text{Ar}(\gamma, p)$ and $^{34}\text{Ar}(\gamma, 2p)$ were studied using the Coulomb excitation method in inverse and complete kinematics at the LAND/R3B setup at GSI. The $^{32,34}\text{Ar}$ isotopes were obtained via fragmentation of a primary ^{36}Ar beam on a $6.347\text{g}/\text{cm}^2$ Be target located at the entrance of the FRS. The produced proton-rich projectiles with a similar mass-to-charge ratio were separated in flight from the primary beam and other reaction products and impinged on a $500\text{ mg}/\text{cm}^2$ Pb target with accompanied electromagnetic excitation and dissociation. One of the main goals of the experiment is to search for the proton dipole pygmy resonances in nuclei near to the proton drip line. The measurement was motivated by recent theoretical calculations by N. Paar *et al* [10]. The proton pygmy resonance was predicted to be a low energy excitation mode, lying below the giant resonance, which appears due to oscillations of proton skin against the isospin symmetric core. The theoretical calculations predicted appearance of the pygmy resonance in proton rich nuclei such as ^{32}Ar in the range between 8-10 MeV excitation energy. While for ^{34}Ar no substantial pygmy strength was predicted a strong low-lying mode was predicted for ^{32}Ar . Since the proton separation thresholds are much lower than the neutron separation thresholds in case of ^{32}Ar the pygmy resonance decays by proton emission. That is also true for the giant resonance centered at an excitation energy of 20 MeV.

In the experiment carried out in this work, the reconstruction of the excitation energy for one- and two-proton emission channels for ^{32}Ar and ^{34}Ar were derived from the particles momenta using the invariant mass method allowing for an investigation of dipole strength appearance. The Coulomb dissociation cross sections were extracted for the reaction channels of interest. The cross sections were derived by using two complementary methods which were found to be in a good agreement.

The first method was based on a measurement of the cross sections of $^{32,34}\text{Ar}(\gamma, p)$ and $^{32,34}\text{Ar}(\gamma, 2p)$ reactions and it was performed without the full proton branch of the experimental setup which simplified the data evaluation. Using a specialized tracking algorithm the mass spectra of the outgoing isotopes were extracted. After the proper normalization and subtraction of the background, the Coulomb dissociation cross sections were derived.

The second method included a full proton branch which allowed a reconstruction of the excitation energy of ^{32}Ar and ^{34}Ar from one- and two-proton channels. Integra-

tions of the energy differential spectra resulted in Coulomb dissociation cross sections. A very good agreement of these results with the ones derived in the first method has justified that all additional corrections applied in the second method were done properly. In further analysis, a signature of additional resonant strengths was observed in the low excitation energies (below 10 MeV) of ^{32}Ar , whereas in ^{34}Ar it did not seem to be the case. The observed low-lying strength could be attributed to the pygmy resonance, which would be the very first experimental confirmation of their existence in a neutron-deficient nucleus. However, in order to conclusively justify observation of the proton pygmy resonance further investigations are required, where the data has to be complemented with a reaction model along with the decay mechanism allowing for a complete interpretation of the 1p- and 2p-decay data. The analysis of the present experiment is in progress. At the future facility of antiproton and ion research (FAIR) the R3B experiment is designed to take advantage of a few orders of magnitude higher radioactive beam intensities using a much more sensitive detector setup. A high-resolution measurements of the energy-differential cross sections will be feasible for exotic nuclei, that so far were not accessible in any laboratory. This will open up new possibilities for fundamental nuclear physics as well as astrophysical studies providing a high-quality experimental data.

Bibliography

- [1] L. C. Biedenharn and P. J. Brussaard. Coulomb Excitation. Clarendon Press, Oxford (1965).
- [2] K. A. Ter-Martirosyan, J. Exptl. Theoret. Phys. (U.S.S.R.) 22, 284 (1952).
- [3] N. Ryezayeva et al., Phys. Rev. Lett. 89, 272502 (2002).
- [4] J. Enders et al., Nucl. Phys. A724, 243 (2003).
- [5] T. Hartmann et al., Phys. Rev. Lett. 93, 192501 (2004).
- [6] A. Leistenschneider et al., Phys. Rev. Lett. 86, 5442 (2001).
- [7] P. Adrich et al., Phys. Rev. Lett. 95, 132501 (2005).
- [8] P. Adrich: Observation of Pigmy and Giant Dipole Resonances in ^{132}Sn and neighboring mass isotopes. PhD thesis, Jagiellonian University, Kraków (2005).
- [9] Kurt Alder and Aage Winther. Coulomb Excitation. Academic Press, New York (1966).
- [10] N. Paar et al., Phys. Rev. Lett. 94, 182501 (2005).
- [11] Relativistic Beams of Exotic Nuclei - A Powerful Tool for Nuclear Structure Physics, GSI-Nachrichten 3 (1997).
- [12] G. C. Baldwin and G. S. Klaiber Phys. Rev. 71 (1947).
- [13] U. Garg: Nucl. Phys. A 649, 66c (1999).
- [14] W. Bothe and W. Gentner. Zeitschrift für Physik 71, 236248 (1937).
- [15] A. J. Migdal. Phys. (USSR) 8 (1944).
- [16] M. Goldhaber and E. Teller. Phys. Rev. 74, 1046 (1948).
- [17] M. N. Harakeh and A. van der Woude, Giant Resonances, Oxford Studies in Nuclear Physics, vol. 24, Oxford University Press (2001).
- [18] J. S. Levinger and H.A. Bethe, Phys. Rev. Lett. 42, 115 (1950).
- [19] D. Vretenar, N. Paar, P. Ring, and G.A. Lalazissis, Phys. Rev. C 63, 047301 (2001).

-
- [20] D. Vretenar, N. Paar, P. Ring, and G.A. Lalazissis, *Phys. Rev. A* 692, 496 (2001).
- [21] N. Paar, P. Ring, T. T. Nikšić, and D. Vretenar, *Phys. Rev. C* 67, 034312 (2003).
- [22] N. Paar, T. Nikšić, D. Vretenar, and P. Ring, *Phys. Lett. B* 606, 288 (2005).
- [23] N. M. Harakeh and A. van der Woude: *Giant Resonances: Fundamental High-Frequency Modes of Nuclear Excitation*. Oxford Univ. Press, 656 pages (2001).
- [24] J. Suhonen: *From Nucleons to Nucleus: Concepts of Microscopic Nuclear Theory*. Springer, 648 pages (2007).
- [25] N. Paar et al., *Phys. Rev. Letters* 94, 182501 (2005).
- [26] C. Barbieri et al., *Phys. Rev. C* 77, 024304 (2008).
- [27] N. Paar et al., *Phys. Rev. Letters* 94, 182501 (2005).
- [28] R³B Technical Proposal (2005).
- [29] M. Roeder et al., GSI Scientific Report (2011).
- [30] D. Kresan et al., GSI Scientific Report (2011).
- [31] C. Langer, PhD thesis, Univ. Frankfurt (2012).
- [32] C. Langer et al., GSI Scientific Report (2010).
- [33] *Passage of Particles Through Matter in Review of Particle Physics*, *Eur. Phys. Jour. C* (1998).
- [34] <http://www-linux.gsi.de/weick/mocadi>.
- [35] W. R. Leo, *Techniques for nuclear and particle physics experiments*, Springer-Verlag (1994).
- [36] D. Griffiths, *Introduction to elementary particles*. Wiley-VCH Verlag GmbH (2004).
- [37] <http://www-linux.gsi.de/rplag/land02/detectors/gfi>.
- [38] J. Cub, G. Stengel, A. Grünschlo, K. Boretzky, T. Aumann, W. Dostal, B. Eberlein, Th. W. Elze, H. Emling, G. Ickert, J. Holeczek, R. Holzmann, J. V. Kratz, R. Kulesa, Y. Leifels, H. Simon, H. Stelzer, J. Stroth, A. Surowiec and E. Wajda, *A large-area scintillating fibre detector for relativistic heavy ions*, *Nucl. Inst. Meth. A* 402, 67-74 (1998).
- [39] J. Cub et al., *Nucl. Instrum. Methods A* 402, 67 (1998).

- [40] V. Metag, R. D. Fischer, W. Kuhn, R. Mühlhans, R. Novotny, D. Habs, U. v. Helmolt, H. W. Heyng, R. Kroth, D. Pelte, D. Schwalm, W. Hennerici, H. J. Hennrich, G. Himmele, E. Jaeschke, R. Repnow, W. Wahl, E. Adelberger, A. Lazzarini, R. S. Simon, R. Albrecht and B. Kolb.
- [41] G. F. Knoll. Radiation Detection and Measurement. John Wiley and Sons, Inc., 3rd edition (2000).
- [42] V. Metag, D. Habs, K. Helmer, U. v. Helmolt, H. Heyng, B. Kolb, D. Pelte, D. Schwalm, W. Hennerici, H. Hennrich, G. Himmele, E. Jaeschke, R. Repnow, W. Wahl, R. Simon, and R. Albrecht, In Detectors in Heavy-Ion Reactions, volume 178 of Lecture Notes in Physics, 163178. Springer Berlin/Heidelberg (1983).
- [43] <http://www-inj.gsi.de>
- [44] H. Geissel, P. Armbruster, K. H. Behr, A. Brünle, K. Burkard, M. Chen, H. Folger, B. Franczak, H. Keller, O. Klepper, B. Langenbeck, F. Nickel, E. Pfeng, M. Pfützner, E. Roeckl, K. Rykaczewski, I. Schall, D. Schardt, C. Scheidenberger, K. H. Schmidt, A. Schröter, T. Schwab, K. Sümmerer, M. Weber, G. Müünzenberg, T. Brohm, H. G. Clerc, M. Fauerbach, J. J. Gaimard, A. Grewe, E. Hanelt, B. Knödler, M. Steiner, B. Voss, J. Weckenmann, C. Ziegler, A. Magel, H. Wollnik, J. P. Dufour, Y. Fujita, D. J. Vieira, and B. Sherrill. Nuclear Instruments and Methods in Physics Research Section B: Beam Interactions with Materials and Atoms 70 (1-4), 286–297 (1992).
- [45] H. Geissel, G. Müünzenberg, and K. Riisager. Annual Review of Nuclear and Particle Science 45(1), 163203 (1995).
- [46] G. Müünzenberg. Nuclear Instruments and Methods in Physics Research Section B: Beam Interactions with Materials and Atoms 70 (1-4), 265–275 (1992).
- [47] B. Alpat et al, Nucl. Instr. Meth. A 540, 121 (2005).
- [48] I. Mukha et al, Phys. Rev. Lett. 99, 182501 (2007).
- [49] J. Alcaraz et al., Nucl. Instr. Meth. A 593, 376 (2008).
- [50] P. Azzarello: Test And Production Of The AMS-02 Silicon Tracker Detectors. PhD thesis, Universite de Geneve (2004).
- [51] R. Plag: <http://www-linux.gsi.de/rplag/land02/>.
- [52] Justyna Marganec and Christoph Langer. Private communication.
- [53] H. T. Johansson. The DAQ always runs. Performing large scale nuclear physics experiments. Licentiate thesis, Chalmers University of Technology, Göteborg, Sweden (2006).

- [54] S. Paschalis. Relativistic One-Nucleon Removal Reactions. Ph.D. thesis, University of Liverpool, UK (2008).
- [55] K. Mahata, H. T. Johansson, S. Paschalis, H. Simon, T. Aumann. Position reconstruction in large-area scintillating fibre detectors. Nucl. Inst. Meth. A 608(2), 331 - 335 (2009).
- [56] Dominic Rossi and Christoph Langer. Private communication (2012).
- [57] T. Le Bleis. Experimental Study of Collective Electric Dipole Mode in Neutron-Rich Nickel Nuclei. Ph.D. thesis, University of Strasbourg, France (2010).
- [58] H. T. Johansson. The DAQ always runs. Performing large scale nuclear physics experiments. Licentiate thesis, Chalmers University of Technology, Göteborg, Sweden (2006).
- [59] H. T. Johansson. Hunting Tools Beyond the Drip-lines. Performing large-scale nuclear physics experiments. Ph.D. thesis, Chalmers University of Technology, Göteborg, Sweden (2010).
- [60] T. Aumann, J. V. Kratz, E. Stiel, K. Sümmerer, W. Brüche, M. Schädel, G. Wirth, M. Fauerbach, J. C. Hill. Inclusive measurements of electromagnetic dissociation of ^{197}Au targets. Phys. Rev. C 47(4), 17281737 (1993).
- [61] Boretzky, K. Systematische Untersuchungen zur Coulombanregung der Zwei-Phononen Dipolriesenresonanz in ^{208}Pb . PhD thesis, Universität Frankfurt am Main, Germany (1995).
- [62] C. J. Benesh, B. C. Cook and J. P. Vary, Single nucleon removal in relativistic nuclear collisions, Phys. Rev. C40, 1198-1206 (1989).
- [63] J. D. Jackson. Classical Electrodynamics. John Wiley & Sons Inc., New York (1999).
- [64] E. Fermi. On the theory of collisions between atoms and electrically charged particles. Nuovo Cimento 2, 143-158 (1925).
- [65] J. D. Jackson: Classical Electrodynamics. Wiley, third edition, 808 pages (1998).
- [66] C. A. Bertulani and V. Y. Ponomarev: Microscopic studies on two-photon giant resonance. Phys. Rep., Vol.321, pages 139-251 (1999).
- [67] C. A. Bertulani and G. Baur. Nuclear Physics A 458(4), 725 - 744 (1986).
- [68] C. A. Bertulani and V. Y. Ponomarev. Physics Reports 321(4-5), 139 - 251 (1999).
- [69] A. N. F. Aleixo and C. A. Bertulani. Nuclear Physics A 505(2), 448 - 470 (1989).
- [70] A. Winther and K. Alder. Nuclear Physics A 319(3), 518 - 532 (1979).

-
- [71] N. Paar, P. Ring, T. Nikšić and D. Vretenar. Quasiparticle random phase approximation based on the relativistic Hartree-Bogoliubov model, *Phys. Rev. C* **67**, 34312 (2003).
- [72] D. Vretenar, T. Nikšić, N. Paar and P. Ring. Relativistic QRPA description of low-lying dipole strength in neutron-rich nuclei, *Nucl. Phys. A* **731**, 281288 (2004).

Acknowledgment

First and foremost, I would like to thank my supervisor, Prof. Dr. Reiner Krücken, not only for providing me the unique opportunity to do the PhD work but also for his greatest contribution to this work and for the skillful guidance, continued encouragement and support during this project. A great thank you! I am very grateful to my tutor, Dr. Roman Gernhäuser, for his great contribution to my understanding of physics, electronics and experimental techniques. Special thanks to Prof. Dr. Walter Henning for his support and help with administrative procedures at Technische Universität München.

I would like to express my gratitude to Prof. Dr. Thomas Aumann and to Dr. Konstanze Boretzky for hospitality and very fruitful work together in the R3B-LAND group at GSI. Many thanks to Ralf Plag for his help during the whole time of my PhD work pretty much in all experiment related topics. In my work with the data analysis I would like in particular to thank Dr. Justyna Marganec, who is always glad to discuss and solve the data analysis issues. I am very grateful to my colleagues Dr. Dominic Rossi and Dr. Yuliya Aksyutina for consulting me on various specific questions and for the team work on the calibration procedures. For their great contribution in calibration of the Crystal Ball and the drift chambers I am very thankful to Dr. Olga Ershova and Christine Wimmer. Many thanks to Dr. Håkan Johansson for many useful discussions about the data acquisition system and technical aspects. Special thanks to Dr. Aleksandra Kelic-Heil and Dr. Sergey Litvinov for the beam and FRS physics discussions. For very useful discussions about the data interpretation and physics I am very grateful to Dr. Michael Heil. I would like to thank Christophe Langer for all the work we've done together. Many thanks to Ganna Rastrepina and all my friends for the support and creating a great and friendly atmosphere. Thanks to all members of the R3B-LAND group for your general assistance in performing the experiments and successful beam-time. I have learned a lot collaborating with you, many thanks for very useful discussions and your interest in my work.

I would like to acknowledge my colleagues at the Technische Universität München for always being friendly and helpful. In particular, I would like to thank Ludwig Maier, Michael Bendel and Tudi Le Bleis for their encouragement in various difficult questions and situations. I greatly appreciate Sonja Winkler, Sabine Schwertel and Michael Böhmer for all the time we spent together developing the diamond detectors. Thanks to Sigrid Weichs and Petra Zweckinger for always being helpful and friendly.

My very special hearty thanks to my beloved husband Sergiy and my sweet little daughter Alexandra for your support and inspiration.

I cannot fully express my gratitude to my parents for supporting me in everything, I dedicate this work to you.

I express my gratitude to all people I may have forgotten to mention here, many thanks to everyone who has helped me in carrying out this work.